

2017

# IR Laser-Induced Gene Expression for Tracking Development of Single Embryonic Neurons and Glia in *C. Elegans*

Anupriya Singhal

Follow this and additional works at: [http://digitalcommons.rockefeller.edu/student\\_theses\\_and\\_dissertations](http://digitalcommons.rockefeller.edu/student_theses_and_dissertations)



Part of the [Life Sciences Commons](#)

---

## Recommended Citation

Singhal, Anupriya, "IR Laser-Induced Gene Expression for Tracking Development of Single Embryonic Neurons and Glia in *C. Elegans*" (2017). *Student Theses and Dissertations*. 389.  
[http://digitalcommons.rockefeller.edu/student\\_theses\\_and\\_dissertations/389](http://digitalcommons.rockefeller.edu/student_theses_and_dissertations/389)

This Thesis is brought to you for free and open access by Digital Commons @ RU. It has been accepted for inclusion in Student Theses and Dissertations by an authorized administrator of Digital Commons @ RU. For more information, please contact [mcsweej@mail.rockefeller.edu](mailto:mcsweej@mail.rockefeller.edu).



IR LASER-INDUCED GENE EXPRESSION FOR TRACKING DEVELOPMENT  
OF SINGLE EMBRYONIC NEURONS AND GLIA IN *C. ELEGANS*

A Thesis Presented to the Faculty of  
The Rockefeller University  
in Partial Fulfillment of the Requirements for  
the degree of Doctor of Philosophy

by

Anupriya Singhal

June 2017





IR LASER-INDUCED GENE EXPRESSION FOR TRACKING DEVELOPMENT  
OF SINGLE EMBRYONIC NEURONS IN *C. ELEGANS*

Anupriya Singhal, Ph.D.

The Rockefeller University 2017

The assembly of neural circuits requires a complex choreography of developmental events: neurons must be generated, extend neurites at the correct time and location, and then integrate extracellular information, like long-range guidance cues or cellular contacts, with an internal developmental program to make correct wiring decisions. Visualizing neural-circuit assembly *in vivo* can provide insight into how these events are coordinated. The *C. elegans* embryo, which contains only 222 neurons and 56 glia, is an attractive setting to study nervous system development comprehensively in an intact, living organism. However, methods to label and track optically-resolvable neurites or manipulate single neurons through gene expression do not exist, as most embryonic reporters are broadly expressed.

Here, I present a method for expressing fluorescent reporters or any gene of interest in specific *C. elegans* embryonic neurons, glia, or other cell types, without cell-specific drivers. Our method is based on a previous setup (Kamei et al., 2009), and uses an infrared (IR) laser to localize heat to the volume of a single precursor cell in the embryo. This induces gene expression in the progeny of that cell (1-4 cells/embryo) through heat-shock-response regulatory elements. I perform significant optimizations to adapt this strategy to cells in the *C. elegans* embryo, which are highly sensitive to heat toxicity. Direct temperature measurements of IR heating in the embryo reveal that cells

are heated to physiological temperatures (32°C) for 5 minute durations using our modified irradiation protocol. These conditions lead to high rates of gene induction (>60%) with no signs of damage.

First, I use our system to label and track single neurons during early nervous-system assembly. These studies reveal a retrograde extension mechanism for axon growth in specific interneurons. I also study the etiology of axon-guidance defects in *sax-3/Robo* and *vab-1/EphR* mutants; these studies suggest that a timing/competence mechanism controls axon-outgrowth dynamics in the nerve ring. Next, I demonstrate the versatility of IR irradiation by performing cell-specific rescues, determining DAF-6/Patched-related site of action during sensory-organ development. Finally, I demonstrate that IR cell irradiation can be used to perform simultaneous ablation and labeling of cells in the same embryo. I use this system to uncover a role for the amphid sheath glia in dendrite extension. As IR induction can be used for targeted labeling, gene expression, and ablation without the need for cell-specific drivers, this tool opens the door to high-resolution systematic analyses of *C. elegans* morphogenesis.

## Acknowledgments

First, I thank Shai Shaham, my thesis advisor. I have spent the last years in awe of Shai's ability to move between the worlds of biology, math, and optics with ease, and his deep and yet broad knowledge of science has been a constant source of inspiration for me. I thank Shai for his thoughtful suggestions and guidance, which kept me focused throughout this work. I especially want to thank him for suggesting that I implement the IR microscope - it was a real challenge, and one that I can feel proud to be on the other side of.

I want to thank the members of my committee, Gaby Maimon, Cori Bargmann, and Zhirong Bao for their scientific input. My rotation experiences in Zhirong and Cori's labs began my foray into worm biology, and I thank them for making the field so exciting to me when I started. I especially thank Zhirong and the members of his lab, in particular Anthony Santella and Pavak Shah, for being so generous with their time and ideas, and with reagents and other tools. I always looked forward to the Bao lab meetings, and I feel very fortunate to have had access to their expertise throughout this project. I also thank Alex Katsov from the Bargmann lab for giving me ideas on measuring temperature gradients and for being generous with equipment.

I want to thank all the members of the Shaham lab past and present who have created such a collegial, enriching work environment. I especially thank my benchmate for many years, Lena, whose optimism and energy are infectious; Wendy, for her deep kindness and vast cultural knowledge which kept me entertained during our many late nights in lab together; Sean, whose dry sense of humor was an antidote to all my failed experiments; and Menachem, for providing a kind but critical scientific eye and his

willingness to always lend a hand. I also thank Peter Insley for advice and for the many hours of fun working together to combine our microscopes; and Wolfgang Keil for many helpful scientific conversations. I also thank our lab manager Maya, who was always unfazed by my many tricky orders and kept the lab running smoothly.

I thank the Bio-Imaging Resource Center, especially Alison North, for being so accommodating to the imaging needs of this project and for allowing me to try out so many systems in the center. The quality of images in this work are a result of her persistence.

I thank the MD-PhD program for bringing me here, and Olaf, for his leadership and for the care he devotes to all of his students.

I want to thank my mother and father for their endless love and encouragement, and for being an unwavering source of happiness in my life. To my brother, Ashu, thanks for always being just one phone call away. I also thank my “new” parents for supporting me over these last few years.

Most of all, I thank my husband Varun, who is effortlessly kind, intelligent, and humble, and inspires me to try to do better every day. Thank you for always being by my side.

## Table of Contents

Chapter 1: Introduction .....	1
1.1 Live Imaging of Neuronal Development.....	2
1.2 <i>C. elegans</i> as a Model for Studying Neurodevelopment <i>in vivo</i> .....	5
1.3 Technical Challenges with Studying <i>C. elegans</i> Embryonic Nerve Ring Assembly.....	9
1.4 Automation of Lineaging in <i>C. elegans</i> .....	11
1.5 Imaging Techniques for Studying <i>in vivo</i> Development .....	13
1.6 Sparse Labeling Strategies Across Model Organisms .....	15
1.6.1 Genetic Strategies for Sparse Labeling .....	17
1.6.2 Optical Tools for Directed Cell Labeling .....	26
1.6.2.1 Photoconvertible Fluorescent Proteins .....	28
1.6.2.2 Optical Control of Visible Light-Sensitive Effector Proteins .....	29
1.6.2.3 Laser-Mediated Gene Induction via the Heat Shock Response .....	31
Chapter 2: Design and Calibration of Infrared Laser Optical Setup for Single-Cell Heating.....	40
2.1 Characterization of the Heat Shock Response in Embryos .....	40
2.2 Theoretical Simulations of Laser Heating .....	43
2.3 Design and Construction of IR Laser Microscope Setup .....	52
2.4 Direct Temperature Measurements of IR Laser-Induced Heating .....	59
Chapter 3: Optimization Single-Cell Heat Shock Induction using an IR Laser .....	71
3.1 Cell Identification with Sparse Lineage-Specific Markers .....	71
3.2 Overview of Induction Protocol .....	74
3.3 Failure to Optimize Pulsed Induction Parameters .....	74
3.4 Optimization of Long Duration, Continuous-Wave Heating .....	79
3.5 IR-Labeled Cells Develop Normally After Irradiation .....	80
Chapter 4: Labeling and Tracking Growth of Diverse Cell Types .....	87
4.1 Testing Irradiation Conditions in Different Sublineages .....	87
4.2 Retrograde Axon Extension in the AVB and RIV Neurons .....	94
4.3 The Order of Axon Entry into the Nerve Ring .....	95
4.4 Sensory Organ Formation .....	97
4.5 Other Cell Types .....	98

Chapter 5: Amphid Neuron Growth Dynamics in Wildtype and Guidance Mutants .....	100
5.1 Wildtype Amphid Axon Growth Dynamics .....	101
5.2 <i>sax-3</i> /Robo Mutant Growth Dynamics .....	104
5.3 <i>vab-1</i> /Eph Mutant Growth Dynamics .....	108
5.4 Order of Development in the Amphid Commissure .....	110
Chapter 6: Applications of IR Laser-Mediated Gene Induction and Cell Ablation .....	114
6.1 Embryonic Rescue of the Amphid Channel in <i>daf-6</i> /Patched-Related Mutants ....	114
6.2 Cell Ablation and Labeling Reveals a Role for Glia in Dendrite Extension .....	117
Chapter 7: Discussion .....	123
Chapter 8: Materials and Methods .....	133
Appendix A: A Stochastic, Genetic Method for Sparse Labeling .....	146
Appendix B: An Automated Method for Cell Identification without Lineage Tracing ..	150
Appendix C: Integration of IR Laser Induction with a SPIM Microscope .....	157
Appendix D: Characterization of Regulators of Glial Specification in <i>C. elegans</i> .....	163
Bibliography .....	184

## List of Figures

Figure 1.1 The <i>C. elegans</i> Nerve Ring .....	6
Figure 1.2 Timeline of <i>C. elegans</i> Embryogenesis .....	8
Figure 1.3 Genetic Strategies for Sparse Labeling .....	18
Figure 1.4 Optical Strategies for Sparse Labeling .....	27
Figure 1.5 IR-Laser Gene Induction .....	35
Figure 2.1 Characterizing the Heat Shock Response in Embryos .....	42
Figure 2.2 Simulations of Laser Heating .....	45
Figure 2.3 Evolution of Heating with Pulsing .....	46
Figure 2.4 Schematic of Optical Setup. ....	53
Figure 2.5 Optical Design and Construction.....	54
Figure 2.6 <i>in vitro</i> Temperature Calibration and Results. ....	63
Figure 2.7 <i>in vivo</i> Temperature Calibration .....	64
Figure 2.8 <i>in vivo</i> Temperature Measurements.....	67
Figure 3.1 Expression Pattern of <i>unc-130</i> Translational GFP reporter .....	73
Figure 3.2 Timeline of the IR Induction Protocol .....	76
Figure 3.3 Pulsed Parameters Lead to Cell Damage .....	77
Figure 3.4 Continuous Wave Heating Induces Cells Specifically and Without Damage .	81
Figure 3.5 Development of Heat-Shock-Labeled Cells Proceeds Normally .....	84
Figure 3.6 Natural Variation in Birth Time vs. Timing of Axon Outgrowth .....	85
Figure 4.1 Cell Lineages in which Induction was Performed .....	89
Figure 4.2 IR Labeling in Diverse Cell Types.....	90-91
Figure 4.3 Development of AVB, RIV, AMso, CEM cells.....	92
Figure 4.4 Development of AWC, SAAV, excretory duct, and DB cells. ....	93
Figure 4.5 Death and Process Clearance of the CEM Neuron.....	97
Figure 5.1 Trajectory of the Amphid Neurons.....	101
Figure 5.2: Wildtype Imaging of AWA, ASG, ASI, AIB neurons .....	103
Figure 5.3. Characterization of Embryonic Guidance Defects in <i>sax-3</i> Mutants .....	105
Figure 5.4: Defects in Dendrite Placement in <i>sax-3(ky123)</i> .....	107



Figure 5.5 Characterization of Embryonic Guidance Defects in <i>vab-1</i> Mutants .....	109
Figure 5.6 Characterization of Growth into the Amphid Commissure .....	111
Figure 6.1: IR-Induction of <i>daf-6</i> in Amphid Sheath rescues Defects in the Amphid Channel .....	116
Figure 6.2: Ablation and Labeling With IR Laser Reveals Glial Role in Dendrite Extension.....	119
Figure 8.1. Tail-to-Head Ratio Is Used as a Proxy for Developmental Stage .....	140
Figure A.1 Genetic Sparse Labeling.....	149
Figure B.1 Bipartite Matching and Iterated Heuristic Transformation.....	154
Figure C.1 Construction of the Optical Light Path .....	158
Figure C.2 IR Induction Optimization and Registration Methods for SPIM.....	162
Figure D.1 <i>ptr-10</i> regulates IL sheath lumen formation .....	166
Figure D.2 bHLH transcription factors regulate <i>ptr-10</i> expression .....	168
Figure D.3 <i>ns2870</i> affects glial reporter expression specifically in the CEP sheath .....	170
Figure D.4 <i>ns2870</i> is an allele of <i>bath-43</i> .....	171
Figure D.5 Function and Localization of <i>bath-43</i> .....	174
Figure D.6 <i>bath-43</i> Mutants Show Excessive Matrix Accumulation in Sensory Channels.....	176
Figure D.7 Strategy for <i>bath-43</i> Transcriptome Analysis in the CEP sheath .....	181

## List of Tables

Table 1: Simulation Results of Heat Distribution during Pulsing .....	45
Table 2. Reporters with Sparse Expression in neural and glial precursors at AB128 .....	73
Table 3. Embryonic and Postembryonic Imaging for <i>sax-3</i> and <i>vab-1</i> mutants.....	102
Table 4. Neuron Types Labeled after Genetic Sparse Labeling .....	149
Table 5. Developmental Cell-Stages and Performance of Matching Algorithms .....	152
Table 6: Interactors with <i>bath-43</i> in Yeast Two-Hybrid Screen.....	178
Table 7: RNA-seq of Isolated Cells from <i>bath-43</i> vs. Wildtype .....	182

## Chapter 1: Introduction

During development, cells undergo a highly orchestrated sequence of changes in order to achieve their proper function in a mature system; cells are generated through cell divisions, migrate through tissues by forming temporary adhesive contacts, develop specialized projections, and form functional cell-to-cell contacts. The coordination of these events is highly critical in the nervous system, where cells must connect to each other with precision in order to form functional neural circuits. Understanding how neurons faithfully achieve this connectivity, in the context of neighboring cells and guidance factors, is a central challenge in neuroscience.

A commonly used approach to visualize neurite growth is to acquire static images from fixed specimens at various time points and infer a developmental trajectory. Indeed, Ramon y Cajal made use of this strategy to catalog the structure of cells in the nervous system by light microscopy of fixed tissue<sup>1</sup>. This work laid the foundation of modern neuroscience, and his insights illustrate the power of this approach. Among his many prescient hypotheses, Cajal predicted the directionality of nerve impulses traveling from dendrites to axons, and even the function of the neuronal growth cone; he reasoned that the diversity of amoeboid shapes at axonal terminations in the chick spinal cord were a response to cues in the external environment as axons navigated to their targets.

Modern advances in neuroscience have moved past Cajal's static cataloging of brain structure and allowed live imaging of the dynamic structure of the nervous system. This approach reveals the time course of the developmental process. For example, whereas Cajal noticed the presence of spines on dendrites during development, only

recently have longitudinal live imaging studies demonstrated that these spines are highly dynamic<sup>2,3</sup>. Moreover, analyzing static images of development requires pooling data across structures to yield information about growth, but does not allow tracking the behavior of a single structure. Live imaging of retinal ganglion cells in zebrafish has revealed that axonal growth happens by a “trial and error” mechanism, where axonal branches are continuously extended and retracted over time scales of 20-30 min<sup>4,5</sup>. Analysis based on static images was only able to demonstrate that arbors grow larger over time. Thus live imaging is critical for a detailed characterization of development.

## **1.1 Live Imaging of Neuronal Development**

### **1.1.1 *In vitro* imaging**

Visualization of neurite growth in intact, living specimens is a challenge for most model systems, as tissues are often thick and not optically transparent. Alternate methods have been developed in cultured cells, tissue slices and organ explants as a proxy for *in vivo* imaging. Remarkably, even in *in vitro* conditions, neurons can polarize to form axons and dendrites, and later establish functional synaptic contacts.

Cultured samples in particular are thin and easily imaged, and brightfield or Normarski differential interference contrast (DIC) microscopy is often sufficient for visualization if cells are well separated. This approach was used by a number of pioneering studies of axon guidance which confirmed the “chemoaffinity” hypothesis. Proposed by Roger Sperry in 1963<sup>6</sup>, this hypothesis states that axon guidance is governed by attraction or repulsion to diffusible substances that form a gradient from start to destination. Time-lapse observations of explanted or cultured neurons revealed how

growth cones respond as they are challenged with other cells, purified membranes, or purified proteins. For example, to test the idea of the chemoaffinity hypothesis in retinotectal projections, explants from the temporal region of the chick retina, which normally targets the anterior region of the tectum, were given a choice to grow on membranes from anterior and posterior regions<sup>7</sup>. This “stripe” choice assay demonstrated that neurons were able to correctly target the anterior membranes, and subsequent experiments identified Ephrin as the molecule mediating this interaction<sup>8,9</sup>. *In vitro* experiments have also revealed the roles of several other guidance molecules. For example, the attractive factor Netrin causes growth cones to turn towards a local source, whereas the repulsive activity of the Semaphorins causes growth cone collapse at high levels<sup>10, 11</sup>. As cultured cells are accessible to a variety of labeling strategies, more recent studies have made use of timelapse imaging to characterize the remodeling of neuronal cytoskeletal architecture, which can be labeled by synthetic microtubule-binding fluorescent molecules or with advances in genetic tools, DNA expressing fluorescently-tagged proteins. Time-lapse observations of fluorescently labeled microtubules have shown that microtubule rearrangements occur in response to external signals and are important for growth-cone steering<sup>12,13</sup>.

Although powerful assays have been developed for cultured neurons, these studies do not always recapitulate *in vivo* developmental processes. First, while exogenous factors have the ability produce phenotypic effects in a controlled *in vitro* environment, this does not mean that they actually govern the equivalent process *in vivo*. Secondly, *in vitro* environments cannot recreate the many complex spatial and temporal cues that growth cones encounter *in vivo*, and therefore, understanding how the history

and environment of a given cell are integrated to generate a complex axon growth pattern requires direct visualization of a developing neuron in its native environment.

### **1.1.2 *In vivo* imaging**

Several technological advances have contributed to the availability of *in vivo* imaging - first, genetically encoded labels allow visualization of subsets of cells, without perturbation or injection with potentially toxic dyes, and secondly, new imaging techniques allow visualization of cellular dynamics at higher depths into tissue and over long durations, with minimal toxicity.

In mammals, *in vivo* imaging of neuronal development is a major challenge. In postnatal mammals, complex techniques are required to immobilize the animal during imaging, and only superficial sections of the brain can be accessed<sup>14, 15</sup>. Moreover, much of neuronal wiring occurs during embryonic development, which is largely inaccessible. Only very recently have tools been developed to image embryos *ex utero*, though these studies have not studied any aspect of nervous system development<sup>16, 17</sup>.

Model organisms that are small and optically transparent, such as zebrafish, *Drosophila*, *Xenopus*, and *C. elegans*, are the simplest systems for *in vivo* imaging, as the entire organism can be accessed and sample preparation is relatively straightforward. For example, single-neurite tracking with *in vivo* imaging in zebrafish revealed a novel role for the Robo receptor in error correction, which had previously been thought to have a single role in axon repulsion from the midline<sup>18</sup>. Several recent studies have characterized large-scale growth dynamics of neuroblasts in zebrafish and *Drosophila*, with the use of single-plane illumination microscopes, which are highly light efficient

(described in 1.6). In *Drosophila*, SPIM microscopy of the entire embryo was used to characterize division patterns throughout the embryo, and specifically the migration, delamination, and division of neuroblasts that lead to the birth of mother ganglion cells<sup>19</sup>. Pan-neuronal membrane-labeled markers were also used to observe the gross formation of the central and peripheral nervous system, and labeling in a sparse subset of neurons revealed active extension and retraction of filopodia during guidance to their targets. In zebrafish, cell divisions and migrations of ~10,000 cells were recorded using this microscope and nuclear positions were tracked over the first 24 hours of development<sup>20</sup>. Importantly, despite the comprehensive nature of these datasets, neither of these studies have attempted to characterize the dynamics of single cells with respect to their final trajectories or surroundings in the embryo.

## **1.2 *C. elegans* as a model for studying neurodevelopment *in vivo***

*C. elegans* is a fertile organism to study how neural circuits assemble *in vivo*. The embryonic nervous system of *C. elegans* contains only 56 glia and 222 neurons, most of which form synaptic contacts in a “brain”-like central neuropil called the nerve ring (Figure 1.1). Axons in the nerve ring form a bundle circumnavigating the pharynx and make *en passant* synapses. In route to the nerve ring, some neurons travel through bundled (or single-neuron) tracts to join with processes from other neurons (e.g. the amphid commissure). The largest longitudinal bundle is the ventral nerve cord (VNC), which contains processes from over 40 cells and contains mostly motor and interneurons; a comprehensive characterization of VNC development was performed through serial time-lapse electron micrographs of the embryo<sup>21</sup>. Genetic screens in the VNC have also yielded several evolutionarily conserved families of ligands and receptors that participate

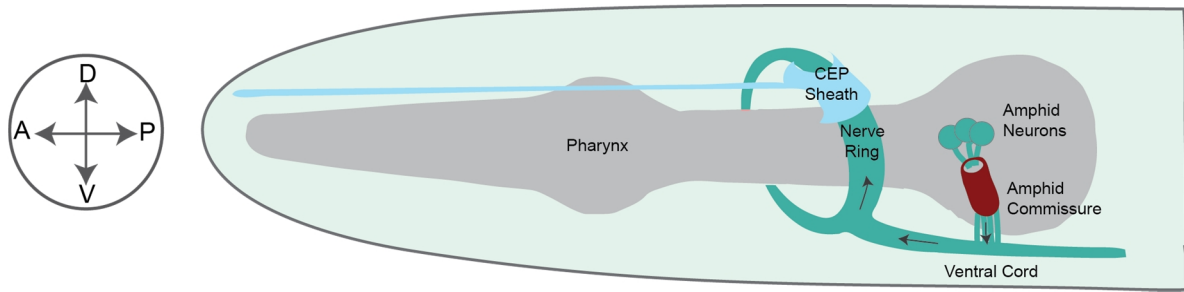


**Figure 1.1 The *C. elegans* nerve ring.** The *C. elegans* nerve ring wraps around the pharynx of the animal. Some axons travel through commissures in route to the nerve ring; the placement of the amphid neurons and amphid commissure are shown (arrows depict the direction of axon growth). The CEP sheath glia encircle the nerve ring – one is depicted but four exist to cover all quadrants of the structure. Axons in the ventral cord travel longitudinally.

in axon guidance, including UNC-6/Netrin and its receptors UNC-40/DCC/Frazzled and UNC-5<sup>22–24</sup>, and Slit and its receptor Robo/SAX-3<sup>25,26</sup>.

Due to the high spatial complexity and large number axons of making contact within the nerve ring, no comprehensive study has been undertaken to understand dynamics of nerve ring assembly, and little is known of how this structure assembles. Studies of signaling molecule expression and mutants have provided some insights into the components that are likely to guide nerve ring formation. The AVA and AVB neurons have been proposed to be pioneers based on early expression of Netrin, a gene known to be expressed by the pioneers of the ventral cord<sup>27</sup>. Studies of Wnt signaling have suggested that the *C. elegans* neuron classes SIA and SIB may be pioneers based on their ability to rescue defects in the placement of the entire nerve ring<sup>28</sup>. Interestingly, glia may be an early and important component of nerve ring assembly; the CEP sheath glia ensheath the nerve ring (Figure 1.1), and release Netrin throughout embryogenesis. Moreover, ablation of the CEPsh results in large NR defects, causing abnormal axon guidance and nerve ring placement<sup>27,29</sup>. The ILsh glia also extend endfeet to the NR that



make contact with axons within the neuropil, and have also been shown to express Netrin during this stage<sup>27</sup>. A recent study in our lab using sparse embryonic reporters has confirmed early roles for the CEPsh and the sublateral neurons through embryonic imaging and genetic rescue studies (Rapti et al., submitted). The guidance of most cells entering the NR remains to be explored, and determining the existence of “pioneers” or cell-cell dependencies will require a comprehensive characterization of all components.

In addition to the limited size of the nervous system, *C. elegans* has a number of other attractive features for a comprehensive study of CNS development. The invariant lineage determines the location and timing of cell generation<sup>30,31</sup>; by lineage tracing, the same cell can be identified and tracked across organisms, which facilitates comparison of individual cells. In addition, the 3D structure of the mature nervous system has been characterized at high resolution by electron microscopy, which delimits the endpoint morphologies associated with each cell. These studies have revealed that each neuron has simple, identifiable branching structures<sup>32</sup>. The simplicity and stereotypy of the *C. elegans* circuitry creates a unique opportunity to study real-time wiring decisions and correlate them to well-defined final anatomical structures.

Embryogenesis in *C. elegans* occurs over approximately 14 hours at 20°C and is divided into two main stages (Figure 1.2): (1) During the proliferation stage (0-330 minutes post fertilization/m.p.f.), a single-cell zygote divides into approximately 550 undifferentiated cells. Gastrulation causes short-range shuffling of precursor cells to internalize germline, endodermal, and mesodermal precursors. Most neurons in *C. elegans* are generated from the AB precursor cell, which divides mostly synchronously at each round of divisions – generating 2<sup>n</sup> cells after each round of divisions (approximate

times for AB<sup>64</sup>, AB<sup>128</sup>, AB<sup>256</sup> are given in Figure 1.2, and most cells will divide one subsequent time). Interestingly, the overall pattern of which precursors produce which cells is essentially mosaic, with sister cells often having different functions; similarly, most neurons form left-right homologs, although some form through lineage symmetry, which may require cells to migrate substantially to match their left-right pairs in the embryo. Others form pairs based on symmetric birth location<sup>33</sup>. (2) Subsequently, morphogenesis takes place (330-800 min), in which cells fully differentiate, migrate to their final positions, and form organs before hatching. During morphogenesis, the embryo begins to curve (bean stage) and elongate within the eggshell, following a sequence of characteristic shapes (comma, 1.5-fold, 2-fold, 3-fold). The embryo begins to twitch in the eggshell at ~430 minutes post fertilization,

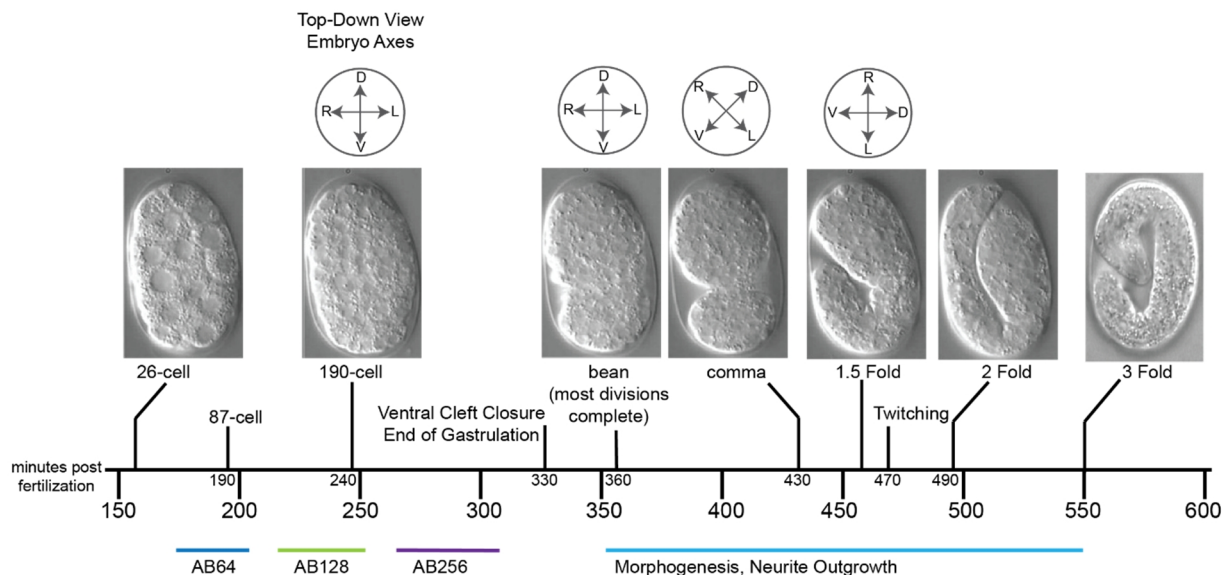


**Figure 1.2 Timeline of *C. elegans* embryogenesis.** Proliferation occurs from 0-360 m.p.f. and morphogenesis begins at the bean stage, when the major organs form and neurite outgrowth begins. Most neurons are derived from the AB lineage. Twitching of the embryo begins at 470 m.p.f. Soon after the onset of morphogenesis, the embryo rotates 90° within the eggshell (shown with the top-down views above the image).

Work from our lab suggests that much of nerve ring development may occur over ~150 min, a small fraction of the total time of embryogenesis; imaging with pan-cellular reporters and electron micrograph studies of embryos have further confirmed that prior to the bean stage, the nerve ring cannot be visualized, but many axons have grown into the rudimentary nervous system prior to the late 1.5 fold stage (Rapti, et al., submitted). Moreover, the twitching of the embryo at the 1.5 fold stage may indicate that a rudimentary nervous system has been formed.

### **1.3 Technical Challenges in Studying Embryonic Nerve Ring Assembly**

Though the nematode nervous system is simple, technical limitations have prevented a complete understanding of embryonic neurodevelopment in *C. elegans* thus far. There are three main technical challenges:

#### **(1) Identifying neuroblasts and glioblasts in embryos requires lineage tracing.**

Postembryonically, individual neurons and other cells can be identified in adult animals based on their unique morphology and relationship to anatomical structures. However, embryonic cells have not acquired their final morphological characteristics, and simple anatomical landmarks to distinguish cells in the embryo do not exist. Lineage tracing, from the 4-cell stage until the final division, will unambiguously identify cells and can be done by eye. However, this requires significant manual effort to trace the divisions of cells over >6 hours. Recently, a system for computer-automated cell lineage tracing allows identification and tracking of cells with minimal manual input<sup>31</sup>. I also describe a simplified strategy to identify a subset of neuroblasts without lineage tracing in Chapter 3.

**(2) Imaging strategies to visualize neurodevelopment over long periods of time have competing demands.** First, embryos are small (~40  $\mu\text{m}$  in the longest axis) and as described above, neurites are sub-diffraction limited (<200 nm). Therefore, high spatial resolution is required to see subcellular structures, necessitating bright fluorescence signals. At the same time, however, embryos are highly photosensitive, especially in GFP wavelengths, which limits the amount of time one embryo can be imaged, and small structures bleach signal rapidly. These challenges require highly light efficient imaging. A second consideration is that neurodevelopment continues after the onset of muscular twitching, and traditional confocal microscopes have difficulty capturing images without incurring significant motion blurring. This is a significant challenge in our own studies and is addressed in Chapter 7. New microscopy tools, such as light-sheet microscopy, address the imaging challenges described above.

**(3) Most embryonic reporters are expressed widely, and therefore cannot be used for labeling and tracking the growth of single neurites, or for driving gene expression selectively.** This problem is compounded by the fact that neurites in the *C. elegans* embryo are subdiffraction-limited in size (<200 nm) and fasciculate into common structures like the nerve ring, ventral nerve cord, and lateral commissures. This prevents resolution of bundled neurites even when very sparse labels are used. Commonly used genetic intersectional strategies, utilizing recombinases or split fluorophores, cannot be applied to the embryo because the speed of development is very rapid, as I describe later in the chapter. Neurite growth can happen as early as 40 minutes after the final cell division; thus expression of a label must happen within this short window of time to achieve specific labeling.

Developing a method to resolve this challenge is the focus my thesis work. In this work, I present a method, using an infrared laser, for reproducible heat-dependent gene expression in small sublineages (1-4 cells) without radiation damage. I show that this system can be used to label and track single neurons during early nervous-system assembly.

First, I briefly describe tools for lineage tracing and selective plane illumination microscopy (SPIM) with respect to studies in *C. elegans*, as they will be essential for future, large-scale characterizations of the nerve ring. During the course of my studies I performed proof-of-principle work to integrate these tools with infrared-laser labeling (detailed in Appendix B and Appendix C). As developing a tool for sparse labeling is the focus this work, in the subsequent section, I highlight strategies used across model organisms to achieve single-neuron labeling.

#### **1.4 Automation of Lineaging in *C. elegans***

The complete, invariant cell lineage of *C. elegans* was initially delineated by John Sulston with the use of DIC microscopy, which relies only transmitted light. To gather quantitative information about cell position and divisions in time and map gene expression onto the lineage, Bao et al. developed tools for automated lineage analysis<sup>31</sup>. The four-cell stage (~75 m.p.f.) is a simple starting point for lineaging, both through manual and automated methods, due to easily identifiable asymmetry between cells.

To perform automated lineage analysis, image volumes of embryos labeled with ubiquitous fluorescent protein-histone fusions are acquired every 1-2 minutes with confocal imaging. A significant challenge is acquiring high signal-to-noise images for

automated lineage analysis without compromising embryo viability. Segmentation of nuclei is relatively straightforward in early time points, when nuclei are well separated from their neighbors and can be identified with simple 3D maxima filters; subsequently, segmented cells are linked and divisions are identified by proximity and morphology of cells between time points<sup>31</sup>. Identification of cells becomes more challenging as development progresses, and recent algorithms have used more sophisticated algorithms to identify and track divisions to early morphogenesis when most of the cell divisions are complete<sup>34,35</sup>. According to a recent study, manual editing of the entire lineage through the final division (550-600 nuclei) with recent software improvements only requires 8-16 hours<sup>36</sup>, while a recently published semi-automated tool requires nearly 3 weeks of manual curation per embryo<sup>37</sup>. Software accuracy of these new automated tools is very high (>99%) at early stages, although even infrequent errors, particularly early in the lineage, will propagate. Thus, all methods require some degree of manual curation.

Published tools perform processing of images after acquisition. Currently, tool development is underway to create a real-time version of the lineaging software (P. Shah, Z. Bao, personal communication), which allows for identification of cells as the embryo is developing. This method will allow automated optical perturbations (including ablation, IR-induced labeling, and photoconversion), and will be important to make the entire embryo accessible to these strategies (discussed further in Chapter 7).

In this thesis, I use a simpler strategy to identify specific cells that does not require lineage tracing, by using nuclear markers that are expressed in small subsets of cells and have been previously characterized through lineage studies<sup>38</sup>. This strategy is described in Chapter 3. I also consider methods to identify all cells in the wildtype embryo based on

their relative position (rather than lineage), given that recent studies have demonstrated that the variability in cell position between wildtype embryos is low. This method achieves ~80% identification of cells at very specific stages of development in previously characterized data sets (See Appendix B for details). This work was performed as a proof-of-concept, and I did not attempt to implement this strategy with IR-labeling.

### **1.5 Imaging Techniques for Studying *In Vivo* Development**

Confocal microscopy is commonly used for *in vivo* imaging. Confocal microscopy uses a high N.A. objective to create a diffraction-limited spot in the imaging plane, also illuminating the area above and below the laser focus. A pinhole partly blocks out-of-focus emission, thereby sectioning the sample. Laser-scanning confocal microscopes serially excite spots on a sample, requiring high laser intensities for fast imaging since the dwell time on each pixel is small. Spinning disk confocal microscopy overcomes this issue by parallelizing this process, splitting the laser to excite many separate points on the image plane and feeding the resulting fluorescence into a set of matched pinholes. The time spent exciting each pixel can therefore be increased, leading to gentler imaging. Though both strategies are commonly used for imaging *C. elegans* embryos and are used for imaging labeled cells in this work, both phototoxicity and photobleaching are major concerns as the entire sample is illuminated in the z-axis to acquire a single section.

Selective plane illumination microscopy (SPIM), a newly developed imaging technique, is far more light-efficient and therefore can be used for acquiring images with higher temporal resolution. SPIM achieves optical sectioning by exciting fluorescence only where it is needed for detection. In this setup, the excitation light is focused into a sheet by a different objective at a 90° angle to the detection objective, thereby

illuminating a thin section around the focus. For studying *C. elegans* embryogenesis, SPIM offers a number of advantages: (1) Each plane is illuminated in succession, rather than by individual pixels, and acquisition speeds can be very high with rapid, sensitive cameras, (1 volume/2 seconds)<sup>39</sup>, allowing blur-free imaging after the onset of twitching. (2) The system is much more light-efficient, allowing more frequent imaging without compromising embryo health. During my thesis work, a graduate student in the lab, Peter Insley, built a SPIM microscope in the lab for imaging *C. elegans* embryos. Due to the different sample mounts (slide mounts for use with oil immersion objectives vs. sample chamber with water immersion objectives), we were unable to transfer embryos easily from the IR labeling microscope to the SPIM microscope for imaging. We worked to integrate our systems to allow for induction and imaging on the same microscope, and our progress is given in Appendix C.

A few recent studies have applied SPIM to studies of *C. elegans* neurodevelopment<sup>39-41</sup>. As only a few sparse markers for neurons prior to neurite outgrowth are well-characterized, these studies performed lineage analysis on a promoter labeling the ALA, CAN, AIY, and RMED neurons prior to neurite outgrowth. Previously unknown dynamics of neurite growth and cell migration have been revealed in these studies. First, these studies have shown that neurons exhibit dynamic exploratory behaviors during neurite outgrowth. For example, after the ALA neurite circumnavigates the nerve ring and turns posteriorly, time-lapse imaging from SPIM shows that the ALA growth cone bifurcates and pauses for 10 minutes before continuing growth<sup>39</sup>. This behavior suggests that certain locations in the trajectory of neurons may serve as guidance choice points. Secondly, these studies have demonstrated that neurons can



undertake different modes of outgrowth to grow different regions of one axon. diSPIM imaging revealed that the AIY neuron grows the majority of its distal process in the nerve ring by forward extension, whereas the proximal part of the process, outside the nerve ring, is grown by retrograde extension<sup>41</sup>. Thirdly, blur-free SPIM microscopy has been combined with new computational tools to untwist and compare embryos after twitching and during elongation<sup>40</sup>. By comparing the migration patterns of neurons with the neighboring hypodermal seam cell during elongation, it was shown that ALA and AIY move at the same rate as the seam cell nuclei, suggesting a mechanism by which they are passively “dragged,” whereas CAN neurons migrate at a higher rate than surrounding cells, suggesting an active process. This tool provides a framework for combining data from multiple embryos, and strategies to implement this tool and others are described in the final chapter (Chapter 9).

## **1.6 Sparse Labeling Strategies Across Model Systems**

Visualizing individual cells is essential for understanding the developmental principles of neural circuitry. This problem was recognized even by Ramon y Cajal, who used Golgi’s staining method to systematically characterize the morphology of cells in the vertebrate and insect nervous systems<sup>1</sup>. Golgi’s staining protocol leads to the formation of black precipitates in a random subset of cells, and allowed visualization of individual neurons for the first time. This advance allowed Cajal to reject “reticular theory,” the idea that nerve processes were fused together into a giant net, in favor of “cell theory,” the idea that neurons were the structurally and functionally independent units of the nervous system. Golgi staining remains a benchmark for sparse labeling, but it has several limitations, chief among them that the stain can only be used in fixed tissue. A

subsequent advance was the discovery and use of “vital dyes,” which label cells without killing them. Lipid-soluble carbocyanine dyes were used as tracers of neurons, allowing tracking of growth cones of retinal axons through the optic chiasm<sup>42</sup>, and lineage tracing of neural tissues in chick embryos<sup>43</sup> and *Xenopus*<sup>44</sup>.

Genetic markers have now largely superseded cell marking using dyes or other stains, most importantly since the discovery of green fluorescent protein (GFP) from the jellyfish *Aequorea victoria*<sup>45</sup>. In this section, I first describe strategies in which sparse labeling is achieved solely through genetics. These strategies utilize expression of transcription factors (e.g. GAL4-UAS) and recombinases (e.g. Cre and Flp) by well-defined regulatory elements to produce deterministic (intersectional) or stochastic labeling. Earlier strategies have utilized single-color labels, but more recent strategies, like Brainbow, increase the number of labels such that each cell can be distinguished from its neighbors based on its unique color profile. This strategy provides an advantage of allowing imaging from many cells within the same sample. Then, I discuss optical tools, which use lasers to produce single-cell selectivity, without the need for cell-specific drivers. Photoconversion is a technique used commonly for this application. I also review newly developed light-responsive effector proteins, which may be of use for targeted labeling in the near future. Finally, I discuss recent studies that utilize an infrared laser to induce expression via heat-responsive elements, which my thesis work is based upon. In many cases, I considered applying these strategies to achieve sparse labeling in the *C. elegans* embryo, and so I discuss their applicability and any preliminary data I generated.

## 1.6.1 Genetic Strategies for Sparse Labeling

### 1.6.1.1 Transcription Factors for Intersectional Expression

Labeling can be limited to sparse cells in a deterministic fashion based on overlapping expression patterns of different transcriptional sequences. One method to achieve cell-type specificity is through the use of transcription factors, which are already capable of producing logical “AND” and “NOT” operations to specify the expression of genes during development.

The GAL4-UAS system is one implementation of this concept, and is commonly used in zebrafish and *Drosophila*<sup>46, 47</sup>. The GAL4 transcription factor is typically driven by a cell or tissue-type specific promoter sequence, and the UAS (upstream activating sequence) serves as the binding site for GAL4, driving expression of a downstream effector gene (Figure 1.3A). In this simple configuration, the system does not provide any additional spatial specificity, but one major advantage is that the signal is amplified due to the added strength of GAL4 transcription. To increase spatial control, a few variations have been developed. GAL80, the yeast-repressor of the GAL4 gene, has been shown to function in *Drosophila*, thereby creating a logical “NOT” operation. In a split GAL4 system, two parts of the GAL4 gene are expressed under different promoters, such that the GAL4 function is reconstituted only in the overlapping set of cells, producing a logical “AND” operation<sup>48</sup>. More recently, systems with even more complex opportunities for regulation have been developed. The Q-system has been adapted from *Neurospora* for use in *Drosophila*<sup>49</sup>, and more recently in *C. elegans*, where it is the first reported transcriptional binary system<sup>50</sup>. In this system, QF serves a transcriptional activator, analogous to GAL4, and QS, like GAL80, serves a repressor. Interestingly,

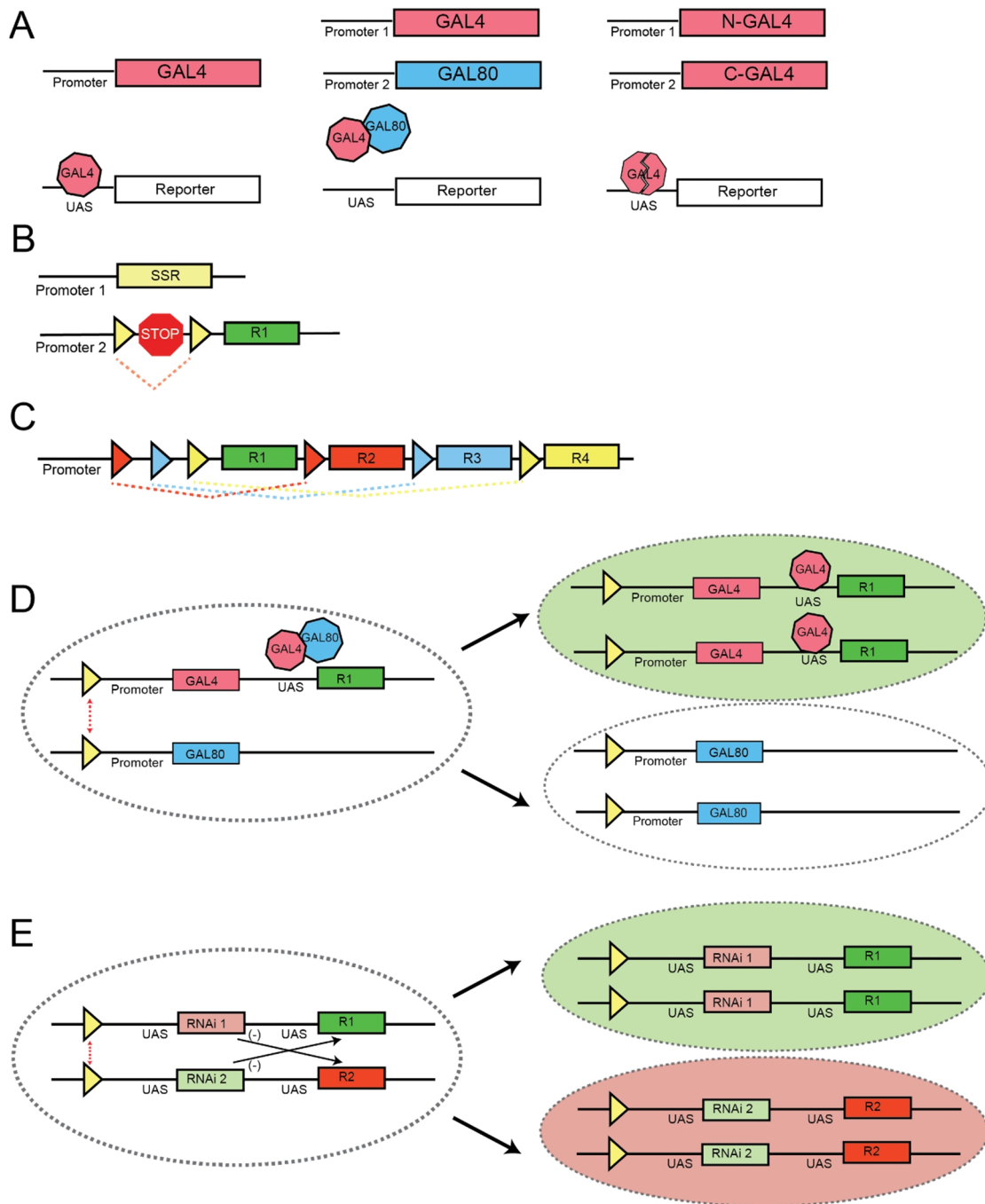


**Figure 1.3 Genetic Strategies for Sparse Labeling.** (A) GAL4 Binary System. GAL4 activates transcription and is suppressed by GAL80. (B) Recombinases excise the sequence between two lox sites (triangle). (C) Brainbow. Recombination occurs only between heterospecific lox sites. (D) MARCM strategy. Recombinases cause interchromosomal exchange, causing segregation of identical chromosome arms during mitosis. This relieves GAL4 suppression. (E) Twin-spot MARCM. RNAi repressors block expression of reporters on opposite chromosomes. After SSR-mediated chromosome exchange, reporters are expressed.

quinic acid fed to the worms relieves QS suppression, thus providing an additional level of temporal control, with de-repression observable after ~6 hours.

We explored the use of the Q binary system in *C. elegans* to create a feed-forward transcriptional loop, to amplify signal from a transient, or weak heat pulse after laser induced heat shock. We developed a transgenic line containing the constructs: heat shock promoter::QF, UAS::GFP, and additionally UAS::Q to provide self-sustaining amplification. Such a strategy to produce persistent expression from a transient tissue-specific promoter has been used in zebrafish with GAL4<sup>51</sup> (termed “kalooping”). Our transgene also allowed us to measure the kinetics of the process in the embryo and for intersectional strategies. We found that the kinetics of GFP expression after a heat pulse was too slow to be used for embryogenesis (5-6 hours), and secondly, that GFP expression was not maintained after heat shock. Thus, the Q system is not applicable for studies of early *C. elegans* embryogenesis.

#### **1.6.1.2 Site-Specific Recombinases for Intersectional Expression**

One feature of combinatorial transcriptional systems is that all components (split activators, repressors, etc) must be actively generated in order to produce a given expression pattern. On the other hand, strategies using genetic switches change the genetic makeup of the cell, and this change is maintained in the cell and also inherited by progeny, providing a convenient record of a cell’s developmental history, particularly useful for lineage tracing.

Site specific recombinases (SSRs), such as Cre and FLP recombinase (first identified in bacteria and yeast respectively), perform DNA strand exchange between two

short recognition sequences possessing sequence homology. Recombinases are frequently used to drive expression in an overlapping set of cells, using a strategy called FLP-out in *Drosophila*<sup>52</sup> and commonly used with Cre recombinase in mice and more recently in *C. elegans*<sup>53</sup> (Figure 1.3B). Notably, recombinase systems can integrate behavior of the two promoters in time - the excision event can be driven by transient expression of recombinase by the first promoter, causing the second promoter to drive expression, even if the expression of the two driving sequences never overlap in time. I explored the use of SSRs for intersectional strategies during *C. elegans* embryogenesis and found that after heat shock driven Cre expression, reporter expression begins after ~2 hours (Figure 2.1), which is sufficiently fast enough to be useful for this system, while for FLP-FRT these events appear to take longer (3-4 hours, data not shown).

#### **1.6.1.3 Random Labeling via Interchromosomal Exchange (MARCM)**

An elegant application of the GAL4 transcriptional system and SSRs was developed to label random lineages of cells in *Drosophila* by Lee and Luo in 2001<sup>54</sup>. Since then, this technique, termed mosaic analysis with a repressible cell marker (MARCM), has been used in many studies tracing lineage in complex neuronal circuitry (Figure 1.3D). Precursor cells heterozygously express a GAL4 and UAS reporter on one chromosome and the repressor GAL80 on the other chromosome. During mitotic recombination after the sequences are replicated, FLP recombinase is activated by heat shock, sometimes causing one chromosome arm containing GAL80 to be switched with the GAL80(-) arm. After segregation, one daughter will inherit no copies of GAL80, thereby relieving suppression of the reporter. Building on this strategy, mutant sequences can be genetically linked to the activator allele; thus after recombination and segregation,

labeled cells will be homozygous mutant, thereby enabling mosaic analysis. A further improvement on this strategy, termed twin-spot MARCM, labels both daughter cells in different colors after a recombination event, allowing comparison of cell fate and unambiguous lineage determination. The expression of membrane-bound markers (CD8::GFP or CD2::RFP) requires the release of microRNA suppressors (miR-CD2 or miR-CD8), which are found on the opposite chromosomes from their target (Figure 1.2E). Only after recombination and segregation into separate cells do the sister cells express differently colored fluorescent proteins <sup>55</sup>.

A recent study in *Drosophila* has demonstrated the power of twin-spot MARCM to unambiguously trace cell lineage in *Drosophila* <sup>56</sup>. In contrast to *C. elegans* where neurons proliferate exponentially via repetitive cell divisions, in *Drosophila*, neurons are added sequentially by neuroblasts, which undergo a series of asymmetric divisions. Each neuroblast divides to generate another neuroblast, as well as a ganglion mother cell (GMC) which divides once to produce two neurons. Using twin-spot MARCM, the lineage of anterodorsal antennal lobe was delineated at single-cell resolution. In each recombination, a single GMC-derived cell (the other neuron dies post-mitotically) is paired with a variable number of NB derived clones. By counting the number of NB clones for each labeling pattern, the exact point in the lineage which derived the GMC clone can be determined. Through this systematic analysis, it was shown that 40 antennal lobe projection neuron types arise in an invariant sequence from the original neuroblast <sup>56</sup>. This stereotyped development indicates that lineage determines specification in *Drosophila* even for diverse neuron types. Moreover, a dividing neuroblast contains

information about the number of previous cell divisions it has undergone in order to generate neurons with a specific sequential identity.

#### **1.6.1.4 Single-Color Random Labeling via Recombinase Excision**

With low levels of recombinase activity, excision events become less probable. As excision events produce a binary outcome (“on” or “off”), reducing the level of recombinase expression produces sparse labeling. This strategy has been employed in zebrafish with low levels of heat shock<sup>57</sup>, and in mice by the use of Cre-Estrogen-Receptor recombinase, which can be dialed exogeneously by the concentration dependent nuclear translocation of the ER in response to 4-OHT<sup>58</sup>. If the recombination event occurs prior to the final cell division, this strategy can be used for lineage tracing.

Given the challenges in employing the more complex multi-color labeling Brainbow technique to *C. elegans* (described below), and given that the kinetics of Cre-lox recombination in the embryo was relatively short (~2 hours, Figure 2.1), we applied a strategy similar to MaZe<sup>57</sup> (mosaic analysis in zebrafish) to *C. elegans* embryos (Appendix A). We found that there were two main challenges with this approach: (1) with low levels of heat shock, the Cre-lox reporter exhibited greater delays in recombination, such that in order to visualize cells at the beginning of morphogenesis, clones were very large (8-16 cells) preventing single neurite resolution, and (2) labeled cells appeared to be non-random, biasing towards sensory neurons, the pharynx, and gut, probably due to varying heat shock thresholds in tissues. Similar strategies that could improve this technique are described in Appendix A.



### **1.6.1.5 Multi-Color Random Labeling via Recombinase Excision**

In 2007, Livet et al. pioneered the “Brainbow” technique to label neurons stochastically with different colors by combinatorial expression of fluorescent proteins for the purpose of mapping neuronal connectivity in the mouse brain<sup>59</sup>. Over the past few years, Brainbow strategies have been adapted to other model systems, including flies, zebrafish, and *Arabidopsis*, and have also been used for studies of development and lineage tracing<sup>60–62</sup>. Unlike many of the previously described strategies, the use of multiple colors within one cell population allows the user to trace the behavior individual cells and visualize their interactions with neighboring cells. Single organisms contain information from all differentially labeled clones, and therefore methodology for merging data sets from many differentially labeled organisms or samples is not required.

The Brainbow strategy relies on Cre-mediated excision of DNA fragments using heterospecific lox sites (Figure 1.2C). Cre-mediated excision causes one such event to occur randomly, arbitrarily positioning one fluorescent protein closest to the promoter. Color diversity is increased by having multiple copies of the transgene—either by multiple insertions into the genome or through techniques that introduce many copies as extrachromosomal elements. However, increasing the hues that are present can require sophisticated image processing to trace the processes of individual cells by separating the ratios of the fluorescent proteins expressed.

Since the advent of the technique in 2007, several improvements (e.g. maximizing color diversity, adding antibody amplification, refinements for applications to other model organisms) have been described, but here I focus on a couple of recently published advances. One elegant solution to the issue of color discrimination is to increase the

dimension of labeling by targeting fluorescent proteins with different subcellular localizations<sup>63</sup>. For example, two copies of transgenes with three fluorescent proteins will generate 6 possible hues, which are simple to discriminate. Having two cytoplasmic-expressed transgenes and two nuclear-expressed transgenes creates  $6 \times 6 = 36$  possible combinations, which are technically no more difficult to separate than the original 6 because they are clustered in different compartments. By contrast, increasing the number of cytoplasmic transgenes to 4 requires discrimination within the same compartment of 26 hues, both a smaller number and also more challenging. Although Brainbow has predominantly been used for labeling cells, recent strategies have coupled color to the expression of rescuing or dominant negative genes through fusion or tandem expression with a fluorescent protein. This strategy allows genetic mosaic analysis in colored clones. The “Brother of Brainbow” (BOB) approach was applied in *Arabidopsis thaliana*<sup>62</sup>. In this study, the function of the retinoblastoma-related gene (RBR) was coupled to the loss of a RB-YFP rescuing transgene, leading to expression of other red and blue FPs. Clonal cells marked by blue or red proliferated more, indicating a conserved role for RBR across species.

Although Brainbow was originally used for post-developmental brain connectivity studies, recent work has adapted its use to the study of development alongside *in vivo* time-lapse imaging, particularly in *Drosophila* and zebrafish. A epithelial-specific version applied in zebrafish (“skinbow”) along with semi-automated tracking of cells has allowed visualization of regenerating skin after major amputation injuries over several hours<sup>64</sup>. Improvements in *Drosophila* have allowed live imaging and lineage studies of entire tissues such as the wing disc<sup>65</sup> and the cornea<sup>66</sup>.

Importantly, no study, to our knowledge, has applied these tools to studying nervous system development in any intact living organism.

Initially, we considered an approach for labeling via a Brainbow strategy in *C. elegans*. There are a number of technical limitations, specific to *C. elegans*, which make this strategy not applicable. The foremost limitation relates to the fact that neurites in the *C. elegans* embryo are smaller than other organisms. As visualized by electron microscopy, neurites in *C. elegans* are ~100 nm in width in the embryo, whereas the limitation of fluorescence microscopy is roughly 200 nm. Since most neurons in *C. elegans* grow into overlapping structures, the signal from a single pixel will be the contribution of a bundle of labeled cells, preventing resolution of single neurites. Secondly, the time between the final division in *C. elegans* and the beginning of neurite outgrowth in *C. elegans* is very short (~40 min for early components, Figure 3.5). For cells that are related by lineage to be labeled differentially, the recombination event and labeling must occur within this window of time; however we measured the time for Cre-lox recombination in *C. elegans* to be ~2 hours for GFP (Figure 2.1). For color variants of fluorescent proteins, which Brainbow relies on, the maturation time is frequently even longer. Thus lineages will be labeled in the same color if early neurite characterization is desired.

#### **1.6.1.6 Random Sparse Labeling by Stochastic Regulatory Elements**

Though transcriptional elements usually produce deterministic expression, Thy1 regulatory elements, derived from a gene that encodes a small immunoglobulin superfamily member, produce stochastic labeling in neurons of mice. After tailoring the transcriptional sequence towards neuronal specificity, it was found that a wide variety of

expression patterns can result from genomic integration of the same Thy1 construct in mice<sup>67</sup>. Within these transgenic lines, there is a strong variation in the neuronal subpopulations that are labeled, and most surprisingly, Thy1-driven lines have the feature that individual neurons within a seemingly homogenous populations of neurons can show strong labeling, while adjacent cells do not show labeling. The mechanism producing stochastic labeling are not known, but is thought to be a result of insertion site and “positional affect variegation,” by which genes are inactivated in a mosaic fashion through differing juxtaposition with heterochromatin in different lines.

Thy1-XFP mice have become valuable tools to visualize neuronal development. Sparse labeling of accessible regions like the neocortex, alongside tools to image the same region of the intact cortex in live mice, have facilitated longitudinal studies of spine plasticity, since the same cells can be identified over days to months. For example, studies using these sparsely labeled transgenic mice have shown that dendritic protrusions of pyramidal cells in immature animals are highly dynamic, with filopodia and spines turning over nearly daily, whereas spines stabilize substantially in older animals<sup>14,15</sup>. Though this tool is widely in use in mice, transcriptional elements driving stochastic expression are only known for mice.

### **1.6.2 Optical Tools for Directed Cell Labeling**

The strategies above rely on genetic tools for directed or stochastic labeling of cells. Now I discuss a class of strategies that use the focusing power of optics to selectively label cells.

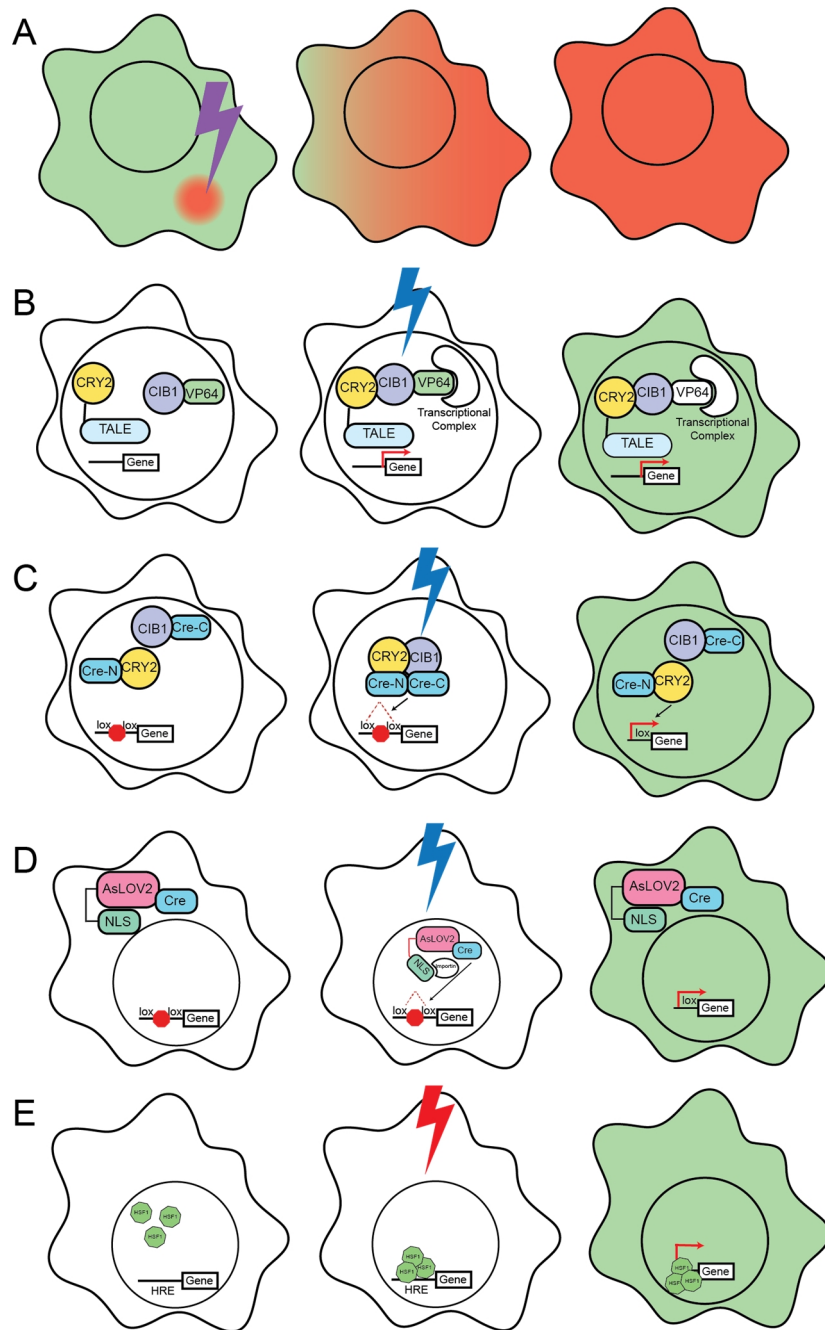


**Figure 1.4 Optical Strategies for Sparse Labeling.** (A) Photoconversion of Kaede or mEos2 with a UV laser (B) CRY2-CIB1 dimerization by blue light activates transcription (LITE) (C) CRY2-CIB1 interaction reconstitutes Cre, leading to excision, and expression. (D) AsLOV2 domain inhibits the NLS of Cre from accessing importin machinery. Under blue light, the conformation changes allowing nuclear import and excision. (E) IR Laser Induced Gene Expression. HSF1 is activated by heat from the laser, leading to gene expression downstream of heat shock response elements (HRE).

### 1.6.2.1 Photoconvertible Fluorescent Proteins for Optical Cell Marking

Photoconvertible fluorescent proteins undergo a chemical reaction upon excitation, resulting in an irreversible shift in their excitation/emission spectrum. These proteins are useful for cell tracking experiments, as the entire cell population can be labeled in the baseline fluorescence color (close to GFP for Kaede and mEos2), while the protein within a specific cell can be converted by a laser of the conversion wavelength (UV) (Figure 1.4A).

The converted protein distributes throughout the cell, such that it can be visualized with a different fluorescence profile (RFP) against the unconverted population. A recent study has used mEos2 to mark and track single oligodendrocyte glia progenitors in the zebrafish nervous system<sup>68</sup>. Interestingly, here photoconversion was achieved using a 440-nm pulsed Coumarin dye laser, which is also used in *C. elegans* for cell ablation, suggesting that a single-laser setup could be used simultaneously for photoconversion labeling and ablation.

A recent study has shown that photoconversion can be used in the *C. elegans* embryo to visualize morphogenesis of single neurons, demonstrating that single sensory neurons extend dendrites retrogradely<sup>69</sup>. This study highlights some of our considerations for applying this tool to a broader study. Photoconversion has a major kinetic advantage over genetic tools, because labeling occurs instantaneously; therefore, labeling can be performed post-mitotically without concern about resolving clonal populations of cells. Visible light at low-levels, unlike heat, as I discuss later, is non-toxic. However, there are a number of limitations. Unlike genetic tools in which production of the signal is ongoing from transcriptional activity, photoconversion produces a limited amount of signal,

making it difficult to use for long-term or high-frequency imaging; indeed, in dendrite extension studies, cells were reconverted every 15 min in order to compensate for bleaching of the signal and protein turnover<sup>69</sup>. Secondly, as neurite outgrowth overlaps with the period of twitching during embryogenesis, photoconversion is incompatible with labeling during this time period. Moreover, photoconversion requires the use of cytoplasmic labels (as opposed to membrane labels) for cell-specificity, which are not well-suited to visualizing cytoplasmically-poor neurites. Lastly, as photoconversion requires only single photons to convert the PC-FP to the labeled state, cells in the laser conversion path (above and below the plane of interest) can also be labeled, albeit to a lesser extent. This issue is mitigated with heat-based strategies, since activation only occurs when the light is sufficiently concentrated such that the temperature reaches above a certain absolute threshold. For these reasons, I did not pursue photoconversion strategies in this work.

#### **1.6.2.2 Optical control of visible light-sensitive effector proteins**

As one of the major disadvantages of photoconvertible proteins is the transient, limited signal produced, novel light-inducible proteins that can activate transcription could offer a potential solution to this problem, while maintaining the low-toxicity of visible light. The first instance of this system, light-inducible transcriptional effectors (LITEs), was described recently<sup>70</sup>. In this system, the cryptochrome 2 protein (CRY2) from *Arabidopsis thaliana* is fused to a customizable DNA binding domain (TALE), while the interacting partner, CIB1, is fused to an effector protein, such as VP16. In the absence of light, TALE-CRY2 binds DNA, while CIB1-VP16 remains inactive, and upon light activation, TALE-CRY2 recruits CIB1-VP16 to activate transcription of a downstream

gene (Figure 1.4B). To be useful for cell labeling applications, the system must be activated by brief pulses of light, and have little activation in the absence of light. In the original study, fold activations of ~20x were achieved over unstimulated cells, with mRNA transcript accumulation visible by half an hour after beginning light stimulation. Other studies have used the same CRY2-CIB1 system to generate a split Cre which is reconstituted upon blue light stimulation<sup>71</sup>. A very recent study has shown that brief stimulation of blue light (4 seconds) leads to excision of a STOP cassette and subsequent expression of GFP in ~20% of cells in cell culture, with minimal background labeling (<2%)<sup>72</sup>. We envision that light-activated Cre excision of a STOP cassette, using this strategy, could be employed in the *C. elegans* embryo for rapid labeling of cells (Figure 1.4C). To date, studies have not applied the CRY2-CIB1 system (either for transcription or for recombinase mediated activity) for single-cell, laser-induced perturbations.

Proteins that allow optical control of subcellular localization are another recently described technology. An optical tool for control of nuclear import has been described, which uses the LOV2 domain from *Avena sativa*<sup>73</sup>. By fusing an NLS sequence to the LOV domain, the NLS motif is prevented from binding nuclear import machinery in the closed state; upon blue light activation, the NLS is “uncaged” and becomes accessible. This tool has been shown to function selectively in single cells of the 4-cell-stage *C. elegans* embryo using a laser, creating reversible translocation of a LOV2-NLS-fluorescent protein fusion<sup>74</sup>. According to this study, translocation to the nucleus occurs within 30 seconds and is maintained until the laser is turned off, when it rapidly returns to the cytoplasm with the same kinetics. We considered a strategy of fusing the LOV2-NLS sequence to Cre recombinase, such that upon light activation it would translocate to the



nucleus to perform STOP cassette excision (Figure 1.4D). However, in our hands, after 488 nm laser excitation, we did not observe a large change in nuclear intensity of the ASLOV2-reporter fusion (<20%, data not shown), possibly due to a technical error. We were also concerned about baseline shuttling of protein to the nucleus, since even a small level of nuclear Cre can cause recombination events (D. Dickinson, personal communication); indeed only 3-fold increases in nuclear expression have been reported, which may not provide sufficient dynamic range. Reductions to the residual levels of nuclear activity would make this strategy feasible. The rapid kinetics, low toxicity of blue light, and use of non-endogenous proteins, which should not interact with the existing cell machinery, make these tools very promising for future strategies to label cells in *C. elegans*.

### **1.6.2.3 Laser-Mediated Gene Expression via the Heat Shock Response**

For inducing gene expression, the heat shock response has a number of attractive features: it is cell-autonomous, has little baseline expression with high upregulation after heat stress, and has rapid kinetics because its effector is a transcription factor. Studies illustrating the use of lasers to elicit the heat shock response have been performed in optically transparent organisms, such as *C. elegans*, *Drosophila*, zebrafish, and *Arabidopsis*<sup>75–78</sup>. These studies use transgenic animals with a heat-shock driven transgene present in all cells, and use the laser to drive targeted expression.

#### **1.6.2.3.1 Overview of the Heat Shock Response**

In order to cope with physiological and pathophysiological conditions that cause protein unfolding, cells mount the heat shock response, a highly conserved transcriptional

program which results in the synthesis of cytoprotective gene products termed heat shock proteins (HSPs). In general, HSPs function as molecular chaperones to fold nascent proteins or to refold proteins damaged by stress. Indeed, in addition to heat, the heat shock response can be activated in response to oxidative stress <sup>79</sup>.

In all eukaryotic cells, heat shock factor 1 (HSF1) is the master regulator of this response, altering transcription of downstream genes, like HSPs and proteases. Promoters for the various HSPs contain similar motifs, termed heat shock regulatory elements (HREs), consisting of inverted GAA repeats separated by two or more nucleotides. These HREs are bound by HSF1 directly and have been shown to be sufficient for the induction of genes upon heat shock <sup>80,81</sup>. In general, the heat shock response is thought to be cell-autonomous, although whole-animal regulation of the response has been observed in *C. elegans* <sup>82</sup>. Importantly, activation of HSF1 also causes repression of transcription and protein synthesis on a broader scale, and depending on the level of the stress, arrest of the cell cycle or stagnation of growth can result <sup>83</sup>.

Interestingly, although the function of HSF1 is highly conserved across organisms, the temperature thresholds at which HSF1 activation occurs varies substantially across animals, and even during the development of single organisms and in tissues across an organism. This leads to the question: How does heat induce activation of HSF1 and how is the temperature set point for activation established? There are two main hypotheses regarding this question. (1) HSF1 is a thermosensor itself. A recent biochemical study has shown that even in the absence of other chaperone proteins, the trimerization domain of HSF1 becomes more stable at higher temperatures, suggesting that HSF1 can directly sense and respond to temperature <sup>84</sup>. However, previous studies

have shown that expressing the human version of HSF1 in *Drosophila* cells sets the temperature threshold of activation to the *Drosophila* level, arguing against an HSF1 intrinsic threshold<sup>85</sup>. (2) The second model relies on the idea that HSP chaperone proteins act as negative regulators of HSF1 under non-stress conditions; under stress, they are titrated away from HSF1, allowing for activation to occur. In this model, a negative feedback loop maintains low activity of HSF1 at the baseline temperature, with a change from baseline resulting in a heat shock response. This model is consistent with results that show that activation temperature can be lowered by reducing cultivation temperature, and that knockdown of HSP70 or HSP90 leads to induction of the heat shock response<sup>86,87</sup>. Thus, the temperature requirements for HSF1 activation are likely to involve a combination of regulation, from the structure of the protein itself, to involvement of other proteins responding to unfolded proteins in the environment.

Despite numerous studies on these competing models, the mechanism by which temperature increase leads to heat shock activation is still poorly understood. Moreover, few studies have addressed how duration of heat stress or recovery periods between heating affect the strength of the response. For laser-mediated heat shock gene expression, defining these parameters (temperature required, duration) is crucial for creating an appropriate sub-lethal heating strategy. However, in the absence of this information, optimizations of laser-induced heat shock in past studies have largely been performed empirically, without reference to the actual temperature or duration of heating being generated. For reference, although conditions for whole animal *C. elegans* heat-shock vary widely, conditions usually range from 32-34°C over minutes to hours to elicit a heat shock response while maintaining cellular viability<sup>88</sup>.

#### 1.6.2.3.2 Early Studies Using a Blue Light Laser to Elicit the HSR

Early versions of this strategy used a pulsed 440-nm laser, commonly used for cell ablation, to elicit the heat shock response<sup>78,89</sup>. To prevent cell damage, the beam was attenuated using neutral density filters and glass slides. These reports used pulse lengths of a few nanoseconds at 3 Hz for 2-3 minutes. A few different lines of reasoning suggest that these conditions may cause a heat shock response through non-thermal mechanisms. First, a recent study performed dosage curves of power vs. induction frequency using 440-nm lasers, and found that the induction frequency stays around ~20% for power levels in a 10-fold range, which would not be expected with a heat-mediated response that typically occurs at a sharp temperature threshold<sup>76</sup>. Secondly, there appears to be no separation in power levels between conditions that cause sub-lethal heat shock and those that cause cell damage. Separately, the duration of heating suggests that the temperatures reached may be very high. As I demonstrate in Chapter 2 with simulations, heat diffusion in tissue occurs very quickly, such that with the length of laser pulses and frequency described, cells would only be heated for <10  $\mu$ s during the 3 minute heating courses.

Indeed, all early reports of this technique have noted several signs of damage after laser induction, although the statements are anecdotal and not quantified. In 1997, Harris and Honigberg used the technique to study the role of *mab-5* in causing Q descendant migration<sup>89</sup>. They note that the laser intensity required to produce the desired rescue often caused blocking or delaying of the subsequent cell division, and moreover, sometimes prevented the cell from migrating entirely, an effect independent of the heat-shock driven transgene. Though these studies demonstrate the power of this tool, it is

clear that characterizing wildtype development would be challenging, as some frequency of cell damage or aberrant cell behavior is unavoidable.

### 1.6.2.3.3 Studies using an Infrared Laser to Elicit the HSR

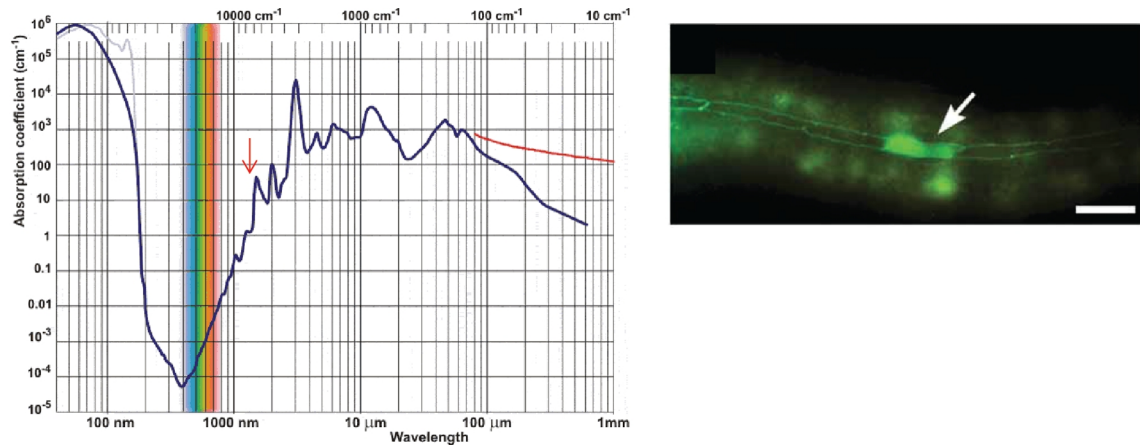


**Figure 1.5 IR-Laser Gene Induction.** Left: Optical absorbance curve for water. 1450 nm represents a peak on the curve (arrow). Right: Image taken from Kamei et al, 2009. A seam cell at the L4 stage is induced by the laser (cell membranes marked by AJM-1-GFP), and heat-shock cytoplasmic GFP expression is visible in the targeted cell. Scale bar is 10  $\mu\text{m}$ .

Kamei et al. advanced the technique by using a wavelength of light specifically tuned for water absorption at  $\sim 1450$  nm (matched to the vibrational symmetric and asymmetric stretching modes of water), thus heating water with  $10^5$  higher efficiency than 440-nm lasers and other visible wavelength lasers. The strategy used for single-cell labeling in this thesis work is based on this paper<sup>76</sup>. The optical absorbance curve of water is shown in Figure 1.5; 440-nm light performs the poorest of all wavelengths in the fraction of energy that is absorbed by water. Given that the minimum spot size that can be achieved by a laser is directly proportional to wavelength, it is important to note that the size of

heating expected with a 1440-nm laser is ~3.3 times larger than that expected with a 440-nm laser.

In contrast to the 440-nm laser response curves, this study shows that the response curves for the IR laser have clear power thresholds for heat shock activation, such that there is a power separation between conditions causing healthy induction and those causing damage. This suggests that laser power correlates to temperature reached at the sample. With the optimal conditions presented in the paper (11 mW, 1 second), IR heat shock induction occurs specifically in the seam cells at the L4 stage at a rate of 40% (nonspecifically additionally in 40% of cells), with damage to the target cell in 0% of cases. Unlike previous studies in which cell damage is not explicitly scored, Kamei et al. score cell damage in the seam cells by looking for loss of expression or aberrant morphology of an apical junction marker (AJM-1::GFP; Figure 1.5). Of note, this study used only these gross morphological defects to score the damage index. A couple of experiments, including gene rescues, in cells fated to divide are shown (seam cells at the L2 stage, and male ray precursors V5 and V6), though induction response curves for these cell types are not given.

Since the Kamei et al. study was published in 2009, several subsequent proof-of-principle studies have applied IR labeling to other model systems<sup>75,77,90–92</sup>. Importantly, all of these papers have demonstrated only cell labeling, usually at single time points, and do not study any aspect of nervous system development. Moreover, no paper has been used to gather new biological data.

#### 1.6.2.3.4 Calibration of Heating Parameters in Kamei, et al.

Unlike previous papers where there is no attempt to measure the temperature generated by the laser, Kamei et al use an “*in vitro*” measurement of temperature, using GFP-expressing bacteria as a thermometer (I recapitulate this system in Chapter 2).

Measurements in this paper suggest that the temperature dependence of heating is  $1^{\circ}\text{C}/\text{mW}$  of IR laser power applied, leading to the temperature at the focus reaching  $(11 \text{ mw} * 1^{\circ}\text{C}/\text{mW}) + 25^{\circ}\text{C} = 36^{\circ}\text{C}$ , close to the established temperature heat shock threshold. The authors also measure the time course of heating; after the laser is turned on, the cell reaches the maximum temperature within  $\sim 100$  ms, with recovery to the baseline temperature also achieved within the same time frame. Thus, their calibration experiments suggest that during optimized heating conditions (11 mW, 1 second), the temperature of the cell is  $36^{\circ}\text{C}$  for 1 second.

A few lines of reasoning suggest that the temperature reached may actually be much higher than what is described. First, the authors use a 0.8 NA objective for temperature measurement experiments, while using a 1.3 NA objective for induction experiments. Higher N.A. objectives, due to their higher focusing abilities, should further spatially concentrate the laser power, leading to higher temperatures; thus, using a lower N.A. objective for temperature measurements will not provide an accurate measurement for the 1.3 N.A. objective. Secondly, though the response curves show a clear power separation between power levels required for healthy induction and cell damage, this separation in power levels is narrow, corresponding to only a  $2^{\circ}\text{C}$  increase in temperature by their measurements; this seems unlikely to elicit such a large change in cellular response.

These reservations about the measurements performed in Kamei et al. are a major focus of our own temperature calibration studies, detailed in Chapter 2.

#### **1.6.2.3.5 Spatial Resolution using Continuous vs. Pulsed Heating**

Most calibration experiments in Kamei et al. were focused on induction of the seam cells in the L4 larval stage. These cells are relatively large ( $\sim 5 \times 15 \mu\text{m}$  in length) compared to neurons or embryonic cells, which are  $\sim 2\text{-}3 \mu\text{m}$  in radius. Even in seam cells, at optimal induction conditions, cells were labeled specifically only 40% of the time, with induction in neighboring cells as well another 40% of the time. This result suggests that during the induction, heat accumulates to temperatures above the heat shock threshold in areas  $> 10 \mu\text{m}$  from the focus.

As embryonic neurons are much smaller ( $\sim 1 \mu\text{m}$  in radius post-mitotically), decreasing the volume of heating is necessary for application to the embryo. Two recent studies, concurrent with our own work, have explored the use of pulsed IR induction parameters to reduce the spatial distribution of heating and thereby increase induction specificity<sup>91,92</sup>. As I show in Chapter 2, theory suggests that pulsed illumination should reduce the size of the heated volume, by allowing heat to dissipate between the pulses. Suzuki et al. explored the use of a pulsed IR laser to target individual neurons deep in ganglia and very early embryonic precursors ( $< 16$  cell-stage)<sup>92</sup>, and a second study used slightly different pulsing conditions to elicit the heat shock response in individual amphid neurons, seam cells at high frequency, and 4-cell stage embryos<sup>91</sup>.

Notably, neither of these studies develop rigorous methods for identifying or quantifying cell damage. Importantly, Churgin et al. also perform experiments to measure



temperature using the “*in vitro*” system and show that their optimal pulsing conditions raise the temperature of the cell to 45-50°C during heating, far exceeding the heat shock temperature threshold. The conditions described in this paper are difficult to compare to previous studies or reproduce, as power levels are given prior to transmission through the objective, which is highly variable.

### **Summary and Considerations in Applying IR Heating to Single Cells of the Embryo**

Laser-mediated heat shock for single-cell expression has a number of advantages over other genetic and optical methods. The system does not require cell-specific drivers and can be used to drive expression of any gene of interest. Secondly, unlike genetic strategies, IR-mediated induction does not rely on “stochasticity”; rather, labeling can be directed to specific single-cells across embryos, a major advantage in a system in which the lineage is invariant. However, a major drawback of heat-shock mediated gene expression is that the heat shock response has wide-ranging effects on cell machinery, and at high temperatures, can cause extensive damage.

Though previous studies have shown that laser-induction can induce single cells in *C. elegans* larvae, several additional considerations are important for application to the embryo. First, embryonic cells are small (~1  $\mu\text{m}$  in radius post-mitotically), thus requiring higher spatial confinement of heat. Secondly, embryonic cells are likely to be much more sensitive to perturbations, as many complex developmental steps (cell divisions, migrations, growth of neurites) are required for cells to generate fully formed neurons from blast cells. Thirdly, the kinetics of the labeling process, which has not been characterized in detail by any previous study, is crucially important for the study of the embryo, as it must be matched to the rapid course of development in *C. elegans*.

## Chapter 2: Design and Calibration of IR Laser Optical Setup

### 2.1 Characterizing the Heat Shock Response in *C. elegans* Embryos

I first aimed to identify the exact heating parameters required to induce the heat shock response in the embryo using whole-embryo heating. I also quantified the kinetics of the labeling process using different fluorescent reporter strains. As phototoxicity is an issue with long-term imaging of embryos, I aimed to identify reporters with maximal brightness such that excitation exposure could be reduced.

#### 2.1.1 Strain Construction

I developed three fluorescent reporter strains for visualizing heat shock expression; two strains drive myristoyl-GFP or myristoyl-mCherry directly using the heat shock promoter, *hsp-16.2*. The third strain generates a signal constitutively; a heat shock-driven Cre recombinase construct excises a floxed STOP cassette in a *his-72*<sub>pro</sub>::lox-STOP-lox::myr-GFP construct to generate constitutive expression in all embryonic cells. (This *his-72* promoter has been previously characterized to be approximately equally expressed in all cells of the embryo, and is used for lineage tracing <sup>31</sup>.) The myristoyl moiety is used to direct fluorescent proteins to the cell membrane, enhancing signal in thin, cytoplasmic-poor neurites.

#### 2.1.2 Temperature Requirements for Heat Shock in Embryos

As the exact parameters for inducing the heat shock response in *C. elegans* varies widely in the literature <sup>93-95</sup>, I first characterized the temperature requirements for the heat shock response in pre-morphogenesis embryos (150-250 min post fertilization). Because inducing single cells with a laser is not feasible for very long periods of time (due to cell

divisions, cell migrations, etc), I measured the response for 5 minutes of heating (a duration feasible to achieve with laser heating) at various temperatures in a water bath, and scored the resulting induction using a heat-shock driven myr-GFP reporter. In order to determine whether cells are healthy after heat shock induction, embryo hatching was used as a proxy for overall cell viability.

As shown in Figure 2.1A, embryos heated to 32°C produce a robust heat shock response and also maintain a high hatching rate. Temperatures higher than 36°C lead to a substantial decrease in embryonic viability, suggesting that this temperature should not be exceeded. All strains had similar temperature requirements (data not shown).

### **2.1.3 Kinetics of Heat Shock Reporter Expression:**

The kinetics of fluorescent reporter expression is an important parameter for developmental studies, as the delay between induction and signal accumulation must be matched to the course of development. An advantage of heat shock-based gene expression over other labeling strategies, such as photoconversion, is that induction creates a persistent transcriptional response, with mRNA accumulating over the course of 1-2 hours, as measured in *C. elegans* worms<sup>96,97</sup>.

To test the kinetics of fluorescent reporters after heat shock induction, I quantified the expression levels of the three reporter strains after a water bath induction. I found that a five-minute heat shock in a water bath at 33°C produced a visible signal in all constructs after ~1-2 hours and strikingly, this signal persisted without any signs of bleaching for 5-6 hours, covering the entirety of morphogenesis and elongation (Figure 2.1B; see the developmental time course below x-axis). For myr-GFP, the signal appears within 45 min,

whereas for myr-mCherry, the signal appears at ~80 min, likely due to the additional fluorescent protein maturation time. For heat-shock driven Cre-lox recombination, the lag

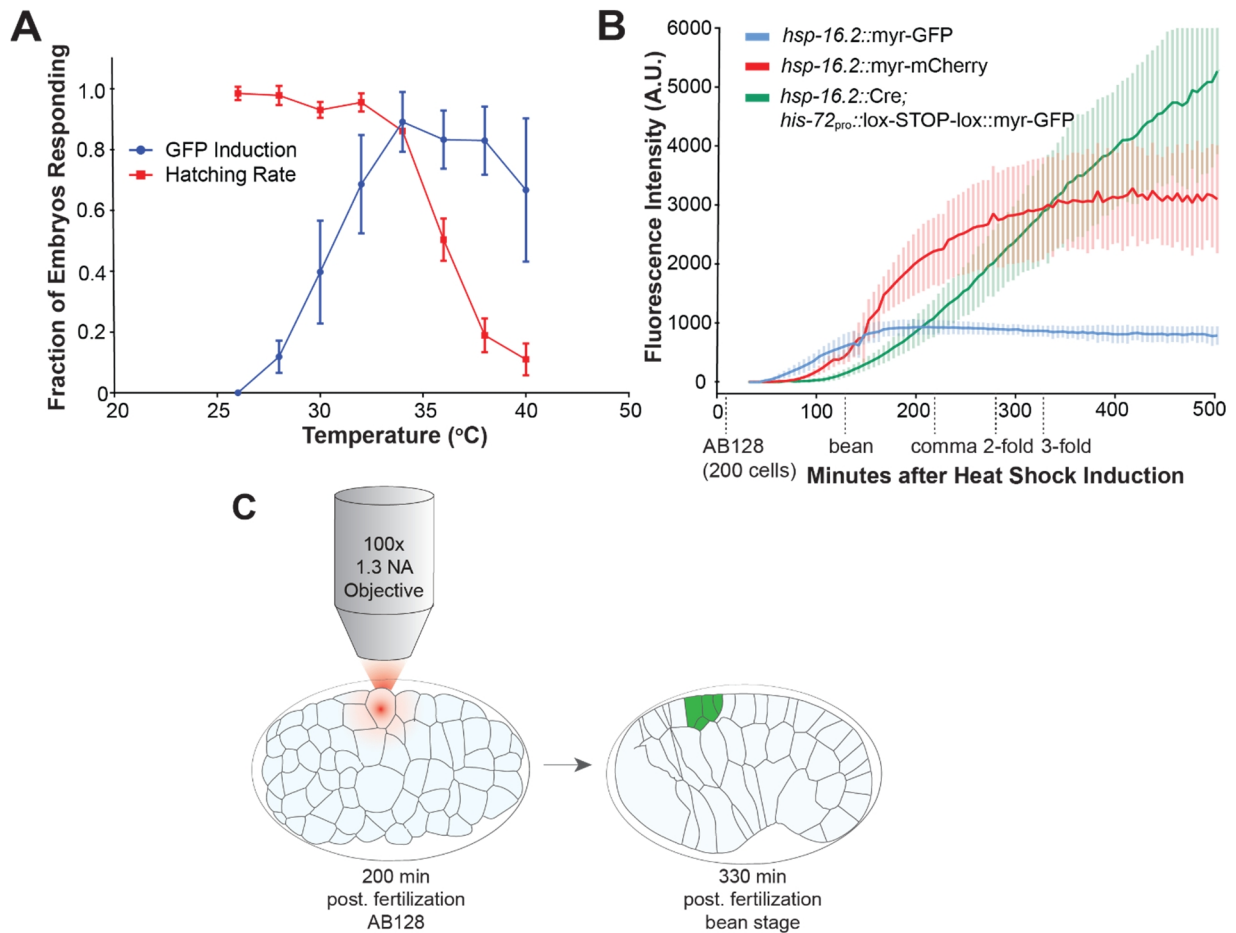


**Figure 2.1 Characterizing the Heat Shock Response in Embryos.** (A) Reporter induction rates and viability after induction. Induction was scored when >50% of cells showed myr-GFP expression. N>30 for each condition, average of 2 trials. (B) Fluorescent-protein induction kinetics. Average fluorescence intensity after heat induction is plotted vs. time (n = 4-6 embryos/reporter) (C) IR-Laser Induction Schematic. Progeny of cells induced at AB128 are visualized by heat-shock-dependent reporters 2 hours after induction.

time is the longest (~110 minutes). Interestingly, after normalizing for laser power, the peak of myr-mCherry signal reached ~2.5 fold higher levels than for myr-GFP; combined with the lower phototoxicity due to longer wavelength imaging<sup>98</sup>, the myr-mCherry protein produced ~12x stronger signal compared with myr-GFP. Thus, for our long-term imaging experiments, the myr-mCherry reporter was used.

We were interested in visualizing developmental events occurring at the beginning of morphogenesis, at approximately 330 minutes post fertilization (m.p.f.) in the *C. elegans* embryo. We considered the tradeoffs of inducing cells at various points in development. Inducing cells early in development produces a strong signal at the time of morphogenesis, but also generates a signal in a larger number of descendants which may not be optically resolvable; inducing a cell after the terminal round of division is complete would generate signal in a single cell, but most early morphogenetic events could be missed. Given that the myr-mCherry signal takes ~100 minutes to accumulate, we addressed this tradeoff by optimizing single-cell induction at the AB128 cell stage, after which most cells generate 4 progeny (Figure 2.1C).

## **2.2 Theoretical Simulations of Laser Heating**

A recent study demonstrating IR-induced labeling in single larval cells has shown through temperature measurements of the IR-laser generated heat distribution that the radius of heating above the biological threshold is 5-10  $\mu\text{m}$ <sup>76</sup>. As embryonic cells are smaller than larval cells (radius of ~2  $\mu\text{m}$  at the AB128 stage), I anticipated that further optimization of the heating parameters would be needed to achieve single-cell induction.

I first aimed to understand the distribution of heat generated by the laser using theoretical simulations. These simulations demonstrate that five parameters affect the distribution: (1) the amplitude of the laser power, (2) the size of the laser focus (determined by the laser wavelength used), (3) the background temperature of the sample, (4) the length of the induction (either a continuous duration or short, separated pulses), and (5) the frequency of pulses. As the parameter space with these five variables is very large and thus difficult to test empirically, the goal of the simulations was to identify regions of the parameter space that would be tested further with the optical setup, and to purchase components that would allow us to access those parameters (e.g. for pulsing the laser at high frequency).

The simulations described are based on equations from models of heat generation from femtosecond laser ablation from Vogel et al., though all the parameters were altered to match our setup<sup>99</sup>. Importantly, a couple of errors exist in the written text of the equations, which I corrected, although the simulations from the original work appear to be performed with the correct versions of the equations and are still valid (Figure 2.2B,E, errors shown in red). (For example, the loss of the  $3/2$  exponent in the original equation prevents the system from ever reaching steady-state).

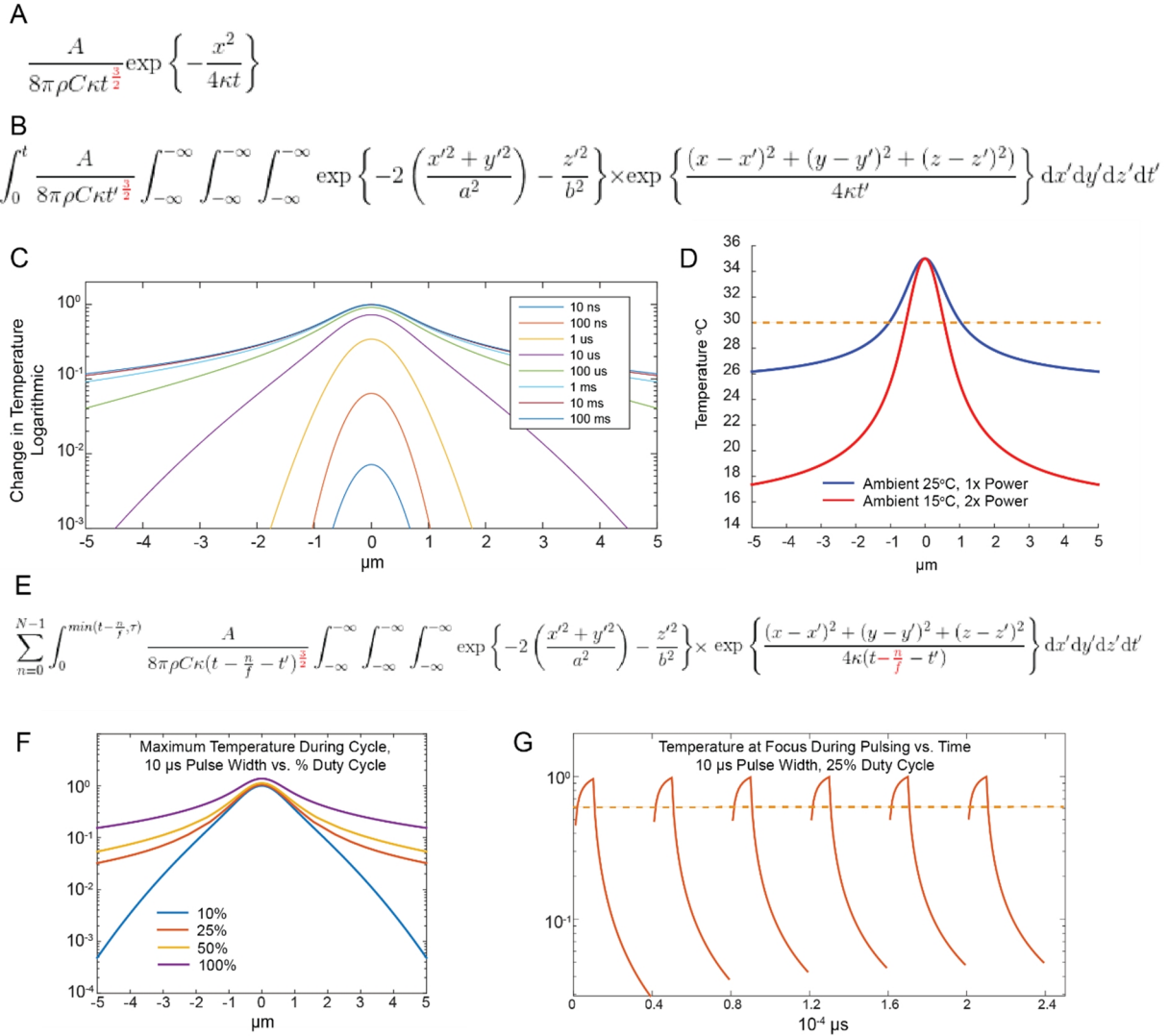


**Figure 2.2 Simulations of Laser Heating.** (A) Fundamental Solution to the Heat Equation (B) Continuous Wave (CW) Heating (errors<sup>99</sup> marked in red) (C) Evolution of Distribution with CW Heating (D) Spatial Distribution of Heating at Steady State (E) Pulsed Heating Equation (F) Effect of Duty Cycle on Spatial Distribution (G) Temperature at Focus During Pulsing

**Table 1**

Pulse Length	Fold-Power Increase vs. CW	Maximum Duty Cycle (%)	1/e <sup>2</sup> Radius of Heating (x-y), at any time point (μm)
100 ns	15.5x	2%	0.8
1 μs	2.9	6%	1.02
10 μs	1.4	24%	1.7
100 μs	1.1	62%	2.86
1 ms	1.02	96%	3.84

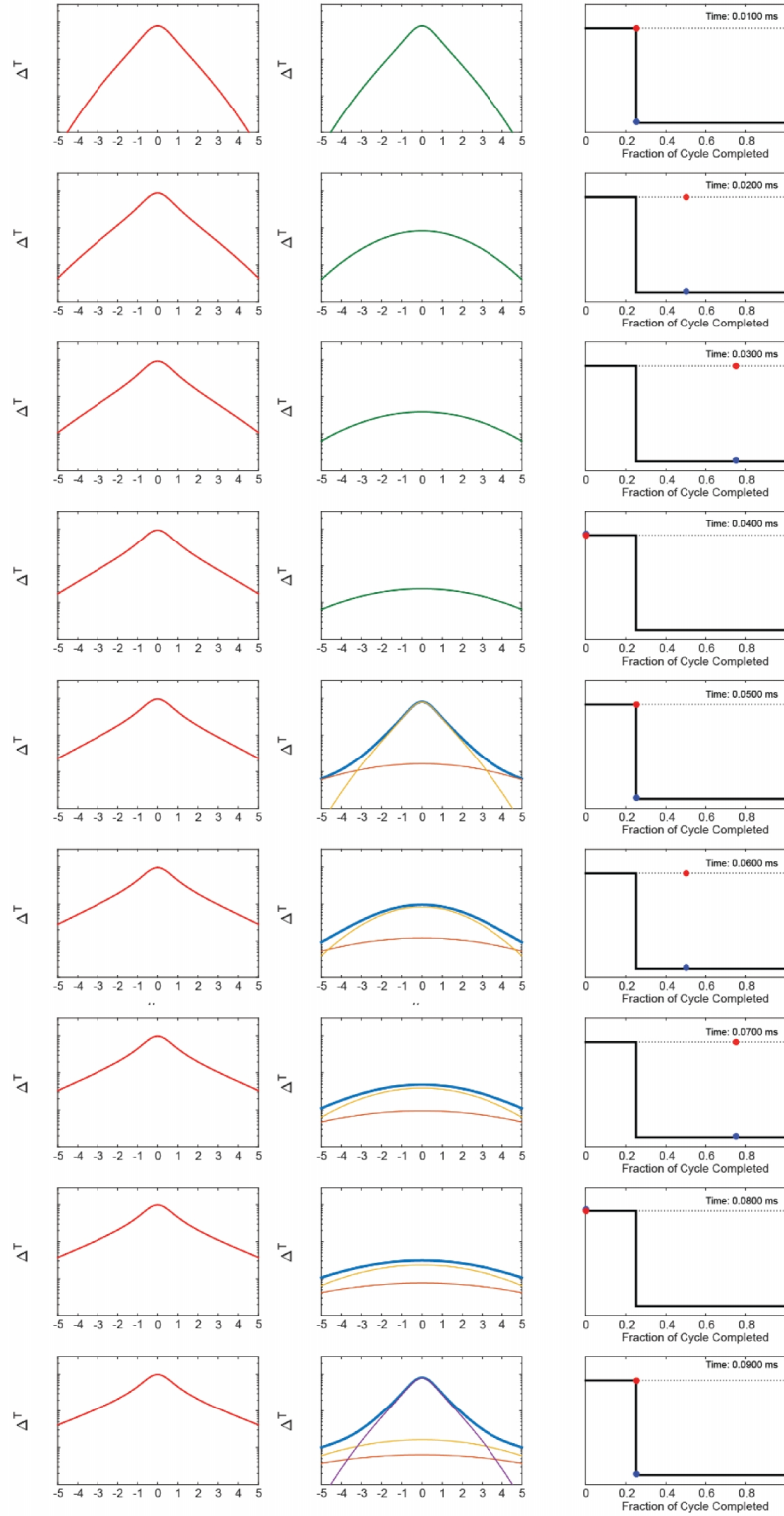


**Figure 2.3 Evolution of Heating with Pulsing.** Continuous Wave (left). Pulsing with 10  $\mu$ s Pulse Length and 25% Duty Cycle (middle). Point in Cycle (right). During pulses, contribution from each pulse is shown, and the darker line indicates the summed value.



### 2.2.1 Equations Modeling Continuous Heating

The solution to the differential equation describing the diffusion of a point source of heat in an infinite space is given in Figure 2.2A, where  $A$  is the amplitude of the power,  $k$  is the diffusivity of the media,  $C$  = heat capacity,  $\rho$  = density, and  $n$  is the number of dimensions of the space (in a volume,  $n = 3$ ). This equation describes the diffusion of heat for an instantaneous point source in an infinite space.

In order to model continuous heating for a finite source, the fundamental solution given above can be superimposed in both space and time. Assuming that the focus of the laser reaches a diffraction-limited spot, the size of the beam is given by the central diameter of the Airy pattern, where the length of the axis in the x-y plane is  $d = 1.22 \cdot (\text{wavelength}) / \text{N.A.}$ , and the length of the axis in the z-plane is longer, approximately  $2.4 \times$  (dependent on the numerical aperture)<sup>99</sup>. Therefore, for a laser of wavelength 1455 nm and an oil objective with N.A. = 1.3, the radius of the spot in the x-y plane is 0.68  $\mu\text{m}$ , and the diameter in the x-y plane is 1.64  $\mu\text{m}$ . To superimpose solutions of the point source in space, I integrated the equation over the 3 dimensions of the source, assuming for simplicity that the amplitude follows a Gaussian distribution. Then, I integrated this equation in time, since the laser heating occurs over a defined duration.

The starting equation for integration is shown in Figure 2.2B, where the first term represents the amplitude of the source, and the second term represents the diffusion of heat for each point by the equation shown above. Due to the Gaussian shape of the starting distribution, the integral over  $x'$ ,  $y'$ , and  $z'$  can actually be computed analytically, and this solution was generated with Mathematica. The time integral was computed numerically using MATLAB.

Since the amount of energy from the heat source contained by some point is linearly related to the temperature elevation at that point, the output of the equation is given as temperature elevation. Rather than compute the actual values for the temperature elevation, which is highly dependent on absorption, the values are plotted in a relative fashion, such that the maximal temperature at the focus is 1 and all other points are given as relative values. The y-values are plotted on a logarithmic scale to allow differences between graphs to be easily observed.

### **2.2.2 Theoretical Temperature Distribution Generated by Continuous Heating**

In Figure 2.2C, the time evolution of the temperature distribution in the x-y plane is shown at the time when the laser has been on for a given amount of time. As can be seen, during continuous heating, heat from the source accumulates at the focus. While the laser is on, heat will also dissipate around the focus, in accordance with the rate of the diffusion. If the time of heating is very short, there will not be sufficient time for the heat to dissipate within that time frame, and the heat will be maintained at the focus. At longer time scales, the whole system will reach a steady state, with the heat entering any area from the source equal to the amount of heat diffusing away from that same area.

For time periods greater than 100  $\mu\text{s}$ , the distribution starts to approach the steady-state with only small temperature increases near the focus as time passes. Thus, previously published studies using continuous heating in the 1 second range are likely to be in the steady-state regime<sup>76</sup>.

Next, I used the steady state distribution of heating to consider how the volume heated by the laser is affected by the ambient temperature. Note that, according to the equation, the amplitude of the temperature elevation at the focus and at any point away from the focus is simply linearly dependent on the amount of laser power applied. The blue curve shown in Figure 2.2D represents the distribution of heat with a given power amplitude that elevates the focus from an ambient temperature of 25°C to a temperature of 35°C, an elevation of 10°C. If the background temperature is dropped to 15°C, 2x as much power must be applied to elevate the focus by 20°C and thus achieve the equivalent temperature (Figure 2.2D, red curve). Although the distributions are linearly scaled with respect to each other, the volume of heating above a certain threshold (e.g. 30°C, Figure 2.2D, shown in orange) is narrower when the ambient temperature is lower. Therefore, reducing the ambient temperature (e.g. by cooling the specimen with a temperature-controlled stage) while compensating for a cooler sample by increasing laser power, together can create a narrower heated volume.

### **2.2.3 Equations Modeling Pulsed Heating**

Recent studies improving on the IR-induction technique have used laser pulsing to reduce off-target heating, and prior studies using a 440-nm laser for heat shock and ablation have also used pulsed-dye lasers<sup>78,89</sup>. Next, I aimed to use my simulation to study how pulsing the laser would change the size of the heated volume. Pulsing the laser reduces the volume of heating because, as shown in Figure 2.2C, heat only accumulates at the focus during short periods ( $< 1 \mu\text{s}$ ). Turning the laser off after a short pulse allows the heat to completely dissipate. This is demonstrated below with data from my simulation.

The equation shown can be modified to show the heat distribution for pulses, by changing the time periods over which the equation is integrated (Figure 2.2E). In the equation shown,  $N$  represents the number of pulses, with each pulse representing a value  $n$ , which takes values 1 to  $N$ . The frequency of pulsing is given by  $f$  and the pulse length is given by  $p$ . For each pulse, the time period of integration is changed from 0 to length of that pulse ( $p$  for the pulses that have been completed, and  $t-n/f$  if the laser is on at time  $t$ , meaning the current pulse is being evaluated). The time that has passed from a time point within a specific pulse ( $t-n/f-t'$ ) is used to determine the dissipation of heat. The distribution generated from each pulse is summed to determine the final distribution.

#### **2.2.4 Theoretical Temperature Distribution Generated by Pulsed Heating**

A time sequence of pulsing the laser versus continuous wave induction is shown for comparison (Figure 2.3). First, note that the time between one pulse and the next pulse must be sufficiently long such that the heat dissipates completely. If the time between consecutive pulses is very short, the pulses will sum together, leading to a distribution similar to the continuous wave distribution (Figure 2.2F). Second, note that during pulsing, the cell is only heated to the maximum temperature for a fraction of each cycle; most of the time is spent in allowing the heat to dissipate (Figure 2.2G). Thus, pulsing the laser requires that the cell “integrate” the signals above the heat shock threshold to induce a response. Finally, note that, as shown in Figure 2.2C, the amount of energy accumulating at the focus during short pulses is lower than that seen during longer heating periods; since increasing power applied will linearly increase the temperature while maintaining the shape of the heat distribution, increased power levels are required

to reach the same maximum temperature as in the continuous wave steady-state distribution.

A summary of the spatial distributions, power requirements, and required dissipation times are given in Table 1. Pulse widths of 100 ns are required to maintain heating solely around the focus, though improvements are seen up to 1 ms. The % of the cycle that must be spent to achieve full dissipation is longest for short pulses, to accommodate the fact that the time it takes for the heat to diffuse is mostly a function of the diffusion constant, and therefore does not change substantially based on pulse length (although longer pulses will have wider distributions that take longer to diffuse). As per the discussion above, although short pulse lengths  $<1\ \mu\text{s}$  offer the greatest spatial resolution, they also require much more power (15x), and the greatest amount of time must be spent in dissipation to prevent pulse summation. The need for increased spatial resolution and issues with eliciting a heat shock response with infrequent signals must be balanced in the pulsing regime.

### **2.2.5 Summary of Simulation Results**

From simulations of heat generated by the laser, we find two ways to reduce the size of the heated spot. With continuous wave heating, the size of the heated volume can be reduced by lowering the ambient temperature and increasing the laser power to create a steeper distribution. This method is simple, but there is a limitation to how much the sample can be cooled without affecting embryonic viability and without causing condensation of water on the objective lens (empirically must be  $>10^{\circ}\text{C}$ ). With pulsed wave heating, a tighter distribution can be achieved by sequentially administering short pulses ( $<1\ \mu\text{s}$  optimally). However, as heat shock is usually the result of a continuous

stressor, whether the heat shock response can function to sum these separate short signals over time is not known. Moreover, long dissipation times required between pulses may allow for cell recovery. Even if the cell is capable of integrating these responses and is heated for only ~10% of a cycle, it would have to be induced 10x longer to achieve the same duration of heating as compared with continuous induction. This is a significant technical consideration.

## **2.3 Design and Construction of IR Laser Microscope Setup**

I designed a simple optical setup to heat single cells, which is integrated with a commercial upright wide-field microscope. The optical path allows for IR induction and fluorescence imaging. The compatibility with fluorescence imaging is required to identify fluorescence-labeled cell nuclei for induction and to use fluorescence measurement as a readout for IR-induced temperature changes (both applications are described later in this chapter).

### **2.3.1 Optical Parts**

The basic configuration is shown in Figure 2.4 and 2.5. The infrared laser is a 1455-nm single-mode continuous-wave 2W laser. A single-mode laser (as opposed to a laser diode) is required to achieve a diffraction-limited spot size. The laser light is collimated, expanded using a 2-lens telescope (4x using a 50 mm and 200 mm lens), and then directed using a set of mirrors to the side port of the microscope. This side port allows access to infinity space before the imaging dichroic. Here, I placed another shortpass dichroic to merge the fluorescent-reporter excitation beam (depicted in blue) and the IR

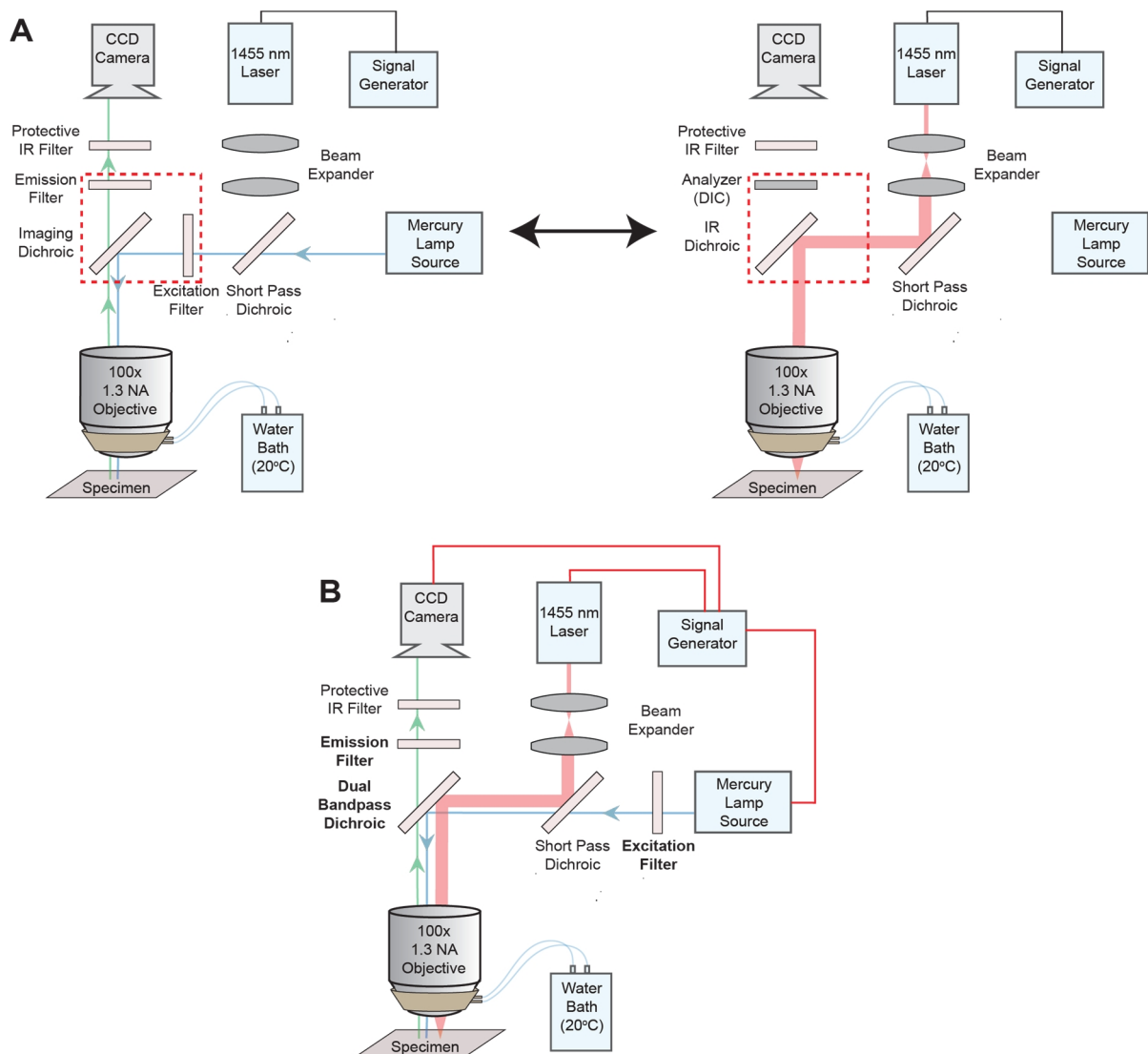


**Figure 2.4 Schematic of Optical Setup** (A) Configuration used for Cell Induction and Fluorescence Scoring. Separate dichroics are used for fluorescence imaging (left) and IR excitation (right) to maximize fluorescence signal. (B) Configuration for Simultaneous IR Induction and Fluorescence Measurements. The excitation filter is moved behind the shortpass dichroic to prevent IR blockage. The signal generator drives the laser, camera, and excitation source.

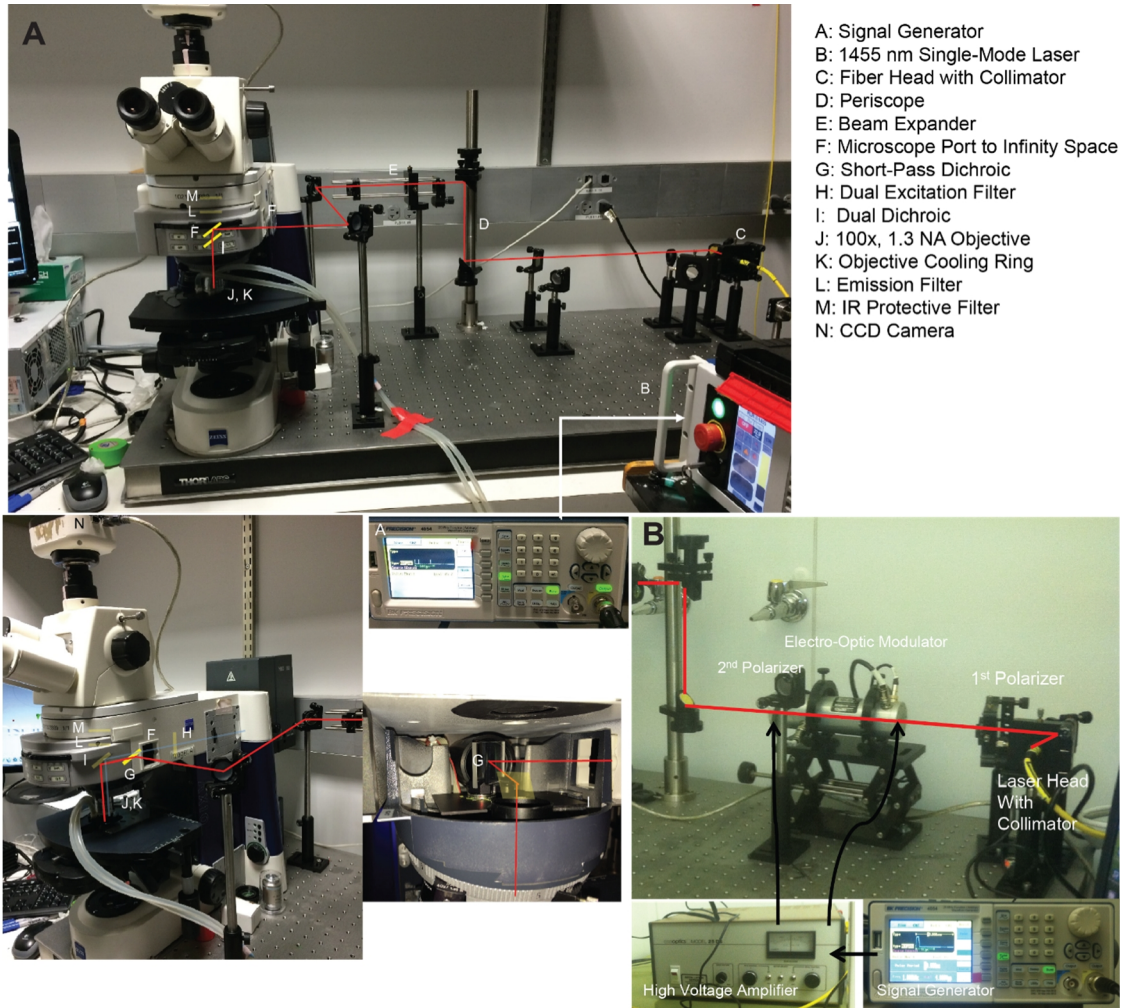


**Figure 2.5. Optical Design and Construction.** (A) The power and duration of the infrared laser pulse is controlled by a signal generator (A) connected to the laser external interface (B). After collimation (C), the beam is expanded by two lenses (E) and then directed to the side port of the microscope (F, Zeiss AxioImager A1), accessing the infinity space before the imaging dichroic. Here, we placed a shortpass dichroic in a fabricated mount to merge the excitation beam (blue) and the IR beam (red). The dual dichroic (I) and emission filter (L) for imaging mCherry/GFP and reflecting IR are placed in the filter turret. An additional IR filter (M) is placed before the camera and eyepieces to block any residual IR radiation. A temperable ring (K) is affixed to the objective (J) and connected by tubing to a temperature-controlled water bath (not shown) to cool the sample. (B) Apparatus used for pulsing the laser at high frequency ( $<50 \mu\text{s}$ )



beam (depicted in red). A dichroic which reflects IR is placed in the filter turret. An additional IR filter is placed between the camera and eyepieces to block any residual IR radiation.

### **2.3.2 Design Considerations for the Setup**

The back aperture of the objective must be overfilled in order to achieve the smallest possible spot size. However, there is a tradeoff between overexpanding the beam such that the narrowest possible distribution is created (an airy disc with a narrow central maximum for a completely flat-topped laser) because most of the power will be lost through truncation. Overexpanding the beam such that the size is  $\sim 1.5$  times the size of the aperture optimizes this tradeoff. For our Zeiss 100x 1.3 N.A. lens, the back aperture is approximately 4.3 mm wide. After 4x beam expansion, the laser is (1.6mm x 4 =) 6.4 mm wide, achieving this ratio.

Traditional laser ablation setups merge the epifluorescence beam and the laser beam from behind the microscope through the epifluorescence port. We found that this method was not suitable for introducing the IR beam because several lenses, which serve as an epifluorescence condenser, poorly transmit IR and therefore block most of the laser power. To bypass these lenses, we used a port on the side of the microscope, which fortunately placed the beam right before the imaging dichroic. As there were no parts in place for merging the fluorescence and IR beams in this location, we designed a small reversible piece (made removable by affixing a circular magnet to the base of the dichroic mount and another magnet to the microscope itself) which holds a shortpass dichroic to sit stably in this space.

### **2.3.3 Systems for Pulsing the Laser**

In the current version of the setup, a signal generator directly drives the laser through the external pin interface. The rise time and fall time for the laser power is approximately 50  $\mu$ s, indicating that pulses of width  $< 100 \mu$ s are not possible with this system. Through empirical optimizations (described in Chapters 3 and 6), we found that pulses shorter than this length are not required for IR-mediated cell labeling and ablation applications.

An older version of the setup contained a system to pulse the laser at higher frequency (Figure 2.5), since our simulations and other papers have suggested that optimal spot size is achieved with pulse widths  $< 100$  ns. Pulse lengths of this duration cannot be achieved through driving the laser directly, so an electro-optical modulator (EOM) was used. The EOM contains an electrically birefringent crystal, which changes the direction of the wave polarization based on the amount of power applied to the crystal. By sending the wave through polarizers oriented opposite to each other by  $90^\circ$ , the amplitude of the wave is proportional to the electrical power, generated by a high voltage (HV) amplifier, driving the EOM. This system has a 10 ns rise time and 10 ns fall time and can generate pulses of  $> 40$  ns width. After optimization of the parameters (Chapter 3), this system was not used further.

### **2.3.4 Imaging and IR Induction Configurations of the Microscope**

The microscope was used in two configurations, shown in Figure 2.4. The first configuration is used for IR cell-induction experiments, which additionally requires GFP imaging to see nuclear reporters for identifying cells (Chapter 3.1) and mCherry imaging for scoring heat shock-driven fluorescence. In this configuration, visualization of cells by

fluorescence and IR induction can be performed sequentially. Therefore, separate dichroics to perform these tasks are placed in the filter turret. One dichroic is used only for IR induction, which also contains a polarizer for DIC imaging. For imaging cells before and after induction, separate GFP and mCherry filter sets are used. The excitation filter (Figure 2.4), due to its narrow bandwidth, would block the infrared, so these functionalities are separated.

The second configuration allows for simultaneous IR induction and fluorescence imaging. This configuration is required for the temperature measurements performed later in this chapter. Here a dual dichroic for mCherry and GFP, which also reflects IR, is placed in the filter turret, and a dual excitation filter is placed behind the shortpass dichroic to prevent IR blockage. The emission filters are either single for the required wavelength, or the emission can be split to image in two colors simultaneously onto the imaging camera. This configuration is more efficient, in that the dichroic does not need to be switched, but our dual filter set has poorer transmission and excitation of GFP and mCherry, and so was not used in daily experiments when the brightness of the reporters is limiting.

### **2.3.5 Alignment of the Microscope**

The beam was aligned into the sample plane by a number of techniques. Fortunately, our CCD camera does have a slight sensitivity in the IR, such that  $<1$  mW of power bouncing off a coverslip and onto the camera can be seen. The IR reflection can be seen when passing between two mediums of different refractive indices. In our samples, two such points are the bottom-of-coverslip to water interface, and the water-slide interface. The

beam can be aligned exactly vertically in Z by having the laser reflect at the same X,Y point in both of these planes.

Z-alignment of the beam, such that the focus of the beam matches the imaging plane of the objective, was more difficult. We found that aligning the “sharpest” point of IR reflection to the interface actually caused heating of the cells several microns below the imaging plane. This inconsistency may reflect chromatic aberrations of some imaging lens. Therefore, I used optical trapping of 3-um polystyrene beads to align the beam to the imaging plane. I further confirmed that this was the correct focal plane through heating experiments. After the fact, I noted that collimating the beam to minimize divergence after the beam expander (such that the image of the beam is at infinity) brings the laser to the appropriate focus (no corrections need to be made for chromatic aberrations of the objective).

### **2.3.6 Operation of the Microscope**

The focus of the laser is verified at the start of each experiment by visualizing it on the camera, and x-y minor adjustments are made using the two mirrors that divert the laser into the microscope that control both angle and position of the beam. The slight daily shifts ( $\sim 1\text{ }\mu\text{m}$ ) are likely to be due to the instability of the shortpass dichroic which is not in a proper mount. The z-focus is only dependent on the distance between the lenses in the beam expander, and therefore does not need daily re-calibration. A crosshair in the eyepiece marks the center of the field of view, and this same location is marked by a piece of tape on the monitor showing the camera output.

After a cell is brought to the center of the field of view using the crosshair in the eyepiece, the laser is turned on using the front panel, or remotely using the signal generator. During long inductions (>2 min) the cell can migrate slightly due to development or Brownian motion, so an effort is made to keep the cell centered by observing the cells either through the eyepiece (with an IR filter) or through the live view of the camera and adjusting the location of the stage manually. Usually adjustments are made by looking at the camera image so that the user's eyes are not inadvertently affected by IR irradiation.

## **2.4 Direct Temperature Measurements of IR Laser-Induced Heating**

In this section, I describe two systems that I implemented for measuring the temperature distribution generated by the laser directly. Both systems rely on fluorescent proteins as temperature sensors, for which the intensity of fluorescence decreases linearly with temperature change: (1) an “*in vitro*” system, using GFP expressing bacteria embedded in agarose gel, originally described by Kamei et al.<sup>76</sup> (2) an “*in vivo*” system using mCherry as a temperature sensor in *C. elegans* cells.

As described in the section on heat simulations, a number of parameters contribute to the heat distribution generated by the laser, and this large parameter space proved difficult to optimize directly. First, the kinetics of the process mean that embryos can only be scored hours after laser heating. Secondly, as there is some variability in the heat shock response even at single temperatures (Figure 2.1A), a number of embryos need to be induced to evaluate a single condition. Thus, I decided to take a reverse approach and measure the temperature in the system directly, therefore providing a direct and immediate readout. I used these measurement systems to find laser parameters that

would raise the volume of a single cell to the heat shock threshold, and sub-heat shock temperatures in neighboring cells.

#### **2.4.1 Concerns with Measurements in Previous Studies**

As described in the introduction (1.6.2.3.4), Kamei et al. used the “*in vitro*” tissue model to validate their induction parameters, showing that, as predicted by heat simulations, the temperature at the focus and at all points shows a linear relationship with the power applied to the system. The authors report that the temperature elevation is 1°C/mW, suggesting that during optimized induction (11 mW, 1 second) the temperature reached is (25°C ambient + 11 mW x 1°C/mW) 36°C, close to the heat shock response threshold. However, one major feature of this measurement was concerning to us; the authors use a 0.8 N.A. objective for temperature measurement experiments (citing the increased field of view), whereas induction experiments are performed using a 1.3 N.A objective. As the focal spot radius is inversely dependent on N.A., this means that the same amount of laser power is distributed over a ~4.5x smaller volume of heating for the higher N.A. objective. This indicates that the actual temperature reached during induction experiments is likely to be much higher than reported.

A second paper, Churgin et al., has recently followed up on the IR laser induction strategy and also reports temperature measurements with the correct imaging objective<sup>91</sup>. Unfortunately, laser power measurements for this study are never given at the sample (rather before the objective) and so cannot be compared between studies. This paper also suggests using fluorescent proteins expressed in *C. elegans* cells directly as temperature sensors, bypassing the *in vitro* model. However, for the reported data, the temperature sensitivity of GFP expressed in *C. elegans* cells is assumed to be the same as it is in

bacteria, and as I show, the sensitivity appears to be less by 50-66%, calling these results into question.

## **2.4.2 An *in vitro* System for Temperature Measurement**

In this section, I re-created the *in vitro* tissue model<sup>76</sup> and determined the relationship between laser power and temperature elevation at the focus with a 1.3 N.A. objective in this system.

### **2.4.2.1 Description and Calibration of the *in vitro* System**

To generate the sample mount, GFP-expressing bacteria were spread on the surface of an agarose pad and allowed to dry, essentially embedding them into the agarose. Since our microscope is widefield, this procedure limited fluorescence to a single z-plane, preventing any contribution from out-of-focus fluorescence.

The brightness of GFP in bacteria reversibly changes in response to a temperature shift, allowing correlation of brightness with temperature. To measure the temperature generated by the laser, two measurements must be taken – one with the laser OFF to establish the baseline fluorescence, which changes from bacterium to bacterium, and the second with the laser ON to capture the change in fluorescence.

To convert change in brightness to temperature change, the temperature dependence of the fluorescent protein must be calculated. To perform this measurement, we serially changed the temperature of the sample using a water bath connected to the temperable ring of the objective, and then captured images of the field-of-view. Whole-bacterium fluorescence measurements were taken and plotted against ambient temperature (20°C), as shown in Figure 2.5C. Similar to the published curves<sup>76,91</sup>, we

found that GFP in bacteria exhibits a temperature dependence of  $\sim -0.8\%/^{\circ}\text{C}$  (Figure 2.6A). As some of the signal loss between subsequent imaging frames is due to fluorescence bleaching, this decrease must be corrected. The GFP bleaching rate is minimal and is shown in Figure 2.6B.

The microscope was used in Configuration 2 (depicted in Figure 2.4) with a GFP emission filter. To create sequential images of Laser ON and Laser OFF specimens, the signal generator was used to sync the camera exposure, excitation source, and laser ON/OFF period, in particular to prevent bleaching outside of imaging times.

#### **2.4.2.2 Results of *in vitro* Temperature Measurements**

A field of view of bacteria-expressing GFP at baseline (Laser OFF) is shown (Figure 2.6C). Another image of the field of view with 14 mW of IR laser power applied to the center (Laser ON) is taken. Dividing the images, pixel by pixel, shows fluorescence decrease at the focus and to a lesser extent in the surrounding tissue. To measure the relationship between power applied and temperature elevation at the focus, I quantified the fluorescence change of bacteria at the focus for several laser powers and in multiple fields of view.

As shown in Figure 2.6E, the temperature elevation depends on IR laser power at a rate of  $\sim 3^{\circ}\text{C}/\text{mW}$ . This is  $\sim 3\times$  steeper than the reported measurement from Kamei et al.



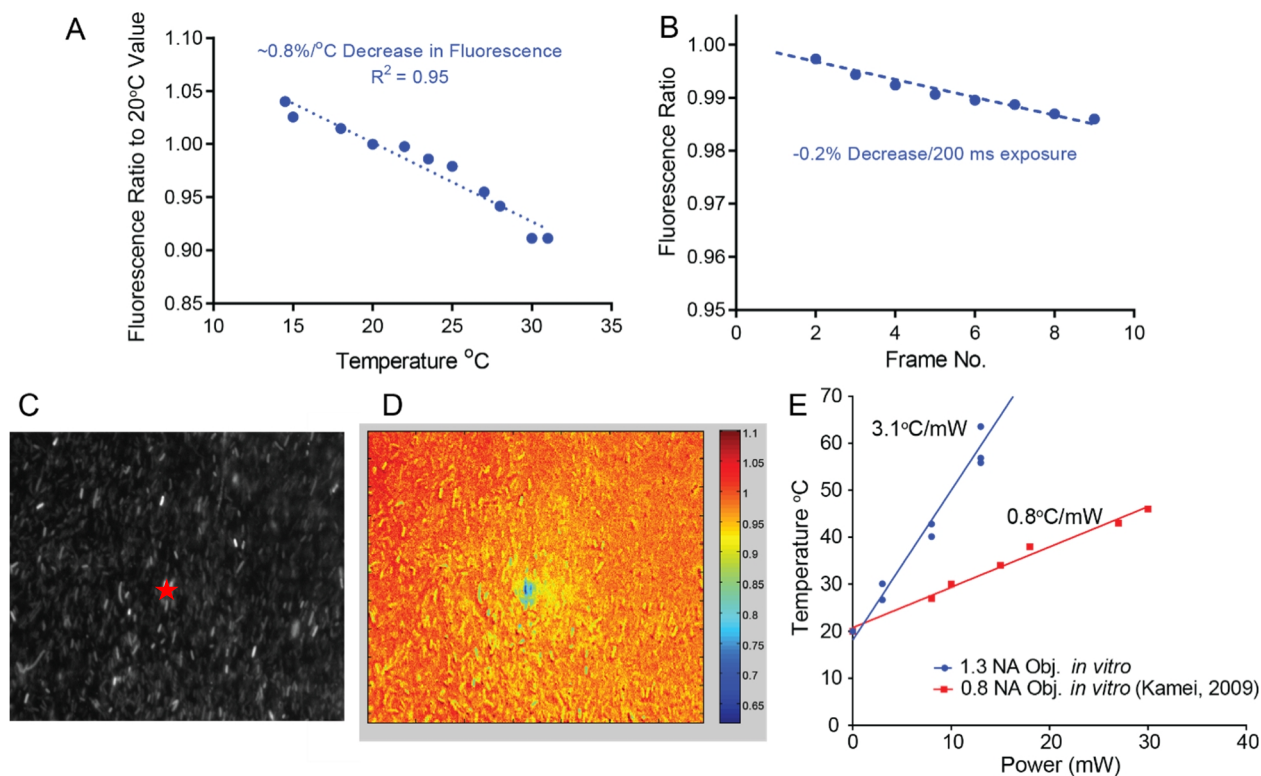


**Figure 2.6 *In vitro* Temperature Calibration and Measurements** (A) GFP Temperature Sensitivity when Measured in *E. coli* (B) GFP Bleaching Rate (C) Image of Bacteria Expressing GFP at Baseline. Star indicates laser focus (D) Laser ON/Laser OFF Image. Ratiometric Map of Fluorescence Decrease at with 14 mW of Laser Power (E) Temperature at the Focus vs. Laser Power. Red curve is taken from Kamei et al. 2009

### 2.4.3 An *in vivo* System for Measuring IR-Induced Temperature Changes

Data from the *in vitro* bacteria system support our claim that the temperatures being reached during previously optimized IR induction conditions were much higher than reported. However, the *in vitro* system may not accurately represent the temperature distribution in *C. elegans* tissues. For example, cell membranes connected to each other may serve as temperature insulators, leading to higher peak temperatures, whereas the water-based agarose medium between bacteria may allow for quicker diffusion.

Similarly, if the cell membrane acts as a strong insulator, the cell may continue to accumulate heat over the course of the laser induction and not reach a steady-state

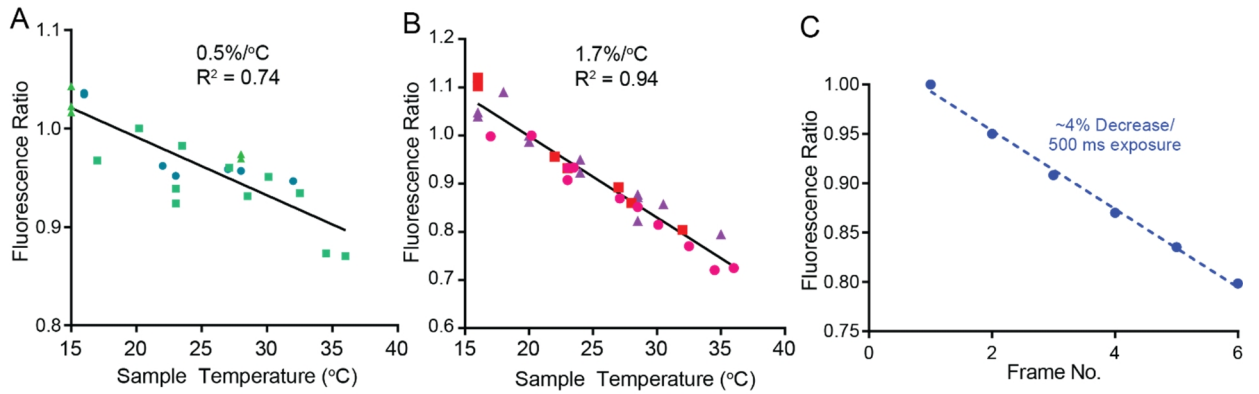


**Figure 2.7 *In vivo* Temperature Calibration** (A) GFP Temperature Sensitivity Measured in *C. elegans* (B) mCherry Temperature Sensitivity Measured in *C. elegans* (C) Bleaching Rate of mCherry

temperature. The kinetics of this process are important for laser induction optimization.

For this study, we created a system to measure temperature *in vivo* and then applied this system to measure the relationship between temperature elevation and laser power at the target cell, the spatial distribution of laser heating, and the kinetics of heating.

#### 2.4.3.1 Description and Calibration of the *in vitro* System

I designed a method to measure the heat distribution in the embryo. As no commonly used methods exist, I first measured the temperature dependence of different fluorescent proteins expressed in *C. elegans* cells. Embryos or anesthetized larvae expressing GFP or mCherry under the *ceh-27* promoter (explained below) were mounted, and the temperature of the sample was varied by using a water bath/objective cooling ring apparatus. The fluorescence of cells in the resulting images at various temperatures was quantified.

Surprisingly, GFP appeared to have a variable and non-linear dependence on temperature, close to 0.5%/°C (Figure 2.7A). This variable dependence occurred in many GFP-expressing strains in the lab. (The discrepancy from the bacteria model may be the result of a different GFP coding sequence or altered protein stability in different systems, which I did not pursue further.) However, mCherry had a linear relationship of -1.7%/°C with temperatures ranging from 15°C to 40°C, making it a suitable temperature sensor for this study (Figure 2.7B). I therefore proceeded with temperature analysis in mCherry-labeled embryos. As with the *in vitro* system, the bleaching curve for mCherry was also calculated at ~4%/500 ms exposure (Figure 2.7C) and corrected for in the subsequent analyses.

The *ceh-27<sub>pro</sub>::mCherry* transgene labels a sheet of cells on the ventral surface of the embryo at the AB128 (200 cell) stage (16 neuroblasts), such that no out-of-focus signal from planes above or below the plane of imaging affects the fluorescence measurement (Figure 2.8A). To quantify laser-induced temperature changes, we captured images of an embryo with the laser ON and OFF sequentially using the microscope setup in Configuration 2 with an mCherry filter, similar to the “*in vitro*” system.

#### **2.4.3.2 Results of *in vivo* Temperature Measurements**

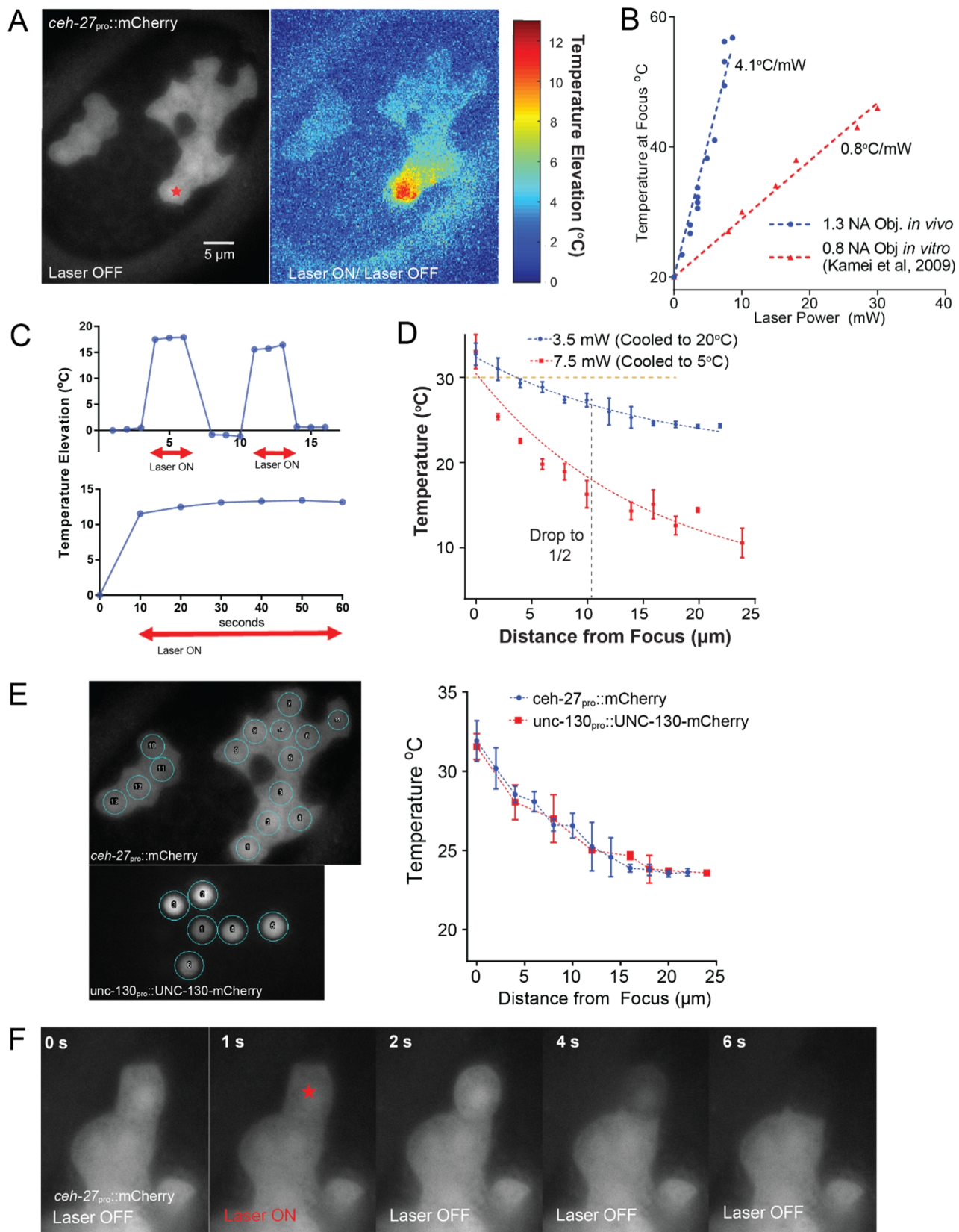
To create a 2D thermal map, the brightness changes per pixel, after dividing the laser ON and laser OFF images, were converted to temperature changes based on the temperature sensitivity of mCherry (Figure 2.8A). A thermal map of an embryo with 3.5 mW of IR laser power applied at the focus is shown. The boundaries drawn within each cell (blue circle, Figure 2.8E) were used to quantify fluorescence, both for measurements of temperature at the target cell and for spatial distributions.

Using the *in vivo* system, I found that the rise in temperature at the focus depends linearly on the power applied at a rate of  $\sim 4^{\circ}\text{C}/\text{mW}$  (Figure 2.8B), similar to the bacterial system and a much steeper rate than previously described. I also measured the time-course of heating and found that the temperature at the focus reached a steady state within 500 ms of beginning laser induction, with the temperature returning to baseline within the same time after the laser is turned off (Figure 2.8C, top). Moreover, over long heating periods, heat at the focus does not accumulate, indicating that laser power correlates to one temperature at the focus, rather than a temperature ramp (Figure 2.8C bottom).

Interestingly, the temperature distributions at different laser powers are fit by exponential-decay curves differing only by a multiplicative-scaling factor (Figure 2.8D). The distance at which the temperature elevation drops to half the maximum is always 11  $\mu\text{m}$  from the laser focus. As we suggest in the heat simulation section of this chapter, this property can be exploited to heat an arbitrarily-sized volume above the heat shock threshold, simply by altering the background temperature and the power applied. For example, if a narrower region of heating is desired, a lower ambient temperature with increased applied power generates the same temperature at the focus, while steepening the curve (Figure 2.8D, red line).

Subtle cell shape changes and dispersion of tissue occur during laser irradiation of cells. To confirm that the fluorescence decrease was due to temperature changes rather than dilution of fluorophore, a nuclear mCherry marker (*punc-130::UNC-130::mCherry*) was used for comparison. As the entire fluorescence from a cell can be measured in these experiments, without concern for the actual boundaries drawn, the summed value should

**Figure 2.8 *In vivo* Temperature Measurements** (A) Expression of *ceh-27<sub>pro</sub>::mCherry* at baseline. Asterisk indicates laser focus (left) Thermal map for 3.5 mW of Power (right) (B) Temperature at the Focus vs. Power Applied. Comparison of *in vivo* measurements in *C. elegans* with a 1.3 NA objective (blue) and *in vitro* measurements with a 0.8 NA objective from Kamei et al. (red) (C) Temperature reaches steady state immediately during and after IR laser Induction Top, the laser (4.5 mW) is pulsed between on-off states every 3 seconds, with camera exposure synchronized to the laser-on time. Bottom, heat does not accumulate at the focus over long time periods. The laser (3.5 mW) is turned on at t=10 s, coinciding with the camera exposure, and images are acquired every 10 seconds. (D) Spatial extent of heating in the x-y plane. Dashed blue and red lines represent exponential fit of distribution with plateau constrained to the background temperature. Temperature elevation drops to half maximal at ~11  $\mu$ m from target (black dashed line). Each point represents 3-7 temperature measurements taken from individual cells. Orange dashed line, heat-shock threshold. (E) Comparison of *in vivo* temperature measurement using cytoplasmic and nuclear mCherry markers. Subtle cell shape changes and dispersion of tissue occur during laser irradiation of cells. To confirm that fluorescence decrease was due to temperature changes rather than dilution of fluorescent protein, a nuclear mCherry marker (*unc-130<sub>pro</sub>::UNC-130-mCherry*) was used for comparison. As the entire fluorescence from a cell can be measured in these experiments, without concern for the actual boundaries drawn (below), the summed value should be insensitive to any changes in cell shape or movement. No differences were observed in the measured temperature or distribution using different markers. (F) Disintegration of embryonic cells after induction with previously described conditions (Kamei et al, 2009; 11 mW, 1 second). In frame 2, the laser is turned on, and in frame 3, the laser is turned off. Shortly after, the cell begins to round and the fluorescence leaks into the extracellular space, probably due to a membrane disruption.



be insensitive to any changes in cell shape or movement. No differences were observed in the measured temperature or distribution using nuclear vs. cytoplasmic mCherry markers (Figure 2.8E, right).

## **Summary and Discussion of Heating Simulations and Direct Temperature**

### **Measurements:**

I implemented two strategies for measuring the temperature elevation and spatial distribution of heat generated by an IR laser. Both the *in vitro* and *in vivo* systems demonstrated that the temperature at the laser focus depends more steeply on IR laser power than previously described (3-4x more). This suggests that previous studies raise the cell at the focus to  $25 + 11 \cdot (3 \text{ to } 4) = 58\text{-}66^\circ\text{C}$  for a short time. Indeed, during temperature measurements of the *in vivo* system at power levels near 11 mW, we sometimes observed complete disintegration of the cell at the focus (shown in Figure 2.8F), suggesting that these conditions for heating are not suitable for embryonic cells.

As also predicted by our models of the heat equation, direct temperature measurements showed that the temperature at the focus and at all points from the focus is linearly dependent on laser power. In addition, the temperature at the focus appears to reach steady-state quickly, within 500 ms, and does not show any accumulation over longer courses of heating. These properties suggest a simple strategy for heating cells with a laser: continuous heating at a constant physiological heat-shock temperature (32-34°C) can be achieved by applying 3-4 mW of laser power to the target cell, when the ambient temperature is 20°C ( $20 + 4\text{C/mW} \cdot 3 \text{ mW} = 32^\circ\text{C}$ ). According to the spatial distribution measured (Figure 2.8D), neighboring cells should not be heated above the heat shock threshold, but as we did not measure the z-distribution of heating, heating of

cells above and below the plane of focus is possible, especially given the widened laser spot size in that axis. As I describe above, cooling the sample further and compensating by increasing laser power should resolve this issue.

I did not pursue experiments to measure the spatial distribution of heat during pulsing due to technical limitations of our setup. Measuring the spatial distribution of heat during pulses is possible<sup>91</sup> but requires additional equipment. If fluorescence measurements occur over the entire duration of heating while the laser is being pulsed, then the fluorescence measured represents a time average of the temperature during the time period. Particularly if pulses are far apart, as is required for heat dissipation (see Simulations), then this will be very low. The peak distribution, when the laser is on, is of more interest. To achieve these measurements, the camera exposure can be synced with the laser pulses and summed, or more simply, the excitation light can be synced with the pulses such that the camera only captures fluorescent signal during laser pulses. It is possible to construct this circuit using simple components, but because the continuous wave system suggested a simple method for heat shock induction, we did not continue with these studies.



## **Chapter 3: Optimization of Single-Cell Heat Shock Induction using an IR Laser**

Significant optimization of induction parameters was performed to achieve cell labeling in the absence of any developmental defects and cell-specificity of induction. Early optimizations were performed using previously described conditions, and are discussed briefly for completeness. The successful heating strategy described is based on results from the direct *in vivo* temperature measurements.

As the *C. elegans* lineage is invariant, precursor cells are fated to generate specific cell identities. This characteristic is useful for many reasons for these optimization studies. First, inducing a specific precursor cell in different embryos will generate the same division patterns, migrations, and morphology of labeled cells. Thus, variations from the expected developmental pattern are a sensitive readout for cell damage. Secondly, because the same cell can be targeted across embryos, cell-to-cell variations in the heat-shock response, which could complicate early optimizations, are not present.

### **3.1 Cell Identification with Sparse Lineage-Specific Markers**

Traditionally, lineage tracing is required to identify the same precursor cell in different embryos and entails substantial manual effort. To trace a lineage from the 4-cell stage to the stage of induction (AB128), requires approximately 3 hours of observation per embryo. Though methods for automated lineage tracing have been developed<sup>31,35</sup>, these methods currently do not offer real-time identification of cells; rather the images are first acquired and then post-processed, which takes a significant amount of time (>1 hour).

To “short-cut” the process of cell identification in the embryo, I identified nuclear reporter strains that mark small subsets of cells that are related by lineage (usually lineage-specific transcription factors). Using published information about the spatial and temporal expression patterns of these transgenes during embryogenesis<sup>38</sup>, I was able to map the expected location of expressing cells onto a representative embryo at various stages<sup>36</sup> and compare them to labeled embryos. For some transgenes, the exact identity of the marked cells can easily be determined because their relative orientations follow simple patterns.

The UNC-130-GFP transgene, which is a translational fosmid reporter, has a simple expression pattern that facilitates identification of all precursor cells throughout development. The expression pattern is shown in Figure 3.1. The ten labeled cells at AB128 produce 19 neurons and 3 glial cells (more than half of the progeny), as well as other cell types, making it a useful marker for our study. Of note, the expression of the transgene from the AB128 stage is maintained in all the progeny of the labeled cells; therefore, colocalization of the UNC-130-GFP signal with the heat-shock driven signal also demonstrates cell-specificity of labeling.

Most of the studies described in the remaining chapters were performed using heat-induction of UNC-130-GFP labeled cells, because this reporter gave us access to the precursors of the amphid neurons and amphid glia for which I addressed a number of specific biological questions (Chapters 5-6). In my studies, I also identified reporters that have similar characteristics as *unc-130* through a manual search of the lineage expression database from the Waterston lab. I determined 5 criteria for “good” reporters: (1) label <30 cells at the AB128 stage (2) >50% of labeled cells should be neuroblasts or glioblasts

(3) bright enough to see by eye under my current imaging microscope (4) expression values are “binary” (either on or off at similar levels across cells). These reporters include *unc-130*, *lin-32*, *cnd-1*, *ceh-27*, and *ceh-32* (Table 2).

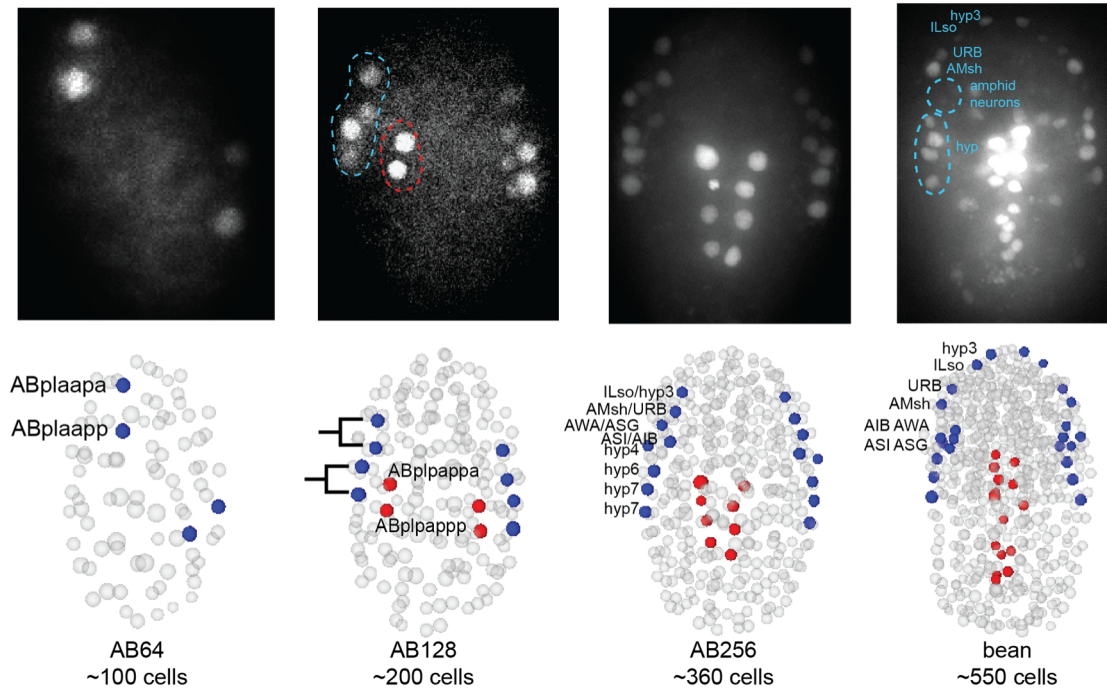


**Figure 3.1 Expression Pattern of *unc-130* translational GFP reporter.** Expression in the dorsal sublineages (ABp[l/r]aap) begins at AB64 (blue), and expression in the ventral sublineages (ABp[l/r]papp) begins in AB128 (red). At the bean stage, expression of GFP in the amphid neurons (circled, cyan) begins to fade (upper right).

**Table 2.** Reporters with Sparse Expression in neural and glial precursors at AB128.

Reporter	# Cells at ~190 Cells	# of Cells at ~350 Cells	% of Total Labeled Cells that Produce Neuroblasts or Glioblasts	# of Embryonic Neurons Generated	# of Embryonic Glia Generated
<i>unc-130</i>	12	24-28	58.3%	19	3
<i>lin-32</i>	N/A	26	84.6%	40	6
<i>ceh-27</i>	16	32	53%	31	0
<i>ceh-32</i>	24	48	70.8%	32	20
<i>cnd-1</i>	~14	~26-30	83.3%	45	3

Together, these reporters cover 49.5% (139/281) of *C. elegans* embryonic neurons and 46.4% (26/56) of *C. elegans* glia and may provide a convenient short-cut for labeling cells without full lineage tracing. (I also made promoter fusions for many of these reporters to see if they could be used directly for labeling and visualizing morphogenesis of cells. They all label too many cells to be used directly, and many become weaker during morphogenesis.)

### **3.2 Overview of Induction Protocol**

The induction protocol is shown under a timeline of embryogenesis in Figure 3.2. Embryos are first dissected from hermaphrodites and mounted onto slides using 20- $\mu$ m spacers (see Methods). The embryos are allowed to develop until AB64 or AB128, and precursor cells are identified by the UNC-130-GFP marker. After laser induction, the embryos develop for another 2-3 hours before being scored for heat-shock driven fluorescent reporter expression. For reference, the placement of the nerve ring at various stages is shown below. Note that the embryo turns in the eggshell by 90° during morphogenesis.

### **3.3 Failure of Pulsed Induction Parameters to Yield Specific or Healthy Cell**

#### **Labeling**

Previously published papers have described a variety of heating conditions to induce gene expression in cells<sup>76,91,92</sup>. Initially, our hope was that these conditions would be directly applicable to healthy cell induction in the embryo. The first paper describing the use of an infrared laser used short induction times, ~ 1 second in duration, to induce larval muscle cells, seam cells, vulval precursor cells, and the distal tip cell<sup>76</sup>. A

subsequent follow up paper used a series of short pulses (6 Hz, 8.3 ms pulses, 4 seconds) to induce expression of fluorescent reporters in neurons and early embryos (<16 cells)<sup>92</sup>. A more recent paper described different conditions for inducing early stage embryos (4-cell) and larval neurons (30-100 Hz, 1 ms pulses, variable length of 0.5-6 minutes)<sup>91</sup>. Of note, the first report induced cells for ectopic expression of genes or rescue experiments, suggesting that the cells retained function after induction, and a subset of the induced cells were precursor cells that successfully divided. However, neither recent paper with pulsing conditions applied the system to study any biological question, and aside from embryos (which were assessed only globally for hatching), neither study performed assays after heat shock induction of fluorescent proteins to test for health or function of the induced cell. In these studies, I assayed cell specificity by looking for co-localization of the heat shock reporter with the UNC-130-GFP reporter. At this time, I had not yet constructed the myristoylated versions of the heat shock reporter, so the images shown (Figure 3.3), contain heat shock-driven cytoplasmic GFP, which if the cell is labeled specifically, should co-localize with the nuclear UNC-130-GFP signal.

I first applied continuous wave (CW) induction parameters to embryonic cells, aiming to label a cell at either the AB64 stage (ABplaap) or the AB128 stage (ABplaap[a/p]). As shown in Figure 3.3B, for 1 second heat shocks at 12-14 mW, heat shock-driven GFP was sometimes seen, but the signal frequently did not co-localize with the nuclear signal, labeling cells either above or below the plane of focus. This result suggests that continuous wave heating does not localize heat sufficiently to the volume of one cell, but rather, neighboring cells were being affected by heat shock instead. Lowering power levels reduced the frequency of heat-shock driven signal, but did not

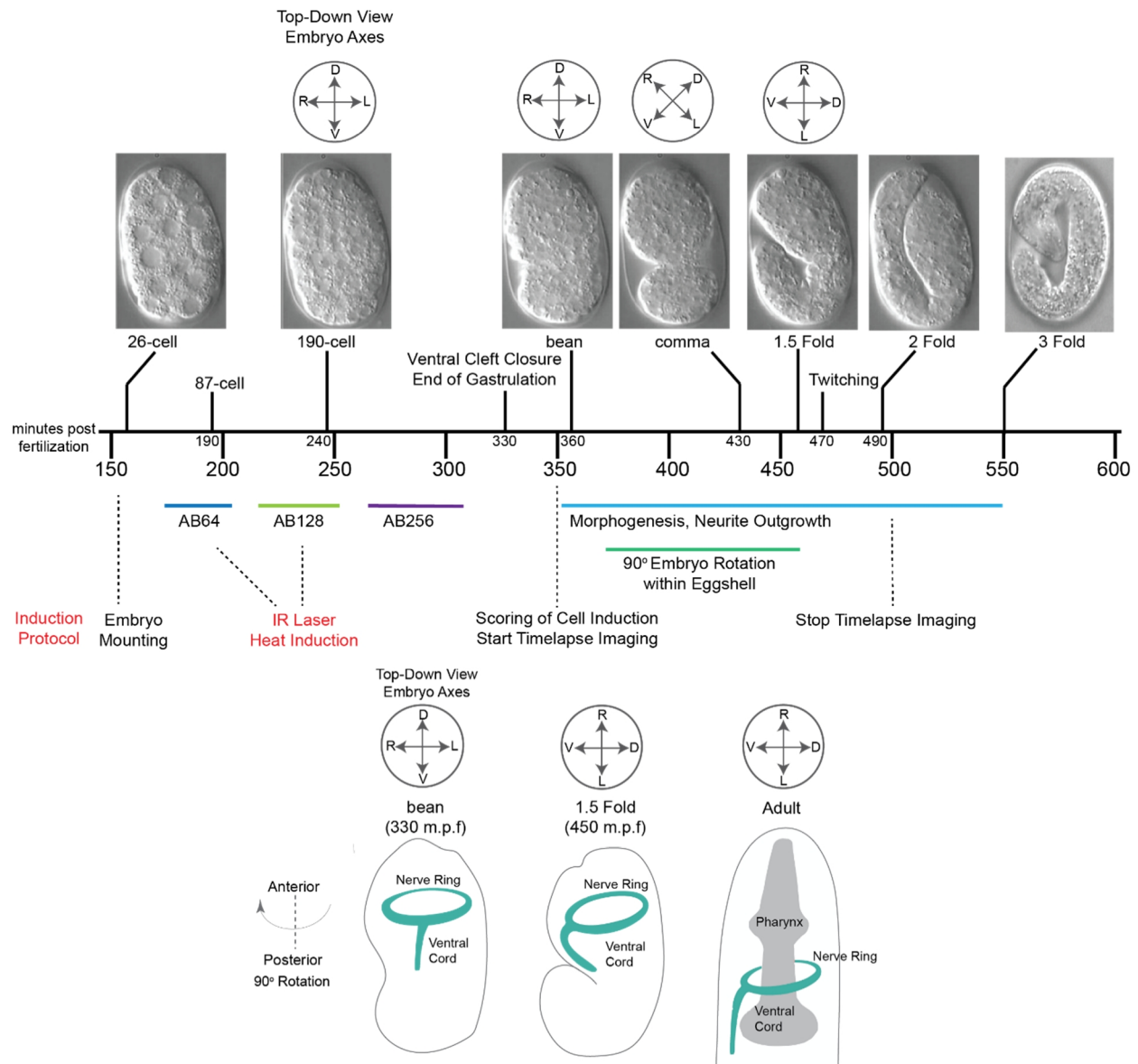


**Figure 3.2 Timeline of the IR induction protocol.** (A) Embryos are dissected from hermaphrodites (<150 m.p.f.) and mounted. The AB64 and AB128 stages are used for identification of precursor cells and for IR irradiation. Each cell at the AB128 stage will divide 2 more times, on average, to generate 4 progeny cells. By the bean stage, induction of fluorescent reporters is visible, and time-lapse imaging is initiated to visualize neurite outgrowth. Muscular twitching of the embryo begins at 470 m.p.f. (B) Placement of the embryonic nerve ring and ventral cord in the bean stage, 1.5 fold stage, and postembryonically. Soon after the onset of morphogenesis, the embryo rotates 90° within the eggshell, turning from the dorsal-ventral axis to the left-right body axis aligning to the Z-imaging axis.

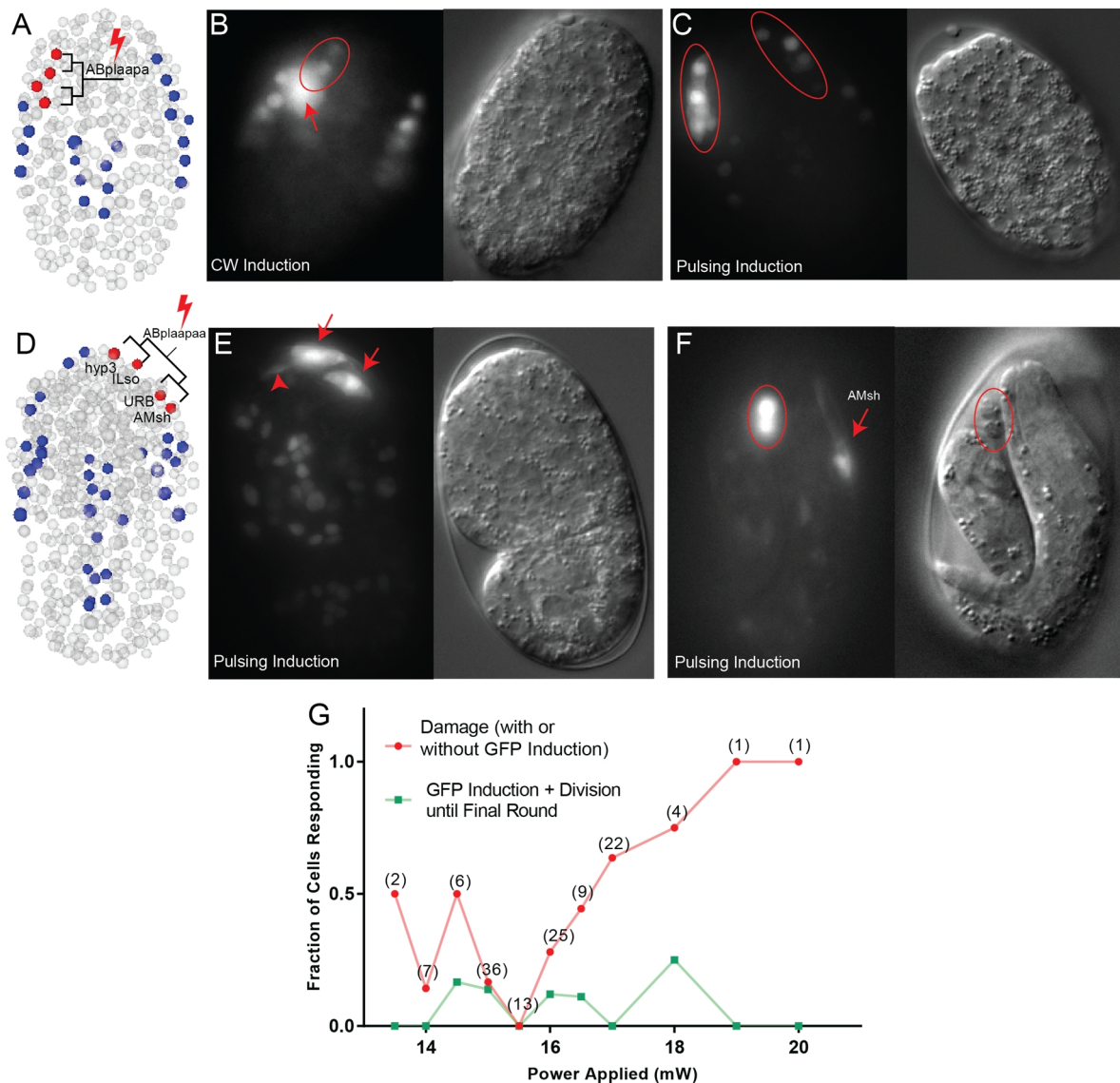


**Figure 3.3 Pulsed Parameters Lead to Cell Damage** (A) Induction at AB64 should lead to induction of 4 cells at AB256. (B) CW Induction. Heat shock-driven cytoplasmic GFP (red arrow) does not co-localize with UNC-130-GFP signal (red oval). (C) Application of Pulsed Induction Parameters. Co-localization of heat shock-driven GFP with UNC-130-GFP at AB256 on the left. UNC-130-GFP unlabeled cells for comparison on the right. (red oval) (D) Induction of ABplaapaa at AB128 leads to labeling of 4 progeny at the bean stage. (E) Heat-shock driven GFP colocalizes with UNC-130-GFP, but is present in only 2 cells, indicating that the cell has not fully divided (two arrows). Process outgrowth in the absence of full division (arrowhead). (F) Even with full cell divisions, cells fail to undergo morphogenesis and are extruded (circled red cells).

improve specificity. As I showed in the measurement section, these heat shock conditions likely heat the cell to  $\sim 65^{\circ}\text{C}$ . Indeed using these conditions during the *in vivo* temperature experiments, the cells at the focus would often disintegrate immediately (Figure 2.8F). Thus, short duration heat shocks using the continuous wave system were not sufficient to produce cell-specificity or allow for normal progression of development.

Next, I applied the conditions in Suzuki et al, using a series of short pulses (6 Hz, 8.3 ms pulses, 4 seconds). Here, the conditions did appear to label cells specifically (Figure 3.3C). However, within a range of 14-17 mW, the response was highly variable (Figure 3.3G). Cells would either: (1) become heat-shock labeled and divide to the final round (2) become heat-shock labeled and fail to divide prior to the final round, indicating cell damage (see Figure 3.3E) (3) fail to divide to the final round in the absence of any GFP signal, indicating that the cell was so damaged that it could not surmount a heat-shock response (4) divide normally in the absence of any labeling. Only a small fraction of embryos showed labeled cells dividing completely after induction (10-20%), and even in this set, cells often did not develop properly during morphogenesis. An example is shown in Figure 3.3F, where even though the cells divide until the final round, two of the four cells undergo cell death and are extruded from the cell body (red circle), whereas the other two cells (one in view) grow processes in a seemingly normal fashion. Due to the lack of consistency and concerns about cell health, I abandoned the use of these conditions. Attempts to use the Churgin et al. conditions and other long duration (5-7 minutes), high frequency pulses led to similar results (not shown).

I did, however, use these optimizations to show that pulsing an IR laser can be used for ablation experiments, alongside labeling, which I show in Chapter 6.



### 3.4 Optimization of Long Duration, Continuous-Wave Heating

After performing the *in vivo* temperature measurements detailed in Chapter 2, I aimed to create a temperature distribution that would raise a cell to 32-34°C for 5 continuous minutes. According to our measurements, heating cells with 2.5-3.5 mW of power should raise the temperature of the cell to  $20 + 4 \times (2.5 \text{ to } 3.5) = 30\text{-}34^\circ\text{C}$ , thus bringing the cell to the correct temperature.

Using the same strategy as detailed above, I induced single UNC-130-GFP labeled cells at the AB64 (ABp[l/r]aapa) and AB128 cell stage (ABp[l/r]aapa[a/p]) for 5 minutes with various power levels, and then scored for the presence of a heat shock reporter label ~2-3 hours later. Specific co-localization of heat-shock driven myr-mCherry signal with UNC-130-GFP can be seen in Figure 3.4A and B. In addition to allowing specific expression, cells divided fully with these conditions, and also appeared to have normal morphologies after development (Figure 3.4 A,B). This result was in sharp contrast to previous experiments using laser pulsing and short duration induction.

I found that at optimal conditions (~3 mW), the target cells at AB128 were induced specifically at a frequency of 60% (Figure 3.4C). Exceeding this power also resulted in cell labeling above/below the target, although expression was generally weaker in non-targeted cells (3.4D). Cells irradiated one generation prior at AB64 require slightly less power, with higher rates of specificity (85%), probably due to increased cell size, such that neighboring cells are a greater distance from the focus (Figure 3.4E). I have observed an increase in the power required to induce cells as development proceeds in other sublineages as well, suggesting that the threshold for heat shock activation increases throughout development. I also tested the effect of distance of

the induced cell from the coverslip and this only modestly affects the rate of induction (Figure 3.4F).

### 3.5 IR-labeled cells develop normally after heat shock induction

The heat shock response leads to large transcriptional changes, and heat stress itself can lead to damage to the cell cytoskeleton<sup>83</sup>. As axon outgrowth requires highly coordinated changes in cytoskeletal polymers to create cell shape changes, we reasoned that the initiation and rate of axon outgrowth would be a sensitive system to study any developmental perturbation caused by heat shock.

To first determine the normal development of a set of neurons in the embryo, we developed a combinatorial strategy (*unc-130*<sub>pro</sub>::Cre, *dyf-7*<sub>pro</sub>::lox-STOP-lox::myrGFP) to label the same cells as shown in Figure 3.5A, which originate from the UNC-130-GFP labeled ABplaapp precursor cell. The *dyf-7* promoter expresses in a large subset of sensory neurons, including the amphid neurons, and begins to express at the early bean stage<sup>69</sup>. Identifying a sequence that recapitulated the *unc-130* fosmid expression pattern was a challenge, as I found that expression in the ABplaap lineage required both elements 5 kb upstream from the start site, and the introns. To express Cre recombinase from this sequence, a bicistronic cassette was created with an SL2 sequence. Lines with transgenes expressing both cassettes exhibited specific expression in the ASI, AWA, ASG cells in a small percentage of embryos (<10%), and those embryos were used for further characterization. The death of the sister of ASI served as a useful marker for labeling in the correct lineage. Note that AIB, which originates from ABplaapp, and is labeled by heat-shock, is not labeled by our combinatorial strategy because it does not express *dyf-7*.

**Figure 3.4 Continuous Wave Heating Induces Cells Specifically and Without Damage**

(A) From left to right: Induction of ABplaapa at AB64 leads to induction of 8 precursors at the bean stage. Co-localization of heat shock-driven myr-mCherry with UNC-130-GFP is visible at AB256. Induction of 8 precursor cells at the bean stage. Dendrite growth (arrow) and axon growth (arrowhead) are visible at 2-fold.

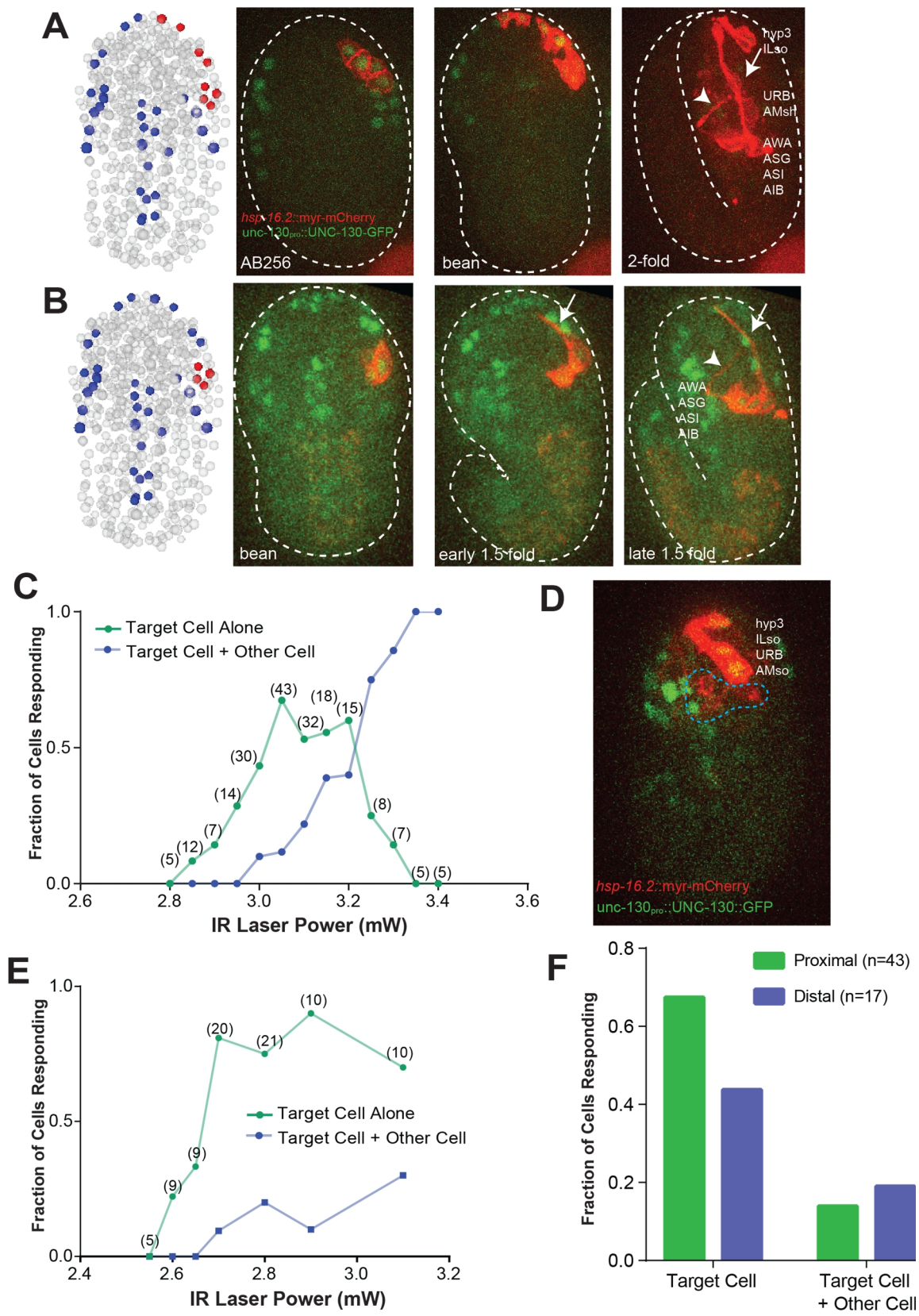
(B) From left to right: Induction of ABplaapap at AB128 leads to induction of 4 precursors at the bean stage. Co-localization of heat-shock driven myr-mCherry with UNC-130-GFP is visible at the bean stage. Dendrite outgrowth is visible at early 1.5 Fold stage (arrow) Axon outgrowth is visible at late 1.5 fold stage (arrowhead).

(C) Fluorescence induction vs. laser power. Irradiation was performed on target cells (ABplaapa[a/p]) at AB128 for 5 min, and specificity scored using UNC-130-GFP. Number of embryos irradiated for each condition is indicated.

(D) Induction of non-target cells. ABplaapaa was targeted, and the progeny, named in white, are labeled brightly by myr-mCherry and co-labeled by UNC-130-GFP nuclear signal. Additional weakly labeled cells indicate off-target induction (blue outline) and are not co-labeled.

(E) Fluorescence induction vs. laser power. Irradiation is performed on the target cell ABplaapa at AB64.

(F) Fluorescence induction is only weakly affected by cell location. Due to embryo compression during mounting (see Supplemental Methods), the dorsal-ventral axis of the embryo aligns along the z-axis of imaging. UNC-130-GFP-labeled ABplaapaa or ABplaapap lie on the dorsal surface of the embryo, and are therefore either close to the coverslip (proximal) or close to the slide surface (distal).



We quantified outgrowth in IR-labeled cells and promoter-labeled cells. Due to variation in the temperature of embryos during imaging and intrinsic variation in the rate of the developmental clock<sup>100</sup>, tail-head ratio was used as a proxy for developmental time (See Methods, Figure 8.1). Comparing axon outgrowth between heat shock-labeled and promoter labeled cells showed no variation in the timing of axon outgrowth, the rates of growth, or the final length of the axon by the 2-fold stage (Figure 3.5B).

We also introduced an *odr-10<sub>pro</sub>::GFP* reporter, expressed in differentiated AWA neurons, into the UNC-130-GFP strain. Post-embryonic expression of *odr-10<sub>pro</sub>::GFP* as well as morphology of AWA neurons whose precursor was irradiated were indistinguishable from the non-heat-shocked bilateral counterpart (9/9 animals; Figure 3.5C).

During the course of our studies, we observed a slight delay in the timing of divisions of heat shocked cells as compared with the symmetric cell homologs. While the left and right sides divided nearly synchronously in the final division (average difference = 3 min) in untreated embryos, heat shocked cells at AB128 divided on average 17 min later than the symmetric homologs in the final round of divisions (Fig 3.5D). This delay was progressive, with cells induced one generation prior, at AB64, dividing ~27 minutes later. Nevertheless, in all labeled embryos, we observed no change in the timing of axon outgrowth. We further confirmed that cell birth time is not linked to the timing of axon outgrowth in a natural setting. Using a promoter that labels neurons sparsely and

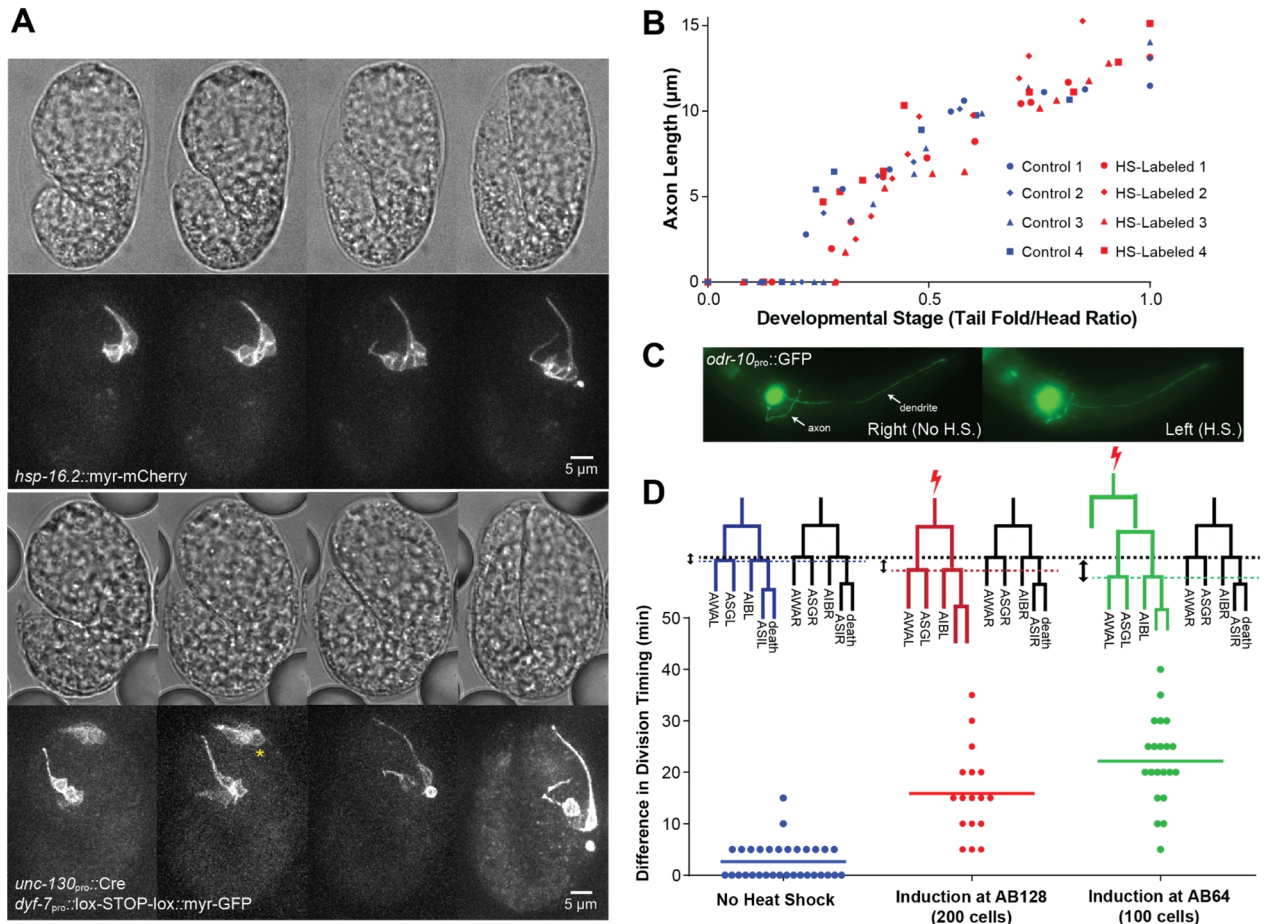


**Figure 3.5 Development of Heat-Shock-Labeled Cells Proceeds Normally.**

(A) Time-lapse imaging of IR-laser labeled and promoter-labeled cells for comparisons.

Asterisk, non-specific expression from recombinase activity. (B) Timing of axon initiation and growth is not affected by heat-shock induction. Axon length plotted against developmental stage in IR-laser-labeled ASI, AWA, ASG, AIB neurons, and promoter-labeled ASI, AWA, and ASG neurons. n=4 embryos/reporter. (C) Post-embryonic fate marker expression and axon trajectory in the AWA neuron are not affected by heat shock. Induction performed at AB64 in ABplaa. Animals scored at L3/L4 stages (D) Cell-division timing is modestly delayed in heat-shocked cells. Timing of final division of heat-shocked cells compared with contralateral homologs using the symmetric UNC-130-GFP marker. Measurements in the “no heat shock” condition are absolute differences between left and right sides. n>8 embryos for each.



symmetrically (*ceh-17<sub>pro</sub>::GFP*, labeling the SIAV, DB5 neurons) and another label for its parents (*ceh-27<sub>pro</sub>::histone-mCherry*), I quantified the differences in birth times between left-right cells, and looked to see whether this difference correlated to differences in time of axon initiation. Only 1/5 embryos displayed an obvious difference in birth time (10 minutes), but in this case, axons of these cells nevertheless grew out simultaneously (Figure 3.6).

Together, our data suggest that even though heat treatment can result in a modest delay in cell division, this has no effect on onset or progression of cell morphogenesis. This validates the use of our setup to study embryonic cell morphogenesis, and reveals that neuron generation and differentiation timings are independently controlled.

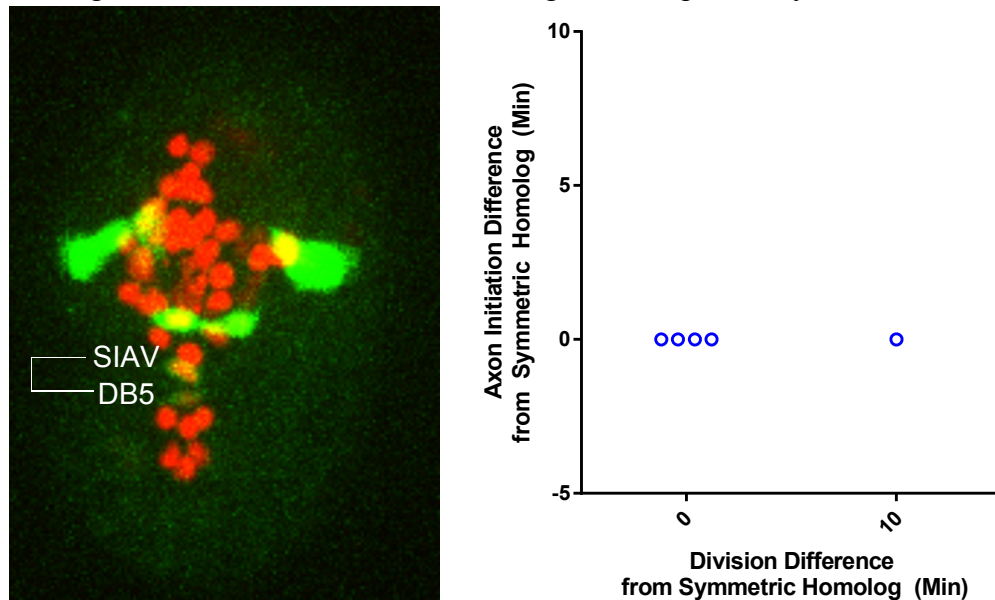


**Figure 3.6 Natural Variation in Birth Time Between Left-Right Homologs Does Not Cause Changes in the Timing of Axon Outgrowth.** Neurons were marked sparsely and symmetrically using *ceh-17<sub>pro</sub>::GFP*, and the precursors of those cells (and others) were marked using *ceh-27<sub>pro</sub>::histone-mCherry*. Left, the SIAV/DB birth time was correlated to the axon outgrowth time of SIAV. Right, despite changes in the timing of divisions in the left-right precursor cells, axons of the descendants always grow out simultaneously. Images were acquired every 5 minutes.

**Summary:**

I describe the use of lineage-specific markers (e.g. *unc-130*) to identify precursor cells from single time points and score cell-specificity of induction and cell damage without the need for full lineage tracing. Though I initially attempted to use previously described conditions for single-cell heat shock, I found that these conditions were not compatible with the embryo, and caused frequent failure of cells to divide or undergo morphogenesis. Heating with low power over long durations (5 minutes) mitigated these problems, and heated cells are labeled at high frequency (>60%) and undergo normal divisions and growth patterns.

To confirm that heat shock does not affect axon outgrowth, we compared the development of heat-shocked cells to promoter-labeled cells. Importantly, we did not observe any changes in the timing of growth when compared to the overall development of the embryo. We did, however, observe that heat shock caused a variable amount of delay of cell divisions in the parental cells. Interestingly, this indicates that axon outgrowth time is determined independently of cell birth time, perhaps by some global, cell-extrinsic cue.



## Chapter 4: Labeling and Tracking of Development in Diverse Cell Types

Having optimized continuous wave IR induction parameters for targeted gene expression in specific precursor cells at AB128, I aimed to show that these conditions can be used to label diverse cell types and track morphological changes. For this study, I characterized wildtype development at high resolution for ~30 cells in the embryo; assuming bilateral symmetry, these represent approximately 10% of the cells in the embryo. These studies revealed a number of previously undescribed growth patterns. Using our system, I identified a retrograde mechanism for axon extension in the AVB and RIV interneurons. I also addressed long-standing hypotheses about early nerve ring entrants using data about the timing of axon outgrowth for a small set of neurons. IR labeling was also used to visualize sensory organ formation, hypodermal migration and fusion, and excretory cell elongation.

### 4.1 Testing Irradiation Conditions in Various Sublineages

In order to identify cells for targeting without the need for lineage tracing, we developed a strategy to use lineage-specific nuclear markers, such as *unc-130* (described in Chapter 3, Figure 3.1). *unc-130* is expressed in ~10 easily identifiable cells at AB128, after which the progeny maintain expression<sup>38</sup>. By labeling different precursor cells marked by *unc-130* and looking for specific colocalization of the heat-shock driven label, we found that our optimized IR irradiation condition successfully labels cells of diverse cell types, including the sensory neurons, interneurons, glial cells, hypodermal cells, and the excretory system. Within these cell types, we did notice subtle changes in the strength

and frequency of labeling, but all inductions performed were within 0.3 mW of the optimized conditions shown in Chapter 3, Figure 3.4. Alongside time lapse imaging, striking morphological changes in these cells were visible, as cells grew from undifferentiated precursors to their characteristic endpoint morphologies.

Because neurons and glia in sublineages labeled by *unc-130* grow processes in common structures, we also labeled precursors neighboring UNC-130-GFP cells, which generate cells that migrate away from each other after birth, in order to visualize growth of single neurites (Figure 4.1, 4.2 C,D). In these studies, the expected location of the progeny cells, from a representative fully-lineaged embryo<sup>36</sup>, as well as the shapes of the cells that emerged from a lineage, served as checks on the specificity of induction.

The sublineages in which IR labeling was tested are shown in Figure 4.1. Time lapse sequences of these cells are shown in Figure 4.2. For specific neuron-generating lineages, additional images with annotations are given with more detail in Figure 4.3 and 4.4.

As cells closely related by lineage in *C. elegans* often have very different fates, I group our observations by cell type, sometimes compiling results from labeling of different precursors. Axon outgrowth of the amphid neurons is described in detail in Chapter 5. Note that the embryo rotates 90° in the eggshell during morphogenesis, from the dorsal-ventral axis aligning with the z-axis to the left-right axis. Figure 3.2 can be used to assist with orientation when looking at time sequences of development.

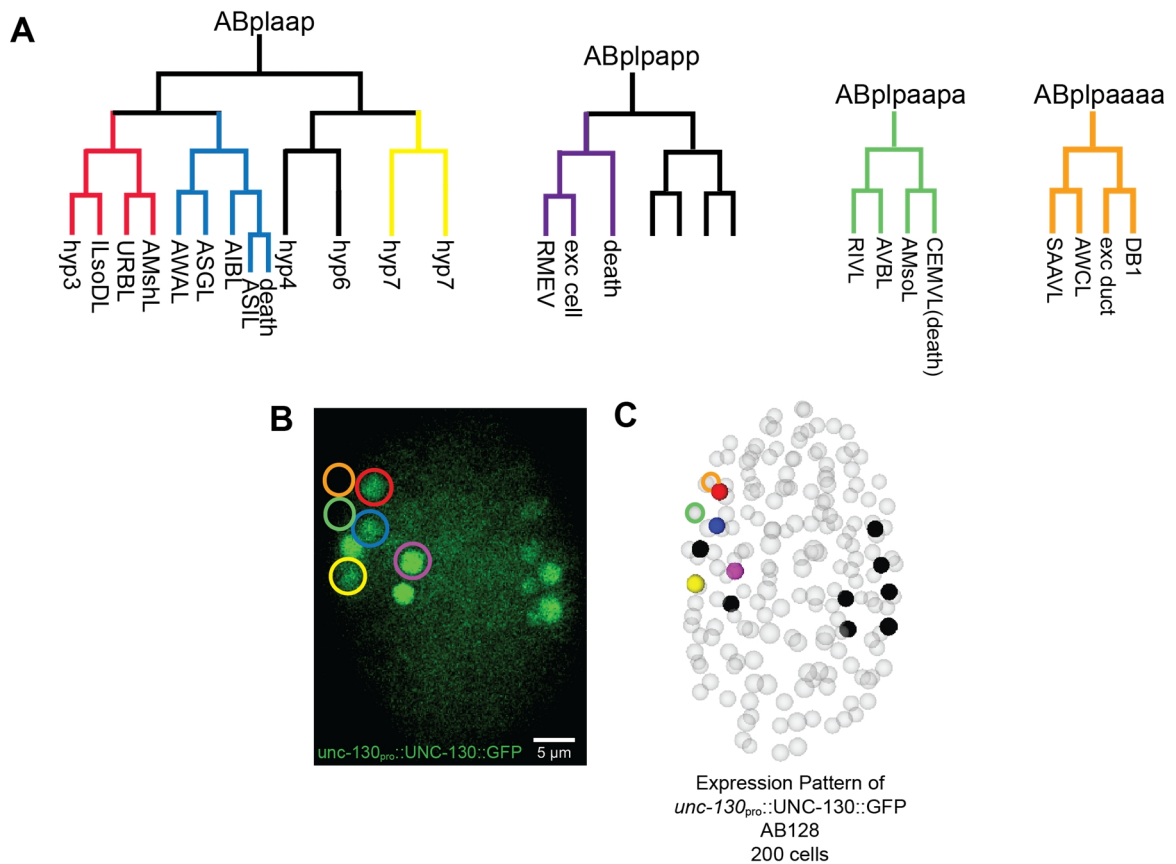


**Figure 4.1 Cell lineages in which induction was performed.**

(A) Induced precursor cells and their progeny. Colors correspond to experiments shown in Figure 4.2-4.4.

(B) Expression pattern of UNC-130-GFP nuclear marker at AB128. Circled cells were targeted for labeling in separate experiments. ABplpaapa (open green circle) and ABlpaaaa (open orange circle) were identified by relative location to UNC-130-labeled cells.

(C) UNC-130-marked cells are shown on coordinates from a representative fully-lineaged embryo at AB128

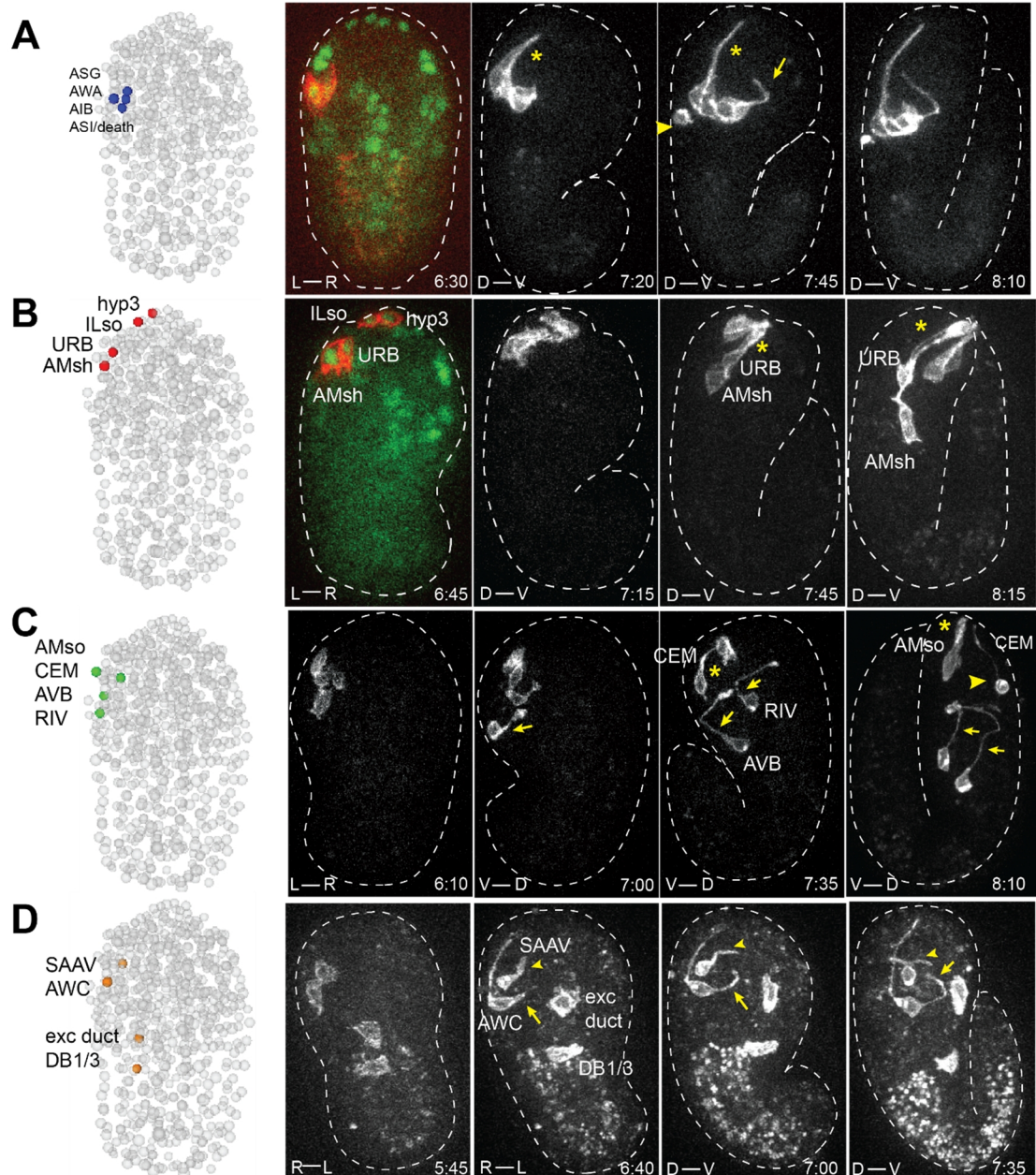


**Figure 4.2 \*C/F +IR Labeling in Diverse Cell Types.**

(A) Amphid neurons undergo retrograde dendrite extension (star) and axon extension ventrally and then dorsally into the nerve ring (arrow). ASI sister-cell death is visible (arrowhead).

(B) Sensory glia and neurons are born near the nose-tip and extend retrograde processes

(C) Proximal axon segment of AVB and RIV (arrow), CEM-neuron early stages of death (arrowhead) are visible. See Figure 4.3 for additional detail.

(D) Extension of SAAV (arrowhead) and AWC (arrow) into the nerve ring. See Figure 4.4 for additional detail.



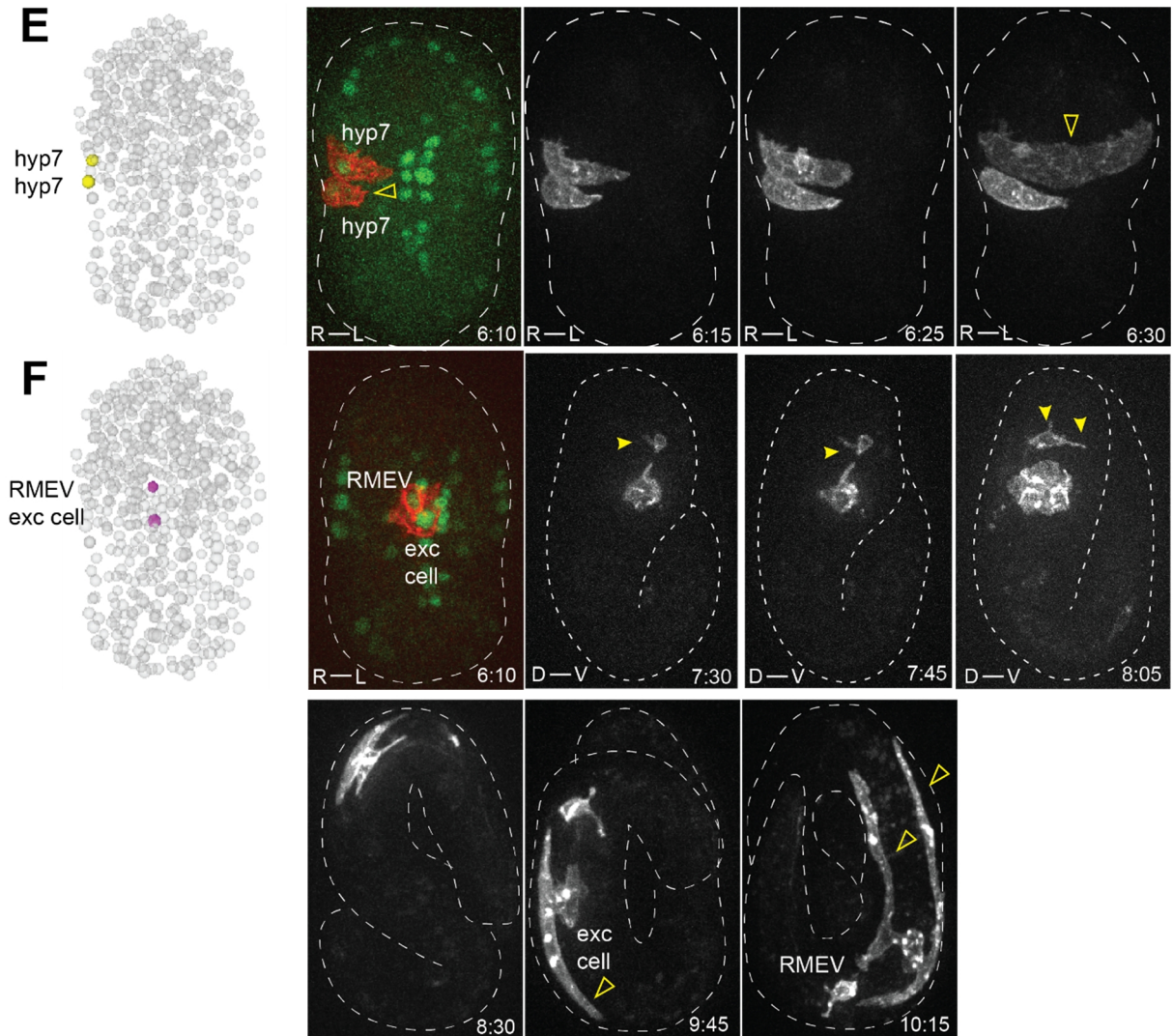


**Figure 4.2 \*G/H'IR Labeling in Diverse Cell Types.**

(E) Ventral migration of hypodermal cells and fusion. (open arrowhead)

(F) RMEV growth into the nerve ring (closed arrows) and excretory cell elongation (open arrowhead) and. Images are spliced from two embryos, (top row and bottom row)

(A-F) Labeled cells are shown on coordinates from a fully-lineaged embryo after the final division is complete (ref) (left). The embryo axis of the imaging plane is shown at the bottom left of images. (D-V, dorsal-ventral; R-L, right-left). Times are given relative to comma stage (7h:10m; ref).

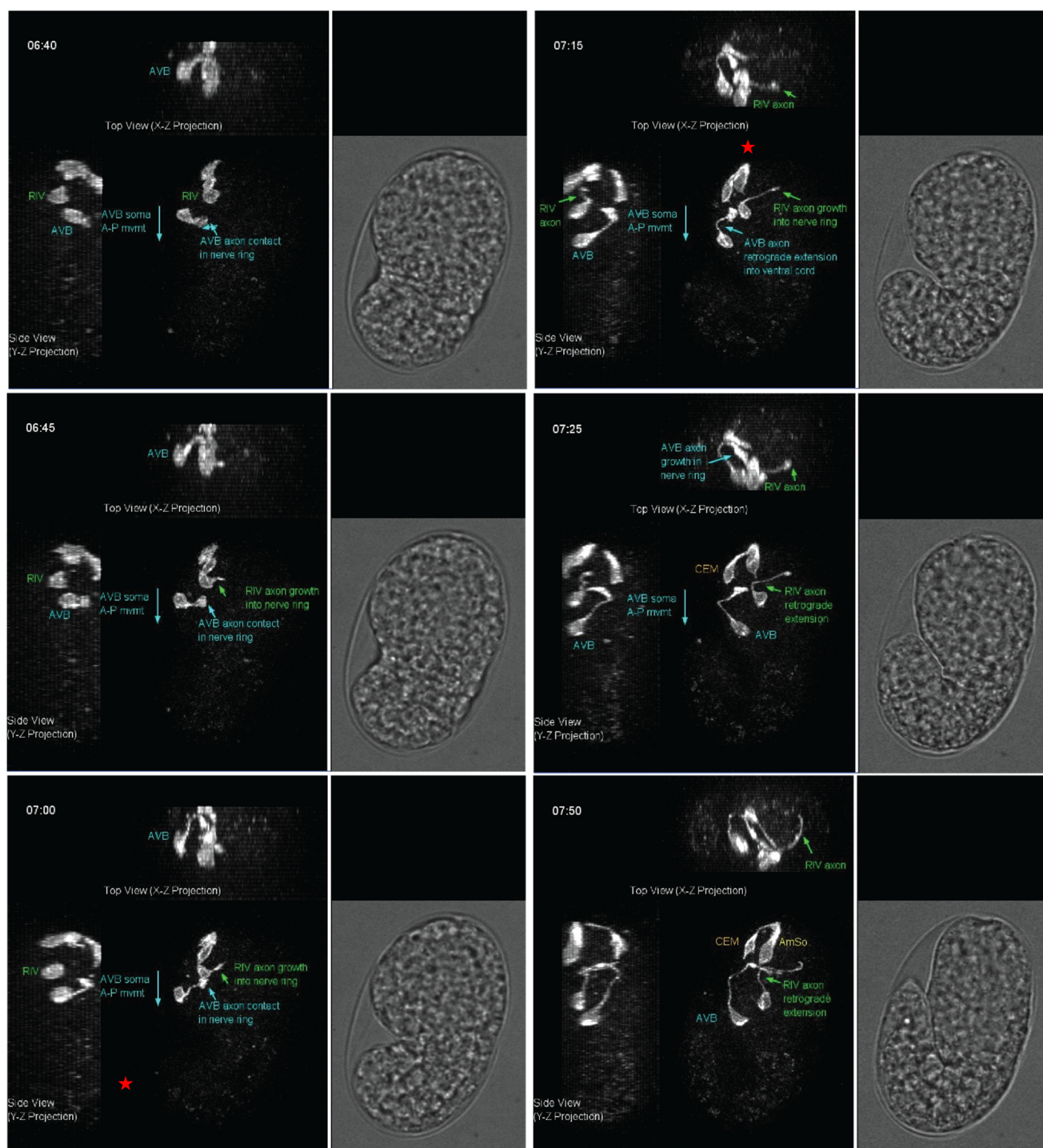


**Figure 4.3 Development of AVB, RIV, AMso, CEM cells.** Note the large growth cone-like axon projection on AVB at 7:00-7:15 (red star). Both AVB and RIV undergo retrograde extension to generate the proximal part of the axon.



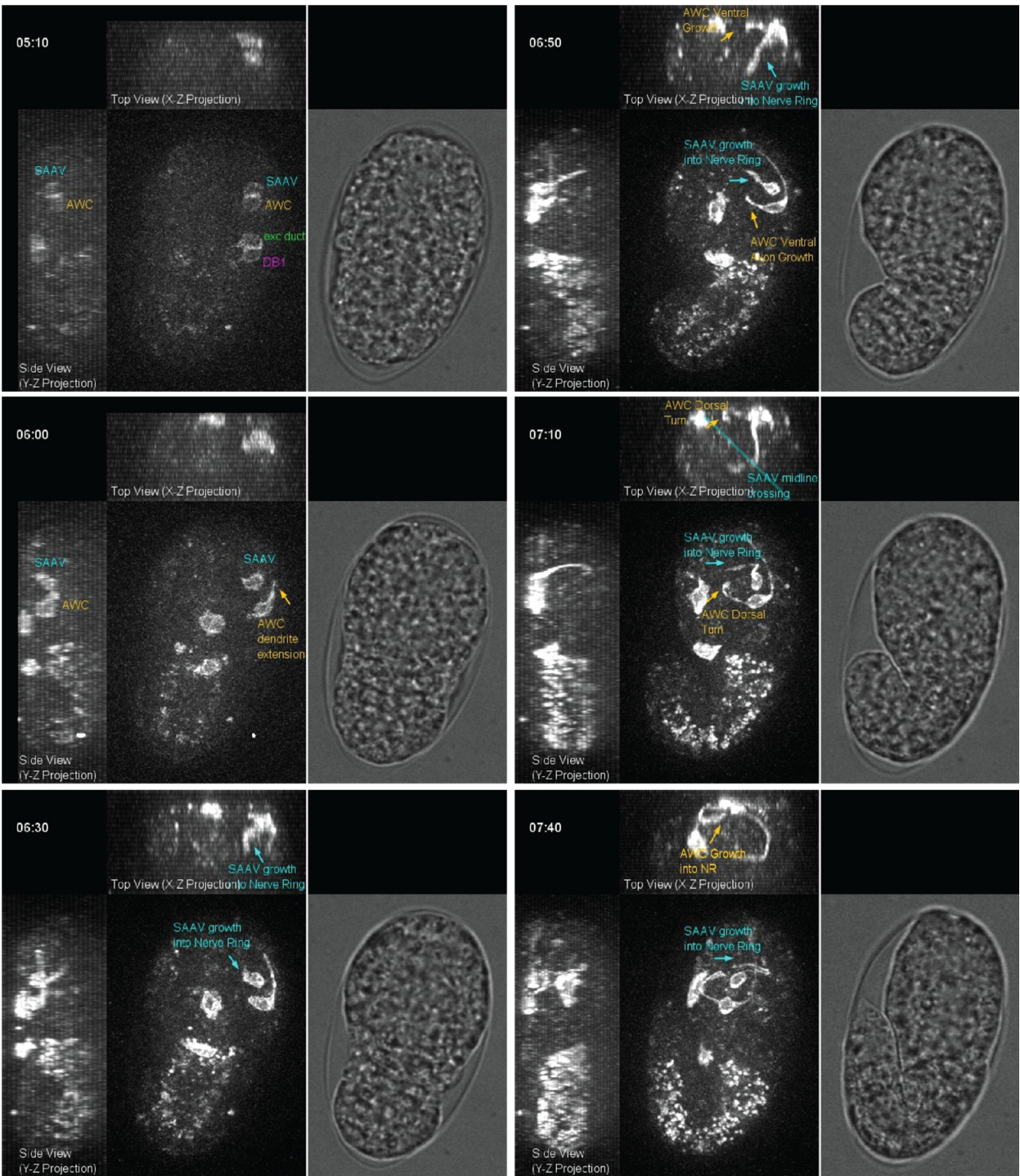


**Figure 4.4 Development of AWC, SAAV, excretory duct, and DB cells.** Note the growth of the SAAV neuron in the Top View (X-Z Projection). The SAAV neuron crosses the midline at around ~7h:00m.p.f. Note that AWC begins ventral growth at ~6h:50mp.f., and turns dorsally around 7h:10m.p.f.

## 4.2 A Retrograde Extension Mechanism in the AVB and RIV Interneurons

Targeting the IR laser to the ABplpaapa precursor resulted in labeling of two interneurons, AVB and RIV, whose development had not previously been characterized in the embryo. With time-lapse imaging, we observed how their final morphologies emerged (n=3).

As seen in Figure 4.3, at ~6h:40m post fertilization (p.f.), the AVB neuron makes contact in the nerve ring (NR) with a small ventral-dorsal extension. Strikingly, growth into the nerve ring then pauses for ~30 minutes, while the cell body pivots around the stationary axon, migrating posteriorly and dorsally away from the nerve ring. This migration appears to extend the cell-body proximal portion of the axon. Interestingly, while this retrograde axon extension takes place, a large growth cone, comparable in size to the cell body, is evident at the axon tip, perhaps tethering the axon to resist the migrating cell-body pull (Figure 4.3, 6h:45m.p.f. -7h:15m.p.f.). The distal part of the axon then resumes growth ventrally to dorsally into the nerve ring to complete the trajectory (7h:20 m.p.f.-7h:50m.p.f.). Remarkably, this mode of axon growth is also employed by the co-labeled RIV neuron, although in this case the order of events is reversed. Over a period of 35 minutes (6h:45m–7h:20m post fertilization), RIV extends an axon dorsally into the NR. Once growth is complete, the cell body migrates posteriorly, laying down the proximal axon segment. While dendrites have been shown to grow by retrograde extension<sup>69</sup>, this system demonstrates that axons can grow by this strategy as well.

The method of growth employed by AVB and RIV is highly reminiscent of the granule cells in the cerebellum, where the axons first bifurcate in the densely-packed



molecular layer and then the cell bodies migrate radially, leaving behind an axon<sup>101</sup>.

Thus, AVB and RIV neurons may be suitable for studying this poorly-understood guidance process. A recent study has shown that the AIY neuron also grows by retrograde extension, suggesting that this may be a broadly conserved mechanism of axon outgrowth in the *C. elegans* nervous system<sup>41</sup>.

#### **4.3 The Order of Axon Entry into the Nerve Ring**

Several studies have proposed pioneers of the nerve ring, but the earliest entrants to the NR are not known. The AVA and AVB interneurons have been suggested based on their early Netrin expression, since the pioneers of the ventral cord, AVG and PVPR, express Netrin during ventral cord formation<sup>27</sup>. The RME neurons are anatomically well-positioned to be pioneer cells based on their juxtaposition to the nerve ring-associated GLR cells and head musculature. In more recent studies, the neurons of the sublateral commissure, in particular SIA and SIB, have been proposed to have pioneer functions; in mutants defective in nerve ring placement and formation, rescue of the defects in the entire structure can be achieved by cell-specific rescue in SIA and SIB<sup>28</sup> (Rapti et al., submitted); a recent study in our lab imaging a subset of nerve ring neurons using sparse-promoter labels has shown that the SIA and SIB neurons are the earliest entrants observed (Rapti et al., submitted).

The sublineages in which irradiation was performed generated 8 cells with visible processes in the nerve ring (the neuron URB is not included as its axon was not visible by the 2-fold stage). This includes the interneurons SAAV, RIV, RMEV, AVB, and the amphid neurons and interneuron, AWC, AWA, ASG, ASI, and AIB. Among these cells, the SAAV neuron is by far the earliest entrant, with a process visible in the nerve ring at

6h:20m, at the early bean stage as seen in Figure 4.4 (n=3). Interestingly, this cell appears to reach the midline by before the comma stage (Figure 4.4, 7h:00m), circumscribing the entire nerve ring by 7h:30m, when the axon is visible on the ventral end of the other side of the nerve ring (Figure 4.4, top-down view); notably, IR-mediated labeling allows visualization of events after midline crossing, unlike most symmetric-promoter based drivers. Symmetric promoter-based labeling strategies have shown that nerve ring closure (when the left and right sides meet at the midline) for the SIA and SIB neurons occurs around twitching (~7h:30m.p.f.), suggesting that the SAA neurons may actually precede these other sublateral neurons. Still, no studies have elucidated a pioneer function for the SAA cells. The RIV neuron also appears to grow early (Figure 4.3, 6h:55m) into the NR. Interestingly, the AVB neuron has a large growth cone-like contact at the ventral entry area of the nerve ring early (Figure 4.3; ~6h:50m), but extension into the NR does not occur until later (7h:20m); thus while AVB may be involved in directing neurons to the ventral point of the NR, a role in guiding cell growth within the NR is less likely. RME does not initiate axon growth until 7h:30m, suggesting it is a latter component (Figure 4.2F). After first growing ventrally in the amphid commissure, all of the amphid neurons observed appeared to make the dorsal turn to grow into the NR relatively late (AWC at ~7h:10m, Figure 4.3; ASG, ASI, AWA, AIB at ~7h:30m; Figure 4.2A). As shown for the amphid neurons in Figure 3.5B, all of our neuron tracking experiments revealed that the timing of outgrowth for cells is highly stereotyped. Thus further labeling and imaging of nerve ring components could provide insight into the order by which the structure is formed.

#### 4.4 Sensory Organs

Previous studies demonstrated that sensory organ neurons are born near the nose tip and extend anchored dendrites by posterior migration of the cell soma<sup>30,69</sup>. Time-lapse imaging of labeled cells confirmed this retrograde extension of amphid sensory dendrites (n=12; Figure 4.2A). By labeling other glia and neurons with anterior processes, we also found that the same mechanism operates for AMsh (n=10) and AMso (n=4) amphid glia, and for neurons and glia associated with other sensory organs (URB and CEM neurons, ILso glia; Figure 4.2B, C).

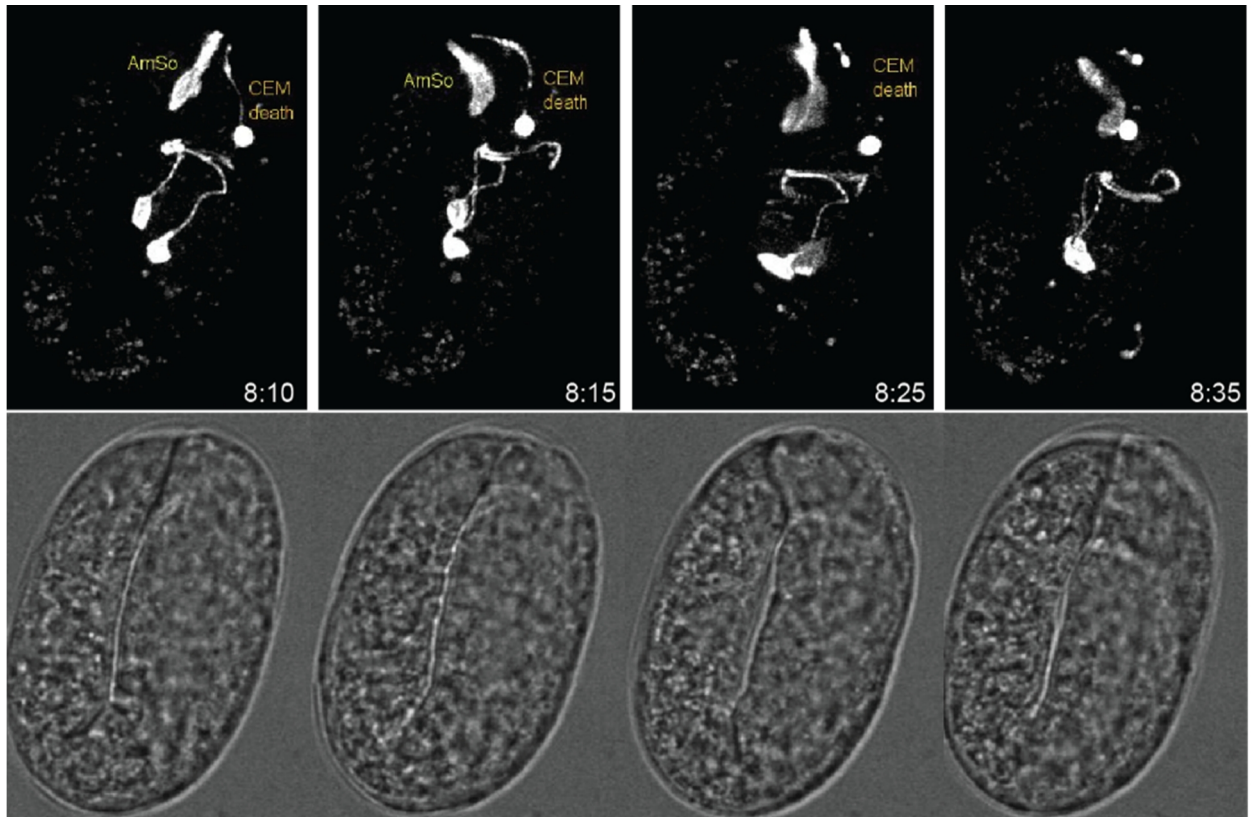


**Figure 4.5 Death and Process Clearance of the CEM Neuron.** Note the proximal part of the process is cleared prior to the distal process.

The CEM neuron, a male-specific sensory neuron, dies in hermaphrodites and survives in males. We found that this neuron extends a dendrite before cell death ensues (Figure 4.3), an observation not previously reported. This is interesting in light of the fact that only 2 other cells in *C. elegans* programmed to undergo cell death actually differentiate before death, the tail-spike cell and the linker cell.

We were surprised to see that the death of the CEM neuron appears to follow a very similar progression to the death of the tail-spike cell, the focus of another study in our lab (P. Ghose, personal communication). Like the tail-spike cell, the proximal part of the process fades early in the degeneration sequence, essentially separating the distal part of the process from the cell body. The distal process of the CEM neuron then shrinks and fragments, and this part persists, just like the distal portion of the tail spike cell (Figure 4.5). Through genetic screens, Piya Ghose has shown that the process and cell body of the tail-spike cell appear to require different machinery for death and clearance. In particular, the *eff-1* fusogen appears to be required for distal process clearance in the tail spike cell, which has a known role in axonal fusions and dendrite sculpting. As the tail spike cell has no molecular similarities to neurons, the CEM neuron is an attractive setting to study the role of this gene in degeneration of the dendrite, and studies are ongoing to test the molecular similarities between the CEM neuron and the tail-spike cell.

#### **4.5 Other Cell Types**

I also tested the ability of the system to label cells outside of the nervous system. I targeted the UNC-130-labeled precursor of the hyp7 cell, which eventually forms a large-syncytium around the animal. During early morphogenesis, the anterior precursor migrates towards the ventral midline and then fuses with the hyp7 cell from the other side

(Figure 2.2E). The leading edge of the hypoderm and the filopodia-like projections were highly visible with our labeling strategy, which can be an advantage over commonly used cell-junction markers which do not localize to the leading edge. We also observed that immediately after fusion, the myr-mCherry signal rapidly (within 5 minutes) diffused to label the entire binucleated cell. Thus, due to the asymmetric nature of IR labeling, fusion events can be seen clearly.

Labeling of the excretory cell revealed that extensive elongation of the lumen occurs within the first 2-3 hours of the 3-fold stage (Figure 2.2F). For this experiment, the embryo was imaged for ~5 continuous hours, and the reporter did not show signs of bleaching. This indicates the perdurance of the heat-shock driven reporter, which should allow for visualization of events even late into the 3-fold stage of embryogenesis.

## **Summary**

In this section, I used IR-mediated gene expression to track and label cells of diverse cell types. I demonstrate a retrograde mechanism of outgrowth in the AVB and RIV interneurons. I also address hypotheses regarding possible pioneer cells of the nerve ring. IR induction can also be used to visualize cell deaths clearly, like the sister of the ASI cell (Figure 4.2A), and the CEM neuron, which undergoes a complex developmental sequence to clear its dendrite (Figure 4.5). Most of our findings regarding embryonic development of cells were previously uncharacterized, and thus IR-labeling is likely to reveal additional insights when applied to a broader set of cells.

## Chapter 5: Characterization of Amphid Neuron Growth Dynamics in Wildtype and Guidance Mutants

In *C. elegans*, the amphid neurons comprise the largest chemosensory organ, with 12 sensory neurons bilaterally. Amphid axons follow a characteristic trajectory; they first travel ventrally, where they are fasciculated in a bundle called the amphid commissure, before turning anteriorly and dorsally to enter the nerve ring (Figure 5.1). Genetic screens in *C. elegans* have uncovered several evolutionarily-conserved families of ligands and receptors that participate in axon guidance, including *sax-3*/Robo receptor and *vab-1*/Ephrin receptor<sup>25,26,102–104</sup>. Both *sax-3* and *vab-1* mutants have defective amphid neurons trajectories<sup>26,103</sup> (see Table 3). However, past studies have characterized *sax-3* and *vab-1* mutants using endpoint assays, and how these defects arise during development is not known. Moreover, mutants of these pathways exhibit >50% embryonic lethality, suggesting that there may be additional defects visible in embryos that do not survive to larval stages.

We sought to use our IR labeling system to characterize the dynamics of amphid axon growth in wildtype animals and make quantitative comparisons to *sax-3* and *vab-1* mutants. Given that the amphid neurons appear to have stereotyped axon growth dynamics in wildtype animals (Figure 3.5), we reasoned that any deviations would be easily visualized. We noticed during our studies that *sax-3* and *vab-1* mutants had slower developmental rates and increased sensitivity to imaging. Thus, tail:head ratio was used to compare the developmental stages between wildtype and mutant embryos (See Materials and Methods, Figure 8.1).

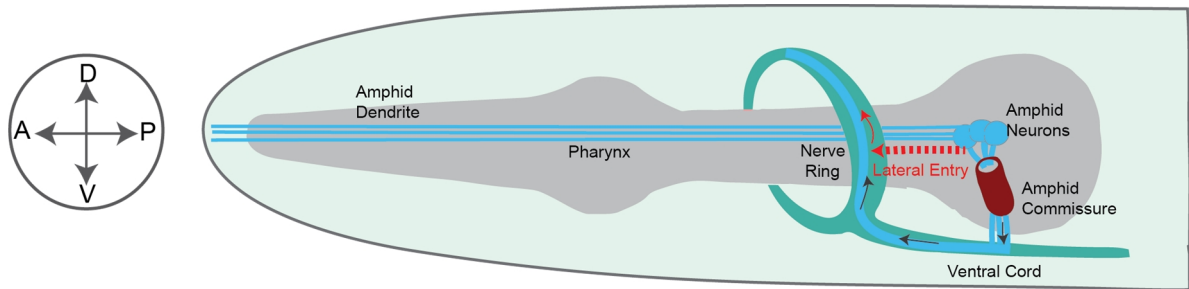


**Figure 5.1 Trajectory of the Amphid Neurons.** The axons of amphid neurons first travel ventrally in the amphid commissure, and then anteriorly through the ventral cord and dorsally into the nerve ring. In some guidance mutants, the amphid neurons travel a shorter path, entering the nerve ring laterally and bypassing the commissure (red).

### 5.1 Wildtype Amphid Axon Growth Dynamics

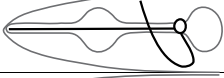
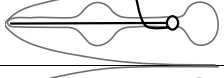


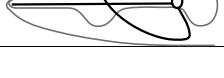
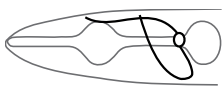
I examined the wildtype axon-navigation dynamics of four amphid sensory neurons, AWA, ASI, ASG, and AWC, in which postembryonic defects have been previously described<sup>26,103</sup>. The AWA, ASI, and ASG neurons can be labeled by irradiating their common grandparental precursor, ABp[l/r]aapap (Figure 4.2A, Figure 5.2). After dendrite extension, neurons extend axons ventrally in the early 1.5-fold stage (7h:30m), then turn dorsally to enter the NR, with full axon extension observed by 8h:15m (n=8). Note that due to fasciculation, the trajectories of single neurites cannot be seen.

Irradiating the ABp[paaaa] precursor cell labels the left AWC neuron, as well as the SAAVL and DB1 neurons, and the excretory duct cell. The AWC axon follows a growth sequence similar to AWA/ASI/ASG (Figure 4.4); however, as SAAVL is already fully grown into the nerve ring at the time of ventral-to-dorsal turning, the growth of the AWC neuron could not be followed in the nerve ring and labeling in this sublineage was

not used for further characterization. Interestingly, AWC initiates ventral growth much earlier (6h:45m) (n=4) than the other subset of amphid neurons (ASI, AWA, ASG), suggesting that all amphid neurons do not grow out axons simultaneously. Rather, there may be series of coordinated events that lead to the development of the commissure (see Section 5.4).

**Table 3: Embryonic and Postembryonic Imaging for *sax-3* and *vab-1* mutants.**

Embryonic defects were characterized by labeling the AWA, ASI, and ASG precursor at AB128 or AB64 (ABp[l/r]aapap or ABp[l/r]aapa). Postembryonic defects were characterized in L3/L4 animals using an AWA-specific marker for *sax-3(ky123)*, *odr-10<sub>pro</sub>::GFP*, and an AWC-specific marker, *odr-1<sub>pro</sub>::YFP*, for *vab-1(dx31)*.

	Phenotype	<i>sax-3(ky123)</i> AWA postembryonic n>50	<i>sax-3(ky123)</i> embryonic n = 31	<i>vab-1(dx31)</i> , AWC postembryonic, n > 50	<i>vab-1(dx31)</i> embryonic n = 27
	Wildtype	43% (23)	52% (12)	63% (35)	76% (16)
	Lateral Axon	13% (7)	26% (6)	38% (21)	24% (5)
	Anterior Axon	22% (12)	22% (5)	0% (0)	0% (0)
	Axon Termination	6% (3)	0% (0)	0% (0)	0% (0)
	Anterior Nerve Ring	15% (8)	0% (0)	0% (0)	0% (0)
	Arrest Prior to NR Entry		(6)		(6)
	Dendrite Misplacement/ Breakage		(2)		



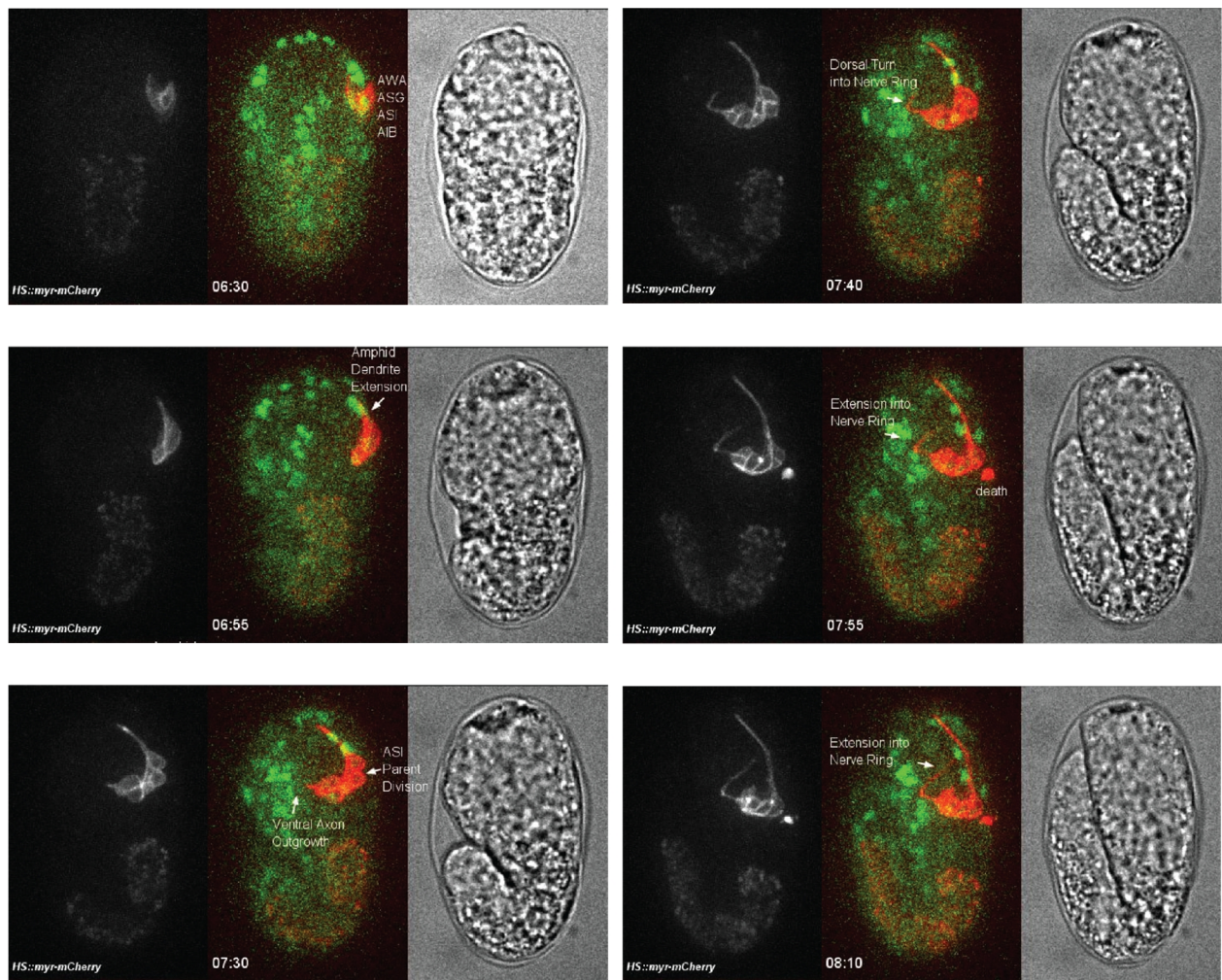


**Figure 5.2: Wildtype Imaging of AWA, ASG, ASI amphid neurons and AIB interneuron.** Growth of the amphid dendrites begin at 6h:30m.p.f. and grow in a retrograde manner. Ventral axon outgrowth begins at the early 1.5-fold stage at 7h:30m.p.f, with full extension into the NR visible by 8h:10m.p.f.

## 5.2 *sax-3* Mutant Growth Dynamics

*sax-3* mutant animals that are characterized post-embryonically show a number of defects in the trajectory of the amphid neurons (Table 3); however, defect etiologies are not known. Previous studies have shown that ~30% of *sax-3* animals show anterior axons; these axons may form after normal axon initiation, wandering anteriorly after failure to turn into the nerve ring; or may initially fail to grow, and only extend processes much later, as has been shown for sensory activity mutants<sup>105,106</sup>. We found that in all *sax-3* embryos with anterior processes, the timing of axon initiation was unaffected, suggesting that *sax-3* acts specifically to regulate axon incorporation into the nerve ring (Figure 5.3A,B).

Other post-embryonic defects in these mutants, including lateral entry into the nerve ring which bypasses the ventral commissure, also appear to arise by failed navigation and do not have defects in the timing of axon outgrowth. Interestingly, in some embryos with aberrant axon trajectories (4/11), axons forked and retracted branches (Figure 5.3A), rather than following a simple continuous path as seen in wildtype animals. This mode of growth suggests that redundant cues may exist in the extracellular space, allowing axons to guide to targets in the absence of signaling from guidance receptors. Notably, these forking patterns were only seen in animals with defective trajectories. Alternatively, the locations of forking may suggest the existence of key decision nodes along the axon migration path. Due to low number of animals in which this phenotype was seen, as well as the low temporal frequency of imaging, we were unable to correlate the location of these forking events to locations in the trajectory.

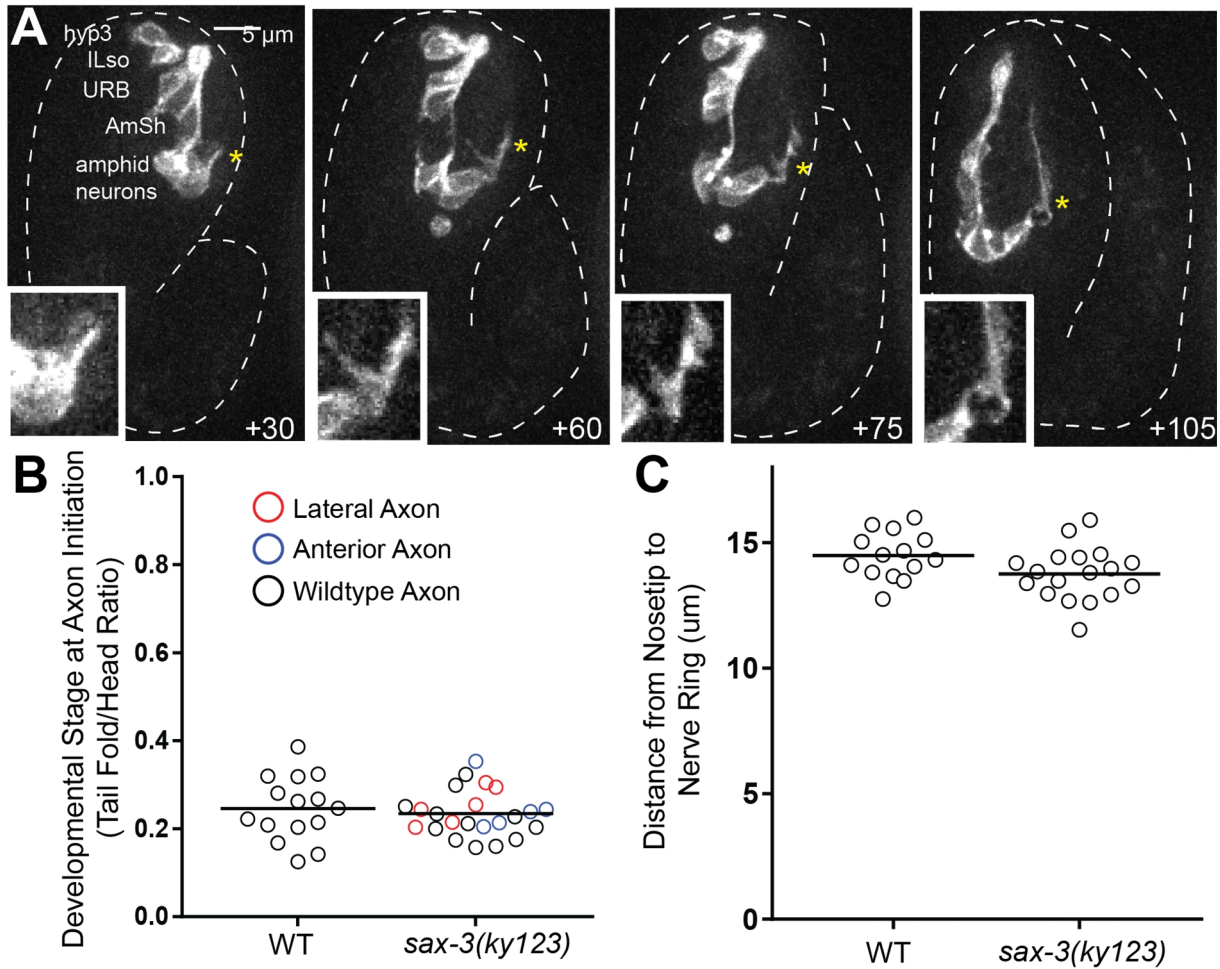


**Figure 5.3. Characterization of Embryonic Guidance Defects in *sax-3* Mutants.**

(A) Embryonic imaging of anterior amphid axon growth and failure to turn into the nerve ring in *sax-3(ky123)*. Induction performed at AB64 in ABplaapa. Inset: Magnified image of starred region showing forking and retraction of axons during growth. Time, minutes from comma stage.

(B) The initiation time of axon outgrowth is not affected in *sax-3* mutants.  $n=15$  embryos for WT,  $n=23$  embryos for *sax-3(ky123)*.

(C) Anterior nerve-ring placement is not pronounced in *sax-3* mutants. Distance measured from nose-tip to nerve ring in 2-fold embryos.  $n=15$  embryos for WT,  $n=18$  embryos for *sax-3(ky123)*.

While we were able to observe many defects of *sax-3* mutants during the time of nerve ring formation in the embryo, our data suggests that anterior placement of the nerve ring may occur after the nerve ring is already formed. An anteriorly misplaced nerve ring was present in 15% of *sax-3* larval animals, but measuring the distance of the nerve ring from the nosetip in the 2-fold embryo did not reveal differences between *sax-3* and wildtype embryos (Figure 4C). This suggests that the nerve ring in *sax-3* forms in the correct location, but may be displaced during elongation. Alternatively, the nerve ring may be misplaced in the early embryo with respect to other structures, like the pharynx, but does not show an early global positioning defect.

We also observed low-penetrance defects in dendrite placement (2/31) that had not previously been described for *sax-3/Robo*. In one embryo, the dendrite of the amphid neurons initially extended in the right-left-axis before turning and correcting its trajectory to the anterior-posterior axis (Figure 5.4A), while another showed defasciculation of the amphid dendrites (Figure 5.4B), which are always seen as a single bundle in wildtype animals.

In the small set of embryos examined ( $n = 23$ ), we did not observe large overall differences in the fractions seen with different amphid neuron trajectories as compared with post-embryonic scoring; this suggests that the type of defect does not significantly affect the ability for the worms to continue development. We did, however, note that a large percentage of embryos ( $n = 8$ , 26% overall) failed to make it through twitching during imaging, which we attribute to increased sensitivity to excitation light, but could be related to particular growth defects, which were not observed due to the early arrest.



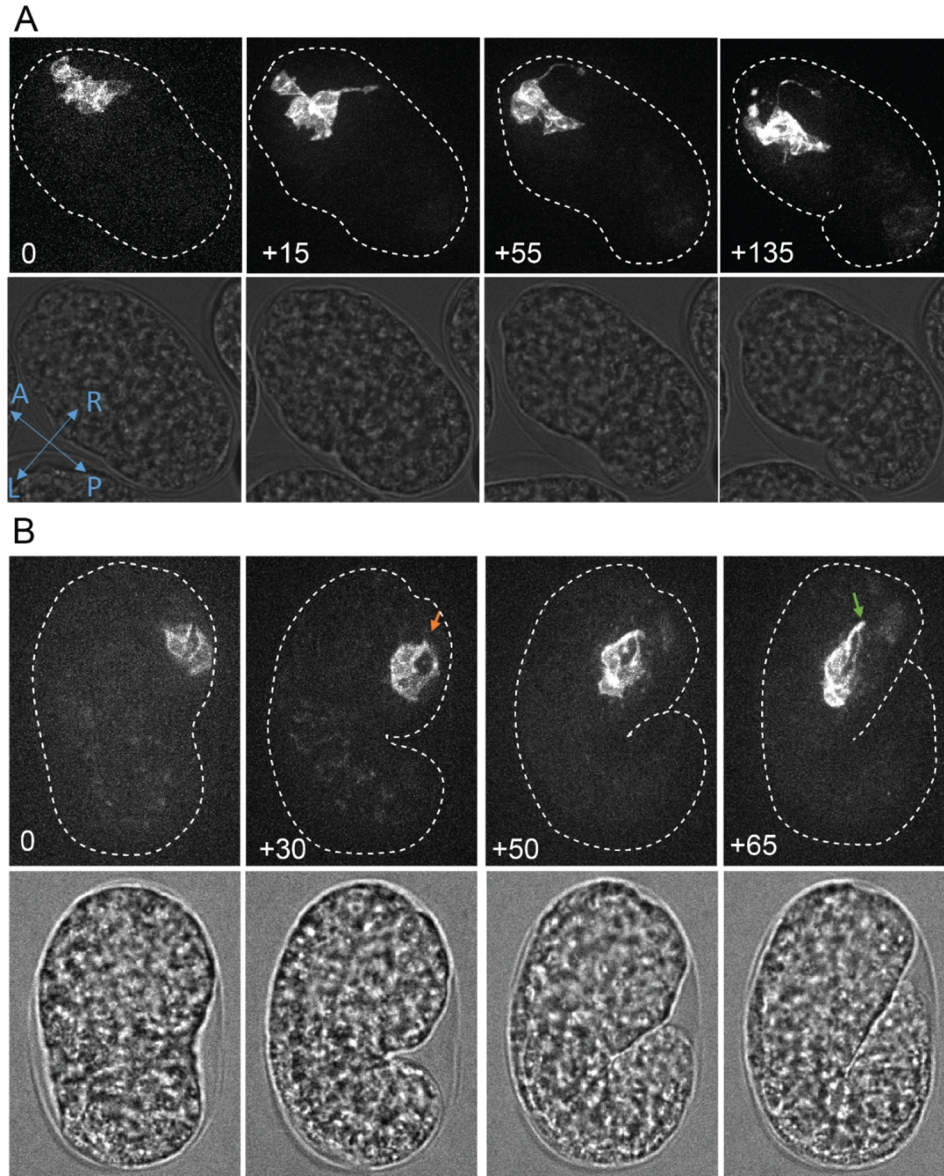


**Figure 5.4: Defects in Dendrite Placement in *sax-3(ky123)*.** (A) Dendrite extension of amphid neurons occurs in the anterior-posterior axis in wild-type animals (Figure 5.2). In one *sax-3(ky123)* embryo, the dendrite begins to extend in the left-right axis before turning and correcting its trajectory to the anterior-posterior axis. This embryo arrested prior to twitching. (B) Dendrite extension occurs in 2 separate bundles (red arrow), rather than one, as normally seen in wild-type animals. The processes do not extend to the nose-tip in the 2-fold embryo (green arrow), indicating that the dendrites are shorter than normal. Time for both time lapse image series are given in minutes from the first image shown.

### 5.3 *vab-1* Mutant Growth Dynamics

Unlike *sax-3* mutants, *vab-1* mutants have a single guidance defect: in ~30% of animals, aberrant lateral axons project directly towards the nerve ring, failing to make the initial ventral turn. Interestingly, laterally-projecting axons begin at the same location and reach the same destination, the dorsal part of the nerve ring, as wildtype animals, but the path length traveled by lateral axons is shorter (see Figure 5.1, Figure 5.5 A, B). We asked if, in *vab-1* mutants, the dynamics of axon growth was altered to compensate for the shorter path taken. For example, if the timing of the turn is controlled independently of the path (e.g. by an absolute timing cue or cell-intrinsically), the turn into the nerve ring (ventral-to-dorsal) should occur at the same time with either path. However, if a compensation mechanism exists, laterally projecting axons would be expected to turn later, in order to reach the destination at the same time as axons that initially project ventrally (Figure 5.5B).

Remarkably, unlike wild-type axons, laterally-projecting axons do not immediately turn dorsally when contacting the nerve ring. Rather, a delay in dorsal turning is evident (Figure 5.5C). (The timing of dorsal turning in wildtype and mutant embryos is shown by the large data points. Because absolute developmental time cannot be used to compare between wildtype and mutant embryos, we used a measure of developmental time that is based on morphology of the embryo and unfortunately, does not allow tracking past the first 2-fold time point. Further growth into the nerve ring often happens afterwards, and therefore the final axon length, which is often longer, is not shown. See Methods, Figure 8.1.)

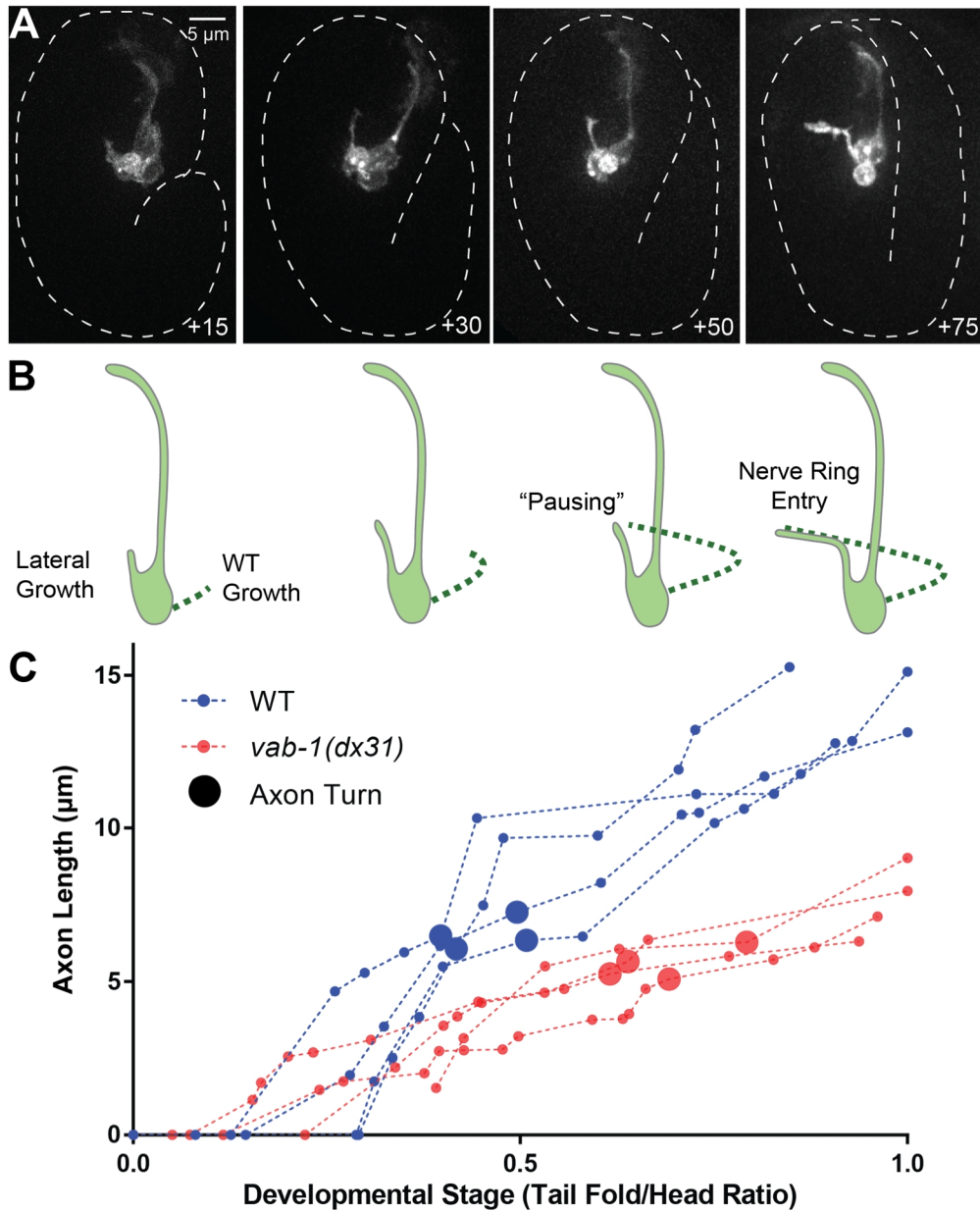


**Figure 5.5 Characterization of Embryonic Guidance Defects in *vab-1* Mutants.**

(A) Embryonic imaging of amphid neurons in *vab-1(dx31)* showing lateral trajectory. Time, minutes from comma stage.

(B) Model for timing compensation in nerve-ring entry in *vab-1* mutants.

(C) Axon trajectories during nerve-ring entry are shorter in *vab-1* mutants, and the dorsal turn occurs later.  $n=4$  embryos each for wild-type and *vab-1(dx31)*.

The delay in dorsal turning for *vab-1* mutants suggests that the nerve ring has a competence period for the navigation of some axons. It is possible, for example, that axons require guide processes to grow, and if these have not formed, axon growth will stall. Thus our setup allows for quantitative comparisons of guidance decisions on a cellular level between embryos and between different genetic backgrounds. The study of *vab-1* mutants also unmasks a previously unknown mechanism for regulating outgrowth during nerve ring assembly.

#### **5.4 Order of Development in the Amphid Commissure**

Interestingly, in *vab-1*/Ephrin mutants or animals in which the *kal-1*/Kallmann syndrome's gene is overexpressed, studies have shown that all amphid neurons in a bundle follow a single trajectory ("all or nothing" defect), despite the incomplete penetrance of the defect in the whole population<sup>103,107</sup>. Based on this result, these studies have proposed the idea of a "pioneer neuron" for the amphid commissure, which determines the path of all follower neurons.

I performed a preliminary characterization of the growth into the commissure for the amphid neurons, given that there are only 12 neurons. Unfortunately, the availability of markers to identify the precursor cells at AB128 was very limited, so I performed one experiment in which I induced the precursors of the amphid neurons at the AB64 stage, where 3 additional precursors, in addition to the two described for AWC, AWA, ASG, and ASI, generate the rest of the amphid neurons. At AB64, these cells could be identified simply by eye with respect to UNC-130-labeled cells (Figure 5.6, top).



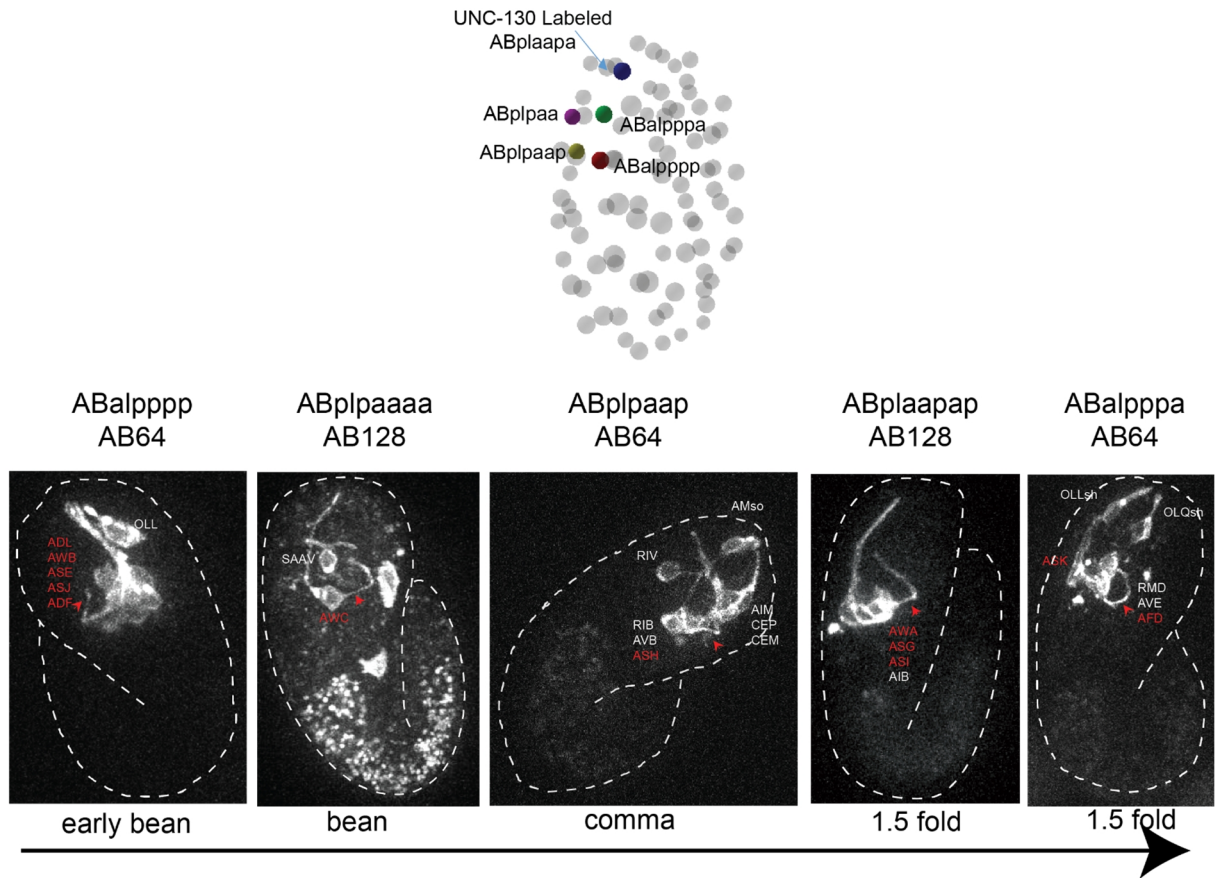


**Figure 5.6 Characterization of Growth into the Amphid Commissure**

(top) Cells generating amphid precursors were induced at the AB64 stage and identified with respect to UNC-130-labeled ABplaapa.

(bottom) Order of growth into the amphid commissure. The final trajectories of labeled neurons are shown, rather than the earliest time point of ventral growth.

The order of growth seen into the commissure is shown in Figure 5.6 ( $n = 1$  for each labeling experiment). Also note that since many amphid neurons are labeled in each experiment, it was not possible to tell from which cell the process emerged, and therefore the order is given based on the first growth of a ventral process. (Since the growth of the ventral process was not visible easily in maximum projections, the final patterns of labeling at the 1.5-to 2-fold stages, when the embryos have turned, are shown.) Nevertheless, interestingly, the AWB neuron, which has been proposed to be a pioneer based on rescue experiments, is contained within the set of neurons in which I first observed ventral growth<sup>103</sup>. Further characterization with labeling in smaller subsets of cells, perhaps at the AB128 stage, or using Cre-lox recombination with a more specific promoter (e.g. *dyf-7<sub>pro</sub>*, which limits expression to the amphid neurons) should allow further resolution of these cell sets.

### **Summary:**

The invariant lineage of *C. elegans* offers an opportunity to label the same cells across different genotypes and make quantitative comparisons of growth dynamics. These studies are further facilitated by the fact that wildtype dynamics of axon growth appear to have little variability (Figure 3.5). Here I studied the growth dynamics of the AWA, ASG, ASI amphid neurons and compared them to growth in *sax-3/Robo* and *vab-1/Ephrin* mutants, which have been shown to have endpoint defects in amphid growth. We found that the timing of axon initiation is not affected in either mutant, suggesting these receptors act specifically to guide the axon, rather than control the timing of growth.

*In vivo* imaging of retinal growth cones in *robo2* mutants in zebrafish has revealed that Robo has roles in error correction<sup>18</sup>; while wildtype retinal growth cones make rare errors, which are corrected, *robo2* mutants have larger, more elaborate growth cones that make frequent errors, accompanied by growth and retraction. Interestingly, in about 1/3 of embryos with defective amphid growth in *sax-3* mutants, we also observed forking and retraction of the amphid axons, suggesting that this role may be conserved.

Using our setup, we also made quantitative comparisons between wildtype axon growth dynamics and *vab-1* mutants, which project laterally into the nerve ring. By identifying differences in the timing of the dorsal turn, we identified a previously unknown checkpoint governing the timing of nerve ring entry. Identifying the mechanism that governs this difference is likely to be challenging. Performing ablation experiments of neighboring cells in the nerve ring or synaptic partners, while concomitantly labeling the amphid neurons and tracking growth, could be a first step to identifying the source of the timing cue. Using an IR laser for both labeling and ablation is discussed in Chapter 6.

## **Chapter 6 Applications of IR Laser-Mediated Gene Induction and Cell Ablation**

In this chapter, I show that IR laser cell targeting is a versatile tool. In addition to being used for labeling and tracking of cells, IR laser induction can be used to express any gene of interest with spatiotemporal control. Therefore, it can be used for investigation of gene function, which provides a distinct advantage over strategies for labeling cells by photoconversion or by stochastic genetic methods. I also explore the use of an IR laser for specific cell ablation using induction parameters that heat the targeted cell to lethal temperatures. By using different conditions, different cells in a single embryo can be ablated and labeled, allowing tracking of the progression of a defect in labeled cells as development proceeds.

### **6.1 Embryonic Rescue of the Amphid Channel in *daf-6*/Patched-Related Mutants**

As IR laser induction can be used to express any gene of interest in a specified cell at a specified time, we used this approach to determine the site of action for *daf-6* in the formation of the amphid compartment during morphogenesis. *daf-6* encodes a Patched-related protein which acts to limit the size of the amphid compartment. In wildtype animals, the socket and sheath cells form a connected tube through which some amphid dendrites are exposed to the outside environment. In *daf-6* mutants, the amphid compartment is abnormally enlarged, and the neurons often project into large vacuoles in the amphid sheath (AMsh), failing to exit the channel<sup>108</sup> (Figure 6.1A).

The defect of the amphid sensory compartment can be assayed by dye-filling; when exposed to the lipophilic dye, DiI, 100% of wildtype animals take up the dye into exposed amphid neurons, whereas 0% of *daf-6* animals are able to dye-fill. The complete

penetrance of the defect in the *daf-6* mutant was useful for our studies, as any rescue was significant and therefore, a large number of animals did not need to be induced and scored.

Previous studies have shown that *daf-6* is expressed in both the amphid socket and sheath cells during embryogenesis<sup>108</sup>. Serial electron microscopy of *daf-6* embryos has shown that bloating of the amphid channel becomes apparent during morphogenesis, suggesting that *daf-6* is required in the embryo<sup>109</sup>.

To test the spatial and temporal requirements of *daf-6*, we expressed *daf-6* specifically in the precursor of the amphid sheath at AB128 by laser heat shock induction (Figure 6.2B). Our transgenic line carries a *hsp-16.2::daf-6* transgene with a *unc-130<sub>pro</sub>::UNC-130-GFP* marker, which is expressed in the precursor of the amphid sheath at AB128. (Thus, the presence of UNC-130 marker indicates that the heat shock-driven transgene is present in the precursor and not lost from mosaicism.) 8/27 operated animals were rescued for the dye-filling defects on the heat-treated side of the animal, while neurons on the non-heated side failed to fill with dye (Figure 6.3C,D). This demonstrates that *daf-6* activity in AMsh glia is sufficient for sensory-organ morphogenesis.

The *daf-6* defect was only rescued in ~30% of animals in our experiment, whereas previous studies have shown that expression of *daf-6* under its own promoter achieves nearly complete rescue<sup>108</sup>. There are several possible explanations for the incomplete rescue. One explanation is that the *daf-6* protein is unstable, and after heat shock induction, does not persist in the progeny cell until the time at which it is required. If additional kinetics considerations are taken into account, genes can be constitutively

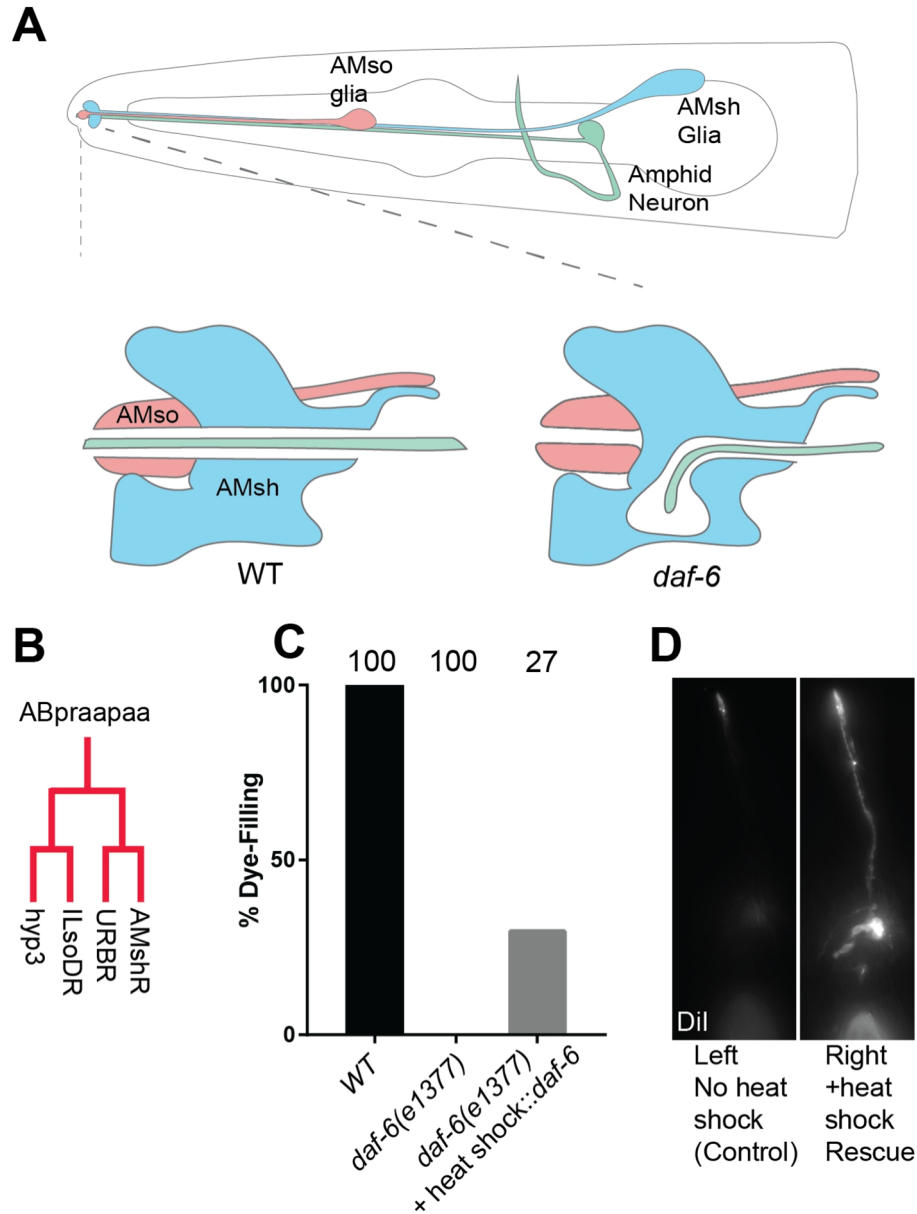


**Figure 6.1: IR Laser-Induction of *daf-6* in the amphid sheath can rescue defects in the development of the amphid channel**

(A) Schematic showing wildtype formation of the amphid channel. The socket and sheath glial cells form a tube through which some amphid neurons extend cilia. In *daf-6* mutants, the cilia of neurons fail to exit the channel.

(B) Induction of the grandmother of the amphid sheath at AB128.

(C) Rescue of dye-filling defects by IR laser induction. Number of animals scored in the upper margin.

(D) Dye-filling defects rescued on the right side of the animal (heat shocked) as compared with the left-side (no heat shock).

expressed for the rest of development using recombinase-based heat shock strategies to overcome this issue (Figure 2.1).

The heat shock induction requirements of our *daf-6* expression and mCherry labeling lines may also differ due to effects of the transgene copy-number; our strategy could be improved by introducing concomitant expression of a fluorescent protein (through an bicistronic cassette or with a 2A cleavage peptide) to assay for the induction of heat shock. Alternatively, *daf-6* may be required in additional cells, including the socket cell, in order to achieve a stronger rescue.

## **6.2 Simultaneous Cell Ablation and Cell Labeling Reveals a Role for Glia in Dendrite Extension**

Laser ablation has been used to eliminate single cells in the *C. elegans* embryo and observe the effect of the perturbation on the development of neighboring cells, revealing physical and signaling interactions between cells<sup>110,111</sup>. Laser ablation is generally performed using 440-nm pulsed dye lasers, which kill cells through an unknown mechanism, likely through oxidative stress or DNA damage. We explored the use of an infrared laser to ablate a cell at the focus, by raising the temperature of the cell to lethal temperatures, and heat-shock label a neighboring cell, via our previously optimized induction parameters, in a single embryo. Indeed, femtosecond infrared lasers have been used for precise cutting of axons in *C. elegans*<sup>112,113</sup>. Unlike ablation-only strategies where the defect is generally scored post-embryonically due to the easier availability of cell markers, IR-mediated ablation and labeling in the same embryo allows us to directly track the effect of the ablation on the development of the labeled cells.

Previous studies, as well as experiments presented here, demonstrate that *C. elegans* amphid sensory neurons grow dendrites by retrograde extension<sup>69</sup>. These studies raise the possibility that AMsh glia, which tightly associate with these dendrites, promote dendrite anchoring as cell-body migration ensues. However, because early embryonic promoters specific for the amphid sheath to drive genetic ablation are not known, this idea has not been directly tested. In *C. elegans*, previous studies in our lab have shown that embryonic ablation of the CEP sheath glia causes shortened CEP neuron dendrites, as visualized after hatching<sup>29</sup>.

First, we modified our induction parameters to achieve cell ablation of the precursor of the amphid sheath at the AB128 stage in the embryo. Simply raising the power levels to damage cells at the focus led to off-target heat shock induction. As I showed by heating simulations, pulsing the laser is expected to reduce heat accumulation away from the focus, allowing for targeting specificity. During the course of our optimizations (Chapter 3, Figure 3.3), I found that the conditions published in Suzuki et al. produced labeling specificity in the embryo at the AB64 and AB128 stages, although the cells frequently arrested shortly after induction. Thus, I used a slightly modified version of these conditions (6Hz, 8.3 ms pulses, *10 seconds*) at higher powers (14 mW) to cause specific cell-ablation. At power levels of 11-13 mW, we occasionally found that the cell targeted for ablation was labeled by heat-shock induction, but increasing the power prevented this response, likely because it killed the cell immediately. Using these modified ablation conditions, we found that the precursor cell was ablated in 12/12 embryos (Figure 6.2A); a cell was scored as ablated if the precursor cell failed to divide to the final round by ~200 min after ablation. Importantly, after ablation, the timing of the



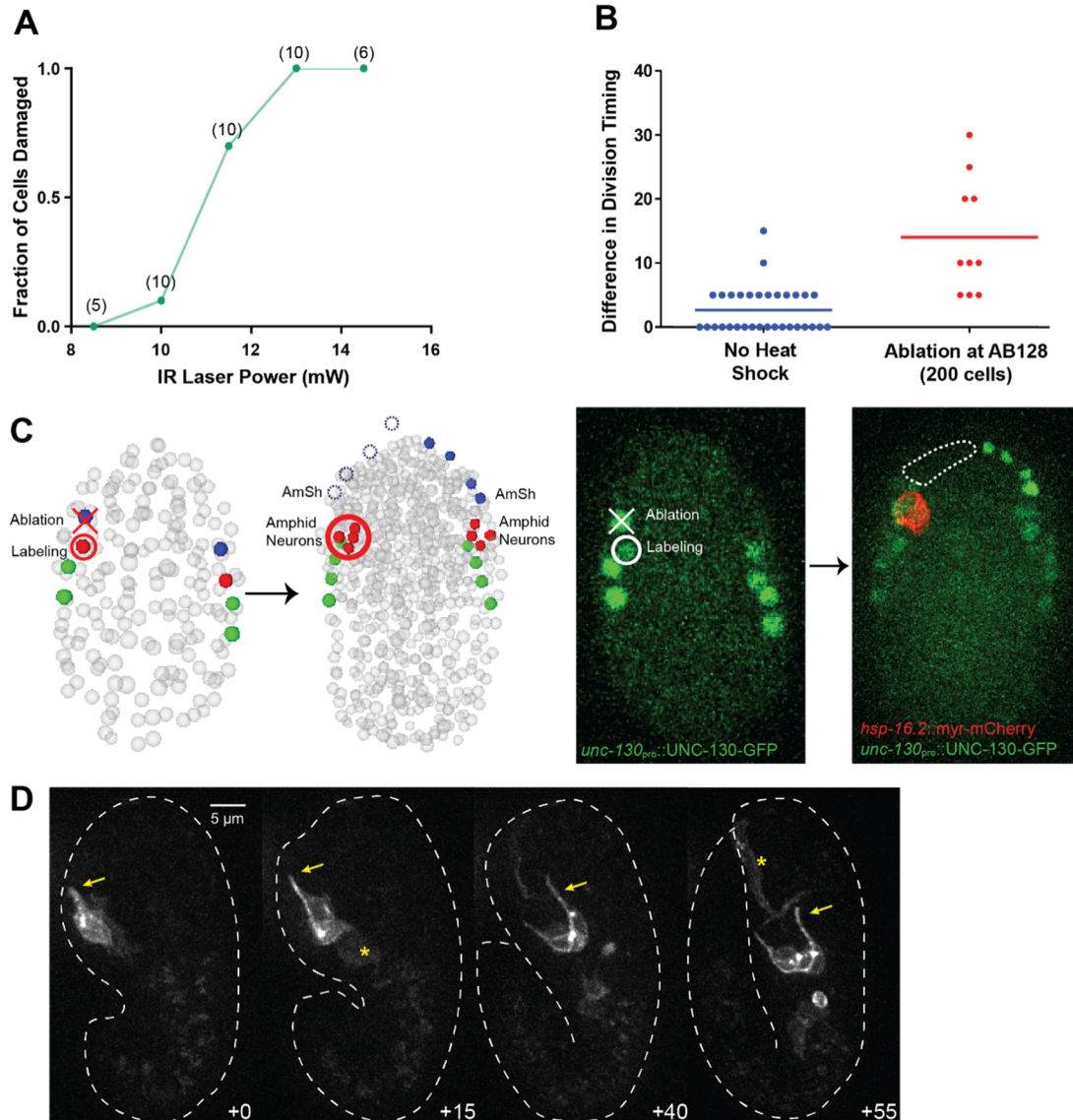


**Figure 6.2: Simultaneous Ablation and Labeling With the IR Laser Reveals AMsh Glia Role in Dendrite Extension.**

(A) Damage response curve at 6 Hz, 5% Duty Cycle, 10 seconds. Cells are scored as damaged if cells fail to complete the final division. Number of animals shown in the upper margin.

(B) Delay in division timing in amphid precursors due to ablation of amphid sheath.

(C) Left: Schematic illustrating cell ablation and labeling strategy. Right: Image showing the absence of the AmSh and sister cells after ablation and labeling of the amphid neurons (red)

(D) Time-lapse imaging of amphid neurons after amphid sheath ablation. Note that the dendrite begins to extend but then fails to remain anchored during cell body migration. Asterisk indicates nonspecific labeling from heat shock.

final cell division in neighboring UNC-130-labeled amphid neuron precursors is only modestly affected (14 min average delay; Figure 6.2B), suggesting that our conditions specifically damage the target cell without affecting surrounding cells. After ablation of the target cell, we sometimes observed heat-shock mediated labeling of neighboring cells, probably due to incomplete heat dissipation. Further optimization of the ablation parameters, by decreasing the pulse width, could create a more localized heat distribution.

We ablated the precursor of the amphid sheath and labeled the precursor of the amphid neurons using our standard induction parameters (Figure 6.2C). In 3/6 embryos in which the grandmother of the amphid sheath was ablated, the amphid neurons appeared to initially form a dendritic protrusion, but this was not anchored and was dragged posteriorly as the cell migrated (Figure 6.2D). This result suggests that the amphid sheath is important for providing an initial anchor in sensory dendrites.

This observation reveals that AMsh glia contribute to dendrite anchoring. Interestingly, the developmental progression of sensory dendrites in amphid sheath-ablated embryos closely resembles mutants that fail to express DYF-7 or DEX-1, extracellular matrix proteins expressed in neurons and the surrounding epithelia, respectively, that form a tether between dendrites and the nosetip<sup>69</sup>. Thus, glial proteins may also contribute to the dendritic anchor.

Importantly, postembryonic visualization of defects, as was performed in Yoshimura et al., after glial ablation does not reveal the origin of the defect. Two different mechanisms can explain how shortened dendrites are formed: sheath glia may either provide the initial anchoring during dendrite extension, or stabilize the neuronal

attachment after it has formed, preventing dendrite detachment during embryo elongation and larval growth. By allowing tracking of cells and ablation simultaneously, our system discriminates between these mechanisms.

## **Discussion**

In this section, I describe applications of IR induction that greatly increase the versatility of the tool. By expressing any gene of interest, rather than a fluorescent reporter, IR induction can be used to explore the temporal and spatial requirements of gene function. We demonstrate this application by showing that *daf-6* is required solely in the amphid sheath for proper amphid compartment formation during embryogenesis.

During the course of these studies, I also attempted to rescue *dyf-7* mutants by heat-shock driven expression of *dyf-7* cDNA in a subset of amphid neurons; as DYF-7 has been shown to be an extracellular matrix protein, I was interested in determining whether expression of DYF-7 from a subset of amphid neurons could rescue the defect in the entire bundle, thereby demonstrating a non-autonomous rescue. Despite achieving rescue with whole-embryo heat shock, laser-induced expression did not show rescue, suggesting that the amount of DYF-7 protein generated by expression in a small set of cells may be limiting. As described above, creating constitutive expression using the Cre-lox system may mitigate this problem, by increasing the level of protein expressed.

We also demonstrate the use of this system for simultaneous ablation and labeling of cells, and reveal a role for the amphid sheath in dendrite anchoring. This method can be immediately applied to many studies, without the need for generating new transgenic lines. In particular, recent studies in our lab have demonstrated a role for the CEPsh glial

cells in directing axon guidance within the nerve ring<sup>29</sup>. Recapitulating these experiments in the embryo and visualizing the origin of the defects in axons could lead to additional insights into how glial cells direct neurite growth.

## Chapter 7 Discussion

### Overview

A major challenge in studying neurodevelopment *in vivo* in *C. elegans* is that most embryonic reporters are expressed widely, preventing resolution of neurites that fasciculate into common structures, like the ventral cord, commissures, and the brain-like nerve ring. Though both the embryonic lineage of *C. elegans* has been delineated and the final structure of the nervous system has been mapped at high resolution over thirty years ago, this technical challenge and others (described below and in Chapter 1) have limited progress in learning about developmental events between neuron birth and neural circuit incorporation.

Here I present a technique for visualizing neural circuit development and manipulating the cellular context of growth *in vivo* in the *C. elegans* embryo. Our method, which uses an IR laser to heat single embryonic cells, is versatile and can be used to label neurons for tracking development, to drive gene expression, and to ablate cells. During this study, we characterize approximately 7% of the cells in the embryo, and reveal many biological phenomena that were not previously reported. For example, we provide evidence that a timing/competence mechanism controls axon-outgrowth dynamics in the nerve ring; we demonstrate that the DAF-6 protein functions in the amphid sheath glia to regulate sensory-organ formation; and we show that the amphid sheath glia are required for dendrite anchoring during retrograde extension.

In this section, I first describe limitations of our system and possible improvements. Next, as my studies have focused primarily on the amphid neurons, I

discuss how the system could be used to more fully characterize the development of the amphid commissure. An important future direction is the integration of our IR system with other tools (automated lineage analysis, SPIM microscopy) to allow for comprehensive cataloging of nerve ring development in *C. elegans*; I discuss considerations for integrating IR-mediated gene induction with these existing tools.

## **7.1 Limitations and Improvements to IR Labeling**

### **7.1.1 Achieving Single-cell labeling**

The main limitation of our system is that it does not provide single-cell resolution. The number of cells labeled is dictated by the kinetics of heat shock induction and subsequent fluorescent protein maturation. For labeling cells with membrane-tagged mCherry, induction must occur in the grandmother of the desired cells, such that ~4 cells are labeled in each embryo. Since many neurons in *C. elegans* fasciculate into common structures, this prevents visualization of single-cell growth.

New, faster maturing, and brighter fluorescent proteins may allow heat shock induction at later stages, reducing the number of cells labeled in each embryo. As I describe in Chapter 1, a major advantage of red fluorescent proteins (vs. green) is the 5-10 fold lower phototoxicity from imaging, thereby allowing much higher quality imaging. An improved red fluorescent protein with similar spectral properties to mCherry has recently been developed, named mKate2<sup>114</sup>. Literature indicates that the protein has half the maturation time of mCherry, is 1.5-2 fold brighter, and is less prone to aggregation. A systematic characterization of newer fluorescent protein variants using the

strategy described (measuring kinetics, brightness, as in Figure 2.1) could allow induction at later stages, and thus, more fine-scale resolution.

Another solution is to utilize recombinase-based strategies with promoters that express in a wide but more restricted set of cells in order to reduce the number of cells in which expression occurs. For example, the *dyf-7* promoter is expressed in all sensory neurons and begins expression at early morphogenesis. In some sublineages (for example, those containing AWC or ASH), there is only one sensory neuron generated by inducing a precursor cell. Thus, by using a heat-shock driven Cre-lox system with the restrictive promoter driving expression, labeling will occur only in that neuron. During the course of our studies, other widely-expressing, early promoters like *dyf-7* were characterized in the embryo in our lab and others, for example *lim-4* for the sublateral neurons<sup>115</sup> and *mir-228* for glia (Rapti et al., submitted), which could be used for such a strategy. Importantly, these reporters are differentially expressed in sister cells, unlike the reporters described in Chapter 3, Table 2, which are lineage-specific. Early in our studies, we attempted to identify an early pan-neuronal promoter, but commonly used reporters (*rab-3*, *unc-119*, *unc-33*) were either not expressed early enough or appeared to be non-specific.

### **7.1.2 Reliance on the Heat Shock Response**

Another limitation of our system is the reliance on the heat shock response, which can alter cell physiology. As this was a major concern, we compared axon growth (Figure 3.5) and hypodermal migration and fusion (not shown) in cells labeled by promoters and by IR induction and did not observe any differences. There were, however, delays in division timing (maximum 40 min) of the heat-shocked precursor cells in the final round

of divisions. The fact that axon outgrowth is not delayed indicates that cell birth time does not determine the timing of morphogenesis of cells, and validates the use of our system to study axon outgrowth.

In theory, the most concerning aspect of the division delay is that the time between cell birth and normal axon outgrowth may be shorter than 40 min for very early nerve ring growth; as the cells may not even be generated by appropriate time, they cannot grow out axons on time. As the amount of heat shock delay appears to be variable (Figure 3.5), one solution is to induce the same cell several times and keep track of the amount of division delay by comparison to the left-right homolog cells. Given that the studies here suggest that the outgrowth timing of cells is stereotyped in *C. elegans*, large differences in outgrowth timing may be a sign of cell damage. Alternatively, data could be used only from cells which are delayed <15 min, which is within the limits of natural variation.

Lowering the heat shock threshold may lessen these delays. Cultivation at colder temperatures has been shown to reduce the heat shock threshold<sup>116</sup>. Increasing the available pool of heat shock factor, by HSF1 overexpression, may allow lower temperature heat shocks to produce the same downstream activation effect. Another possibility is to amplify the signal downstream of heat shock, e.g. through a feed-forward transcriptional loop, thereby creating a highly sensitive switch that is responsive to very low heat shock levels. Early in our studies we attempted to create such a system using the Q-binary system (described in Chapter 1), but were unable to create a sustained response and did not test the system further.



### 7.1.3 Improvements to Optical Setup

Our IR microscope setup is simple and can be easily integrated with a commercial widefield microscope. A few improvements to the setup would increase the ease of use. During the course of 5-minute inductions, the cell often moves from the focus, from short-range shuffling of cells and Brownian motion. This requires the user to manually shift the stage to maintain the focus, which is difficult due to instability of the stage and also greatly increases technical variation. Adding an automated stage with a simple point-and-click mechanism of re-centering based on the location of a camera image would probably increase the efficiency of induction. Alternatively, the beam could be moved with a motorized mirror to compensate for cell movement.

IR gene induction experiments are likely to benefit from a system that can induce multiple cells at once, as *C. elegans* cells are often bilaterally or four-fold symmetric and are generated from different precursor cells. Although it is possible to induce cells serially, there is a limit to how many cells can be induced in a single cell cycle at the AB128 stage (probably 4-5). Parallelization could be achieved by splitting the laser and focusing the microbeams simultaneously through the objective into separate spots on the imaging plane.

## 7.2 Further Characterization of the Amphid Commissure

The amphid commissure is a promising system to study how cell-cell interactions, guidance cues, and cell-intrinsic developmental programs lead to formation of the final structure. In addition to the limited size of the commissure, limited evidence suggests that there may be a pioneer neuron in the commissure, which guides the growth of follower neurons. This model has been proposed based on the fact that guidance mutants of the

amphid commissure have “all-or-nothing” defects, where the entire commissure exhibits the same trajectory<sup>103,107</sup>. The commissure also has a characteristic anterior-posterior ordering of axons, which suggests that fasciculation between neighbors may be important for growth.

Our IR system offers a number of tools to dissect the mechanisms of how this structure forms. First, labeling can be used to determine the order of growth into the commissure. We provide a very preliminary characterization in Chapter 5, but as we describe above, labeling can be limited to only sensory neurons with the Cre-lox system, thereby greatly improving cellular-resolution. The role of a “pioneer neuron” for the amphid can be tested by cell-specific rescues of *vab-1*, which we show in Chapter 5, causes lateral entry into the nerve ring and has previously been shown to affect the entire commissure<sup>103</sup>. If, for example, *vab-1* expression in a single neuron rescues the defect in the entire commissure, then the neuron is likely to be a pioneer cell. It is also possible that defects can be rescued cell-autonomously, which would indicate that cells have the ability to navigate to the target independently of each other. The existence of cell-cell dependencies can also be tested by ablating precursors of amphid neurons and labeling other amphid neurons to see if growth trajectories or dynamics are altered in the absence of fasciculating partners (as shown in Chapter 6 for the amphid sheath). Cells that grow next to each other in the commissure are likely to be good candidates for this study.

### **7.3 Tools for Comprehensive Characterization of Nerve Ring Development in *C. elegans***

IR labeling offers an opportunity to characterize the development of the nervous system in *C. elegans* systematically and at high resolution. Additional tools, which address

challenges in precursor cell identification and imaging at higher temporal resolution, will be essential for future studies.

### **7.3.1 Automated Lineage Tools**

Our studies were facilitated by the use of lineage-specific markers (e.g. *unc-130*), which allowed identification of specific precursor cells without lineage tracing. However, this strategy may not be applicable to all cells in the embryo, as it requires multiple such markers which are not likely to cover any cell of interest (described in Chapter 3, Table 2). We envision that our tool could be combined with implementations of automated and semi-automated lineaging software<sup>31,37</sup> to allow access to the entirety of *C. elegans* embryogenesis, with minimal manual labor. Recent improvements in computer algorithms can identify cell divisions and track nuclei in *C. elegans* embryos in “real-time” (P. Shah, Z. Bao, personal communication)<sup>34,35</sup>. A strategy combining these techniques would work as follows: (1) lineage analysis with software and manual curation would be performed on embryos from the 4-cell stage to the ~200 cell stage using pan-nuclear GFP markers (2) IR labeling or perturbation would be induced in a pre-defined cell of interest automatically, by feeding the appropriate nuclear coordinates to the IR laser alignment system (3) the neurites of the desired subset of cells could be visualized using mCherry fluorescence time-lapse imaging at the start of morphogenesis and simultaneous GFP nuclear imaging with cell tracking would provide cell position data for all other cells in the embryo.

Matching the induction time of heat shock to the time-resolution required for automated lineage-tracing will be important for integration of these tools. Currently, tracking nuclei between time points requires that volumes are taken every ~2 minutes,

while our heat shock induction protocol requires 5 minute inductions. It is not clear whether cell-tracking can perform with high fidelity over that time gap. Performing power response curves and axon outgrowth controls in labeled cells after shorter induction periods will determine whether it is feasible to reduce the induction time. Similarly, attempts to parallelize this tool (lineaging and inducing multiple embryos during the same session) will benefit from shorter induction times.

### **7.3.2 Improved Imaging Techniques**

Image quality of IR-labeled embryos could be improved by using new methods of microscopy, like selective plane illumination (SPIM) or structured illumination, which are specifically suited to imaging live-tissues without photo-toxicity and at rapid rates. The time resolution and signal-to-noise ratio of our datasets was limited by the use of confocal microscopy. For example, although we were able to see axon forking and retraction in *sax-3* mutants, we could not follow the behavior of single branches with five-minute time resolution. Also, our measurements of axon outgrowth were less reliable after the onset of twitching. In principle, SPIM microscopy can image full volumes of the embryo at ~30x the speed of confocal microscopy, and also create blur-free imaging in the post-twitching phase of development, surmounting these problems.

A SPIM microscope was built by Peter Insley in our lab for imaging embryos during the course of these studies. Due to differences in mounting procedures, we were unable to move labeled embryos from traditional slide mounts into the immersion chamber required for SPIM microscopy. We constructed an optical path to merge the IR beam into the SPIM microscope, with the hope of creating a single microscope for lineaging, induction, and imaging of labeled cells. As I describe in Appendix C, we

encountered difficulties with co-alignment of the induction objective with the imaging objectives. More recently, we have constructed a mount separately compatible with both microscopes, and studies are currently underway to image IR-labeled cells using SPIM.

### **7.3.3 Registration Strategies for Embryo-Embryo Comparison**

As our strategy labels small sets of independent cells in individual embryos, a remaining challenge is how to combine and compare spatial and temporal data about neurite growth from different embryos. Such a comparison is crucial to determine, for example, if specific cells labeled in separate experiments make contact with each other during growth or to rigorously compare outgrowth timing. In our comparisons, we use a simple method of temporal alignment based on the overall morphology of the embryo to plot axon growth over time, but we do not attempt to compare spatial localization of neurites or cell bodies between wildtype or mutant embryos.

Recently, a method using the lattice of hypodermal cells has been used to untwist the embryo during elongation, allowing such a comparison of CAN, ALA, and AIY neurons between different embryos and also late into twitching <sup>40</sup>. This strategy uses two alignment markers as a set of fiduciary points – the seam cells markers, which mark a bilaterally symmetric set of 22 nuclei, and a membrane marker labeling hypodermal boundaries. The seam cell markers can be identified automatically through software, whereas the membrane marker requires manual annotation. Adding these alignment markers to our labeling strains and using the established pipeline would allow us to perform these comparisons. However, as the authors note, editing 100-150 timepoints for one embryo requires approximately 8 hours of manual labor.

Although a major advantage of this approach is that it permits alignment of embryos after twitching, our preliminary imaging of axon growth suggests that much of central nervous system development may actually happen prior to twitching. Thus, simpler methods using rigid registration with sparse nuclear markers may be sufficient for generating composite datasets (Insley et al., unpublished). Currently, this alternate pipeline uses the *unc-130* marker for registration between embryos; one advantage of this strategy is that it allows comparisons between embryos early in development since the fiduciary marker is expressed early, permitting tracing of precursor cells or early migrations. Moreover, the system for alignment is entirely automated.

### **Summary**

*C. elegans* is an attractive system to study *in vivo* neurodevelopment, due to its limited size, stereotypical development, and extensive knowledge base. In this work, I present a general and simple method using an IR laser to track and manipulate single neurons and glial cells in the embryo. As we demonstrate, this method is versatile and can be used for directed cell labeling, gene induction, and ablation. Alongside light-efficient imaging technology and software-automated cell identification, we envision that IR laser induction is a parallel tool allowing for high-resolution, systematic analyses of development and also increasing the experimental accessibility of the *C. elegans* embryo. Moreover, given that heat-shock thresholds are similar across organisms, we expect that our induction conditions and strategy for optimization could be adapted readily to other transparent embryos including *Xenopus*, *Drosophila*, and zebrafish.

## **Chapter 8 Materials and Methods**

### **Strains and Plasmids**

Animals were cultured on NGM agar seeded with OP50 bacteria at 20°C using standard methods<sup>117,118</sup>. Transgenes/plasmids are listed further below.

### **Temperature Calibration for Heat Shock Induction and Embryo Viability**

Embryos were dissected from hermaphrodites and allowed to develop for ~2 hours in M9. Embryos were then transferred into PCR tubes and heat shocked for 5 minutes using a temperature gradient program on a Thermocycler with 2°C intervals. Embryos were subsequently recovered and either mounted on agar pads for scoring heat shock induction by myr-GFP, or placed on plates and scored for hatching after 24 hours.

### **Kinetics of Fluorescent Protein Induction**

Embryos were mounted on slides using 20-µm bead spacers, as above. The slides were then put in a thin-bottomed plastic container and placed in a water bath at 33°C for 5 min. After heat shock, slides were imaged using spinning-disk confocal microscopy at 5 min intervals (see Imaging Procedures), and the time from the heat shock was recorded. The total fluorescence was quantified in a single slice over time for 4-6 embryos per transgene and then averaged in every time point to generate the kinetics curves. As the images were taken at different power levels depending on the laser line, the resulting fluorescence intensities were normalized by the applied laser power to create a comparison, which should be affected only by protein levels and quantum efficiency between the different fluorescent proteins.

## **Microscopy for Measuring Heat Shock Kinetics and Imaging Embryos for Tracking Morphogenesis**

Time-lapse images were acquired on the CellVoyager 1000 (Yokogawa/Olympus) spinning-disk confocal microscope, using a 1.35 NA 100x Olympus silicone oil-immersion objective (UPLSAPO 100XS). Z-stacks of 25-30 slices at 0.8-1  $\mu\text{m}$  spacing were acquired every 5 min with 200 ms exposures/slice. Laser-power levels passing through the objective were measured at 20  $\mu\text{W}$  on the 488 laser (GFP) and 100  $\mu\text{W}$  on the 561 laser (mCherry). After twitching, the exposure time was decreased to 40 ms to decrease motion blur, and mCherry laser power was increased to 500  $\mu\text{W}$ . Temperature varied between 21°C-24°C during acquisition, a major cause of developmental timing variation during morphogenesis.

## **Optical Design for IR Induction, Ablation, and Temperature Measurements**

A 1455-nm continuous wave infrared laser (RLR-2-1455, IPG Photonics Corp.) was coupled to a wide-field fluorescent microscope (Zeiss AxioImager A1). After 4x beam expansion, the beam was directed into a side port and a shortpass dichroic (T860spxrt\_1500, Chroma Tech.) was used to merge the epifluorescent light path, first filtered with a dual excitation filter (59022x, Chroma Tech.), and the IR laser beam. A dual dichroic (59022bs, Chroma Tech.) along with single-wavelength emission filters (GFP, XF3080; mCherry, XF3081 Omega Optical) was used for imaging GFP/mCherry simultaneously with IR induction. An additional shortpass filter (FESH1000, ThorLabs) was used to protect the camera and eyepiece from small amounts of IR irradiation. IR Induction experiments and temperature measurements were performed using a Zeiss oil



immersion objective, 1.3 NA (1018-595). A signal generator (BK Precision, 4054) was connected to the external interface of the laser to control the duration and frequency of pulses for ablation and for synchronizing the camera frame acquisition with the laser induction for temperature measurements. Fluorescence images for temperature measurement were acquired using a CoolSNAP HQ2 CCD camera (Photometrics). A temperable ring (Pecon, 0269-010) was fastened to the objective, and connected to a circulating water bath (VWR scientific) with heating and cooling control, for sample temperature control. Pictures of the optical setup can be found in Figure 2.5.

### **Laser Alignment**

To identify the focus of the laser, we found that the infrared laser could be detected at high exposure times (~1 second) on the CCD camera, and this was used for x-y alignment. The z-alignment could not be determined using this method, so we used optical trapping of 3- $\mu$ m polystyrene beads (Polysciences, Inc) during the initial alignment procedure. As the z-focus of the laser is dependent only on the distance between the lenses of the beam expander, this alignment was only performed initially, while the x-y alignment was verified on the camera prior to starting every experiment.

### **Embryo Mounting and Recovery**

For IR labeling and ablation experiments, embryos were dissected from hermaphrodites and transferred by mouth pipette onto glass slides with M9 and 20- $\mu$ m polystyrene beads as slide spacers, as previously described<sup>119</sup>. This places embryos under slight compression and aligns the dorsal-ventral axis to the Z-imaging axis prior to

morphogenesis, and the left-right axis to the Z-imaging axis during elongation (see Figure 3.2 for details). Slides were sealed to prevent evaporation using vaseline heated to 40°C. Vaseline cools quickly on the slide and does not induce the heat shock response, unlike commonly-used Valap which requires higher melting temperatures and prolonged cooling time. For scoring *daf-6* gene rescue and verifying AWA morphology post-embryonically, embryos were induced on 2% agarose pads to facilitate recovery. Approximately 2 hours after heat-shock induction, embryos were transferred to agar plates with a wire pick. Embryos were allowed to hatch on plates and grow until L3 or L4 before scoring.

### **Background Cooling and Measurement of mCherry Temperature Dependence**

For background cooling during induction experiments and for mCherry temperature calibration curves, the temperature of the sample was controlled by heating and cooling the immersion objective. We found this to be an effective method of controlling the sample temperature due to the close contact between the objective and sample. A temperable ring (Pecon, 0269-010) was fastened to the objective, and connected to a circulating water bath (VWR scientific) with heating and cooling control. To confirm that the sample temperature matched the water bath, a thermocouple (Physitemp) was inserted directly into the sample and compared. For water bath temperatures ranging from 15°C-40°C, the sample was within <1.5°C of the water bath temperature. For calibrating mCherry fluorescence, the water bath temperature was changed between 15°C and 40°C and images were captured of a single cell expressing mCherry in anesthetized larval animals (*ceh-27<sub>pro</sub>::mCherry*, expressed only in 4-6 neurons postembryonically). We

noted that the z-focus changed during temperature changes due to expansion/contraction of the objective, and appropriate compensations were made to keep the cell in focus. The total fluorescence of the cell was measured after background subtraction by summing a region of interest circumscribing the entire cell in ImageJ, and the fluorescence was plotted at different temperatures, normalized to the 20°C value. Some temperatures measurements were revisited for each sample after temperature alterations in order to confirm reversibility of the fluorescence change.

### **Temperature Measurements**

For *in vitro* temperature measurements, the laser was focused at the center of a bacterium-expressing GFP, and fluorescence images were acquired one second after the laser was turned on and one second after the laser was turned off. To generate a temperature heat map, the two images were divided pixel by pixel. To calculate the temperature at the focus, total bacterium fluorescence after background subtraction was measured in both laser ON and laser OFF images and the ratiometric decrease in fluorescence was converted to temperature elevation using the temperature sensitivity measured.

For *in vivo* temperature measurements, the laser was focused at the center of an AB128 mCherry-expressing cell, and fluorescence images were acquired one second after the laser was turned on and one second after the laser was turned off. To generate temperature maps, the two images were down-sampled by 3x to reduce noise, and background subtracted. Processed images were divided (Laser ON image/laser OFF image), and ratiometric fluorescence decrease was converted to temperature increase

based on the measured mCherry temperature sensitivity. Heat map was rendered using MATLAB.

To measure temperature elevation at the focus and in neighboring cells, total cell fluorescence was quantified in the laser ON/OFF images after background subtraction using ImageJ, and resulting values converted to temperature elevation as above. To plot spatial distribution, distances between the center of the cell of interest and the focus of the laser were measured. Data from multiple embryos (n=3-5 per power setting/reporter) was aggregated, and independent temperature measurements from cells within 2  $\mu\text{m}$  were averaged. Error bars represent standard deviation.

### **Induction and Scoring of Embryos for Labeling and Ablation**

Embryos were mounted using 20  $\mu\text{m}$  bead spacers. During heat-shock induction, the cell was irradiated for 5 continuous minutes. To determine power vs. response curve, precursor cells were identified using a nuclear UNC-130-GFP marker. A marked cell (ABpl/raapaa or ABpl/raapap at AB128, ABpl/raapa at AB64) was induced for 5 minutes in different embryos at various powers. After 150 minutes, heat-shock driven mCherry induction in progeny cells was scored. If 4 cells were labeled and the signal colocalized with UNC-130-GFP, induction was scored as specific. If additional cells (usually also 4 additional cells, not colocalizing with GFP) were labeled, embryos were scored as having off-target induction.

For ablation experiments, the AMsh-glia precursor was identified (ABpl/raapaa) by UNC-130-GFP at AB128. The cell was irradiated and scored as ablated if it failed to divide to the final round 200 min after induction.

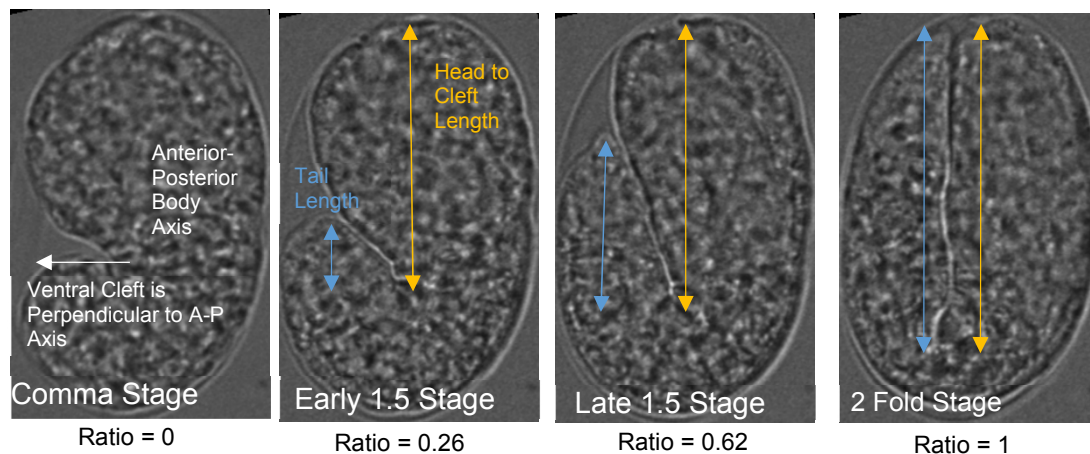
### **Axon-Outgrowth Measurement**

Neurite length was quantified in ImageJ by marking a set of points along the axon and summing the Euclidean distance between these. The distance between neighboring points  $(X,Y,Z) \rightarrow (X', Y', Z')$  was calculated by  $D_{3D} = [(D_{X-X'}^2 + D_{Y-Y'}^2 + D_{Z-Z'}^2)]^{1/2}$ . This distance was plotted as a function of developmental stage (tail-to-head length; see below) to facilitate comparison between embryos. The tail-to-head ratio ranges from 0 (comma stage) to 1 (2-fold stage). Note that after twitching begins (tail-to-head=0.5-0.6), some timepoints were omitted if the axon was not visible.

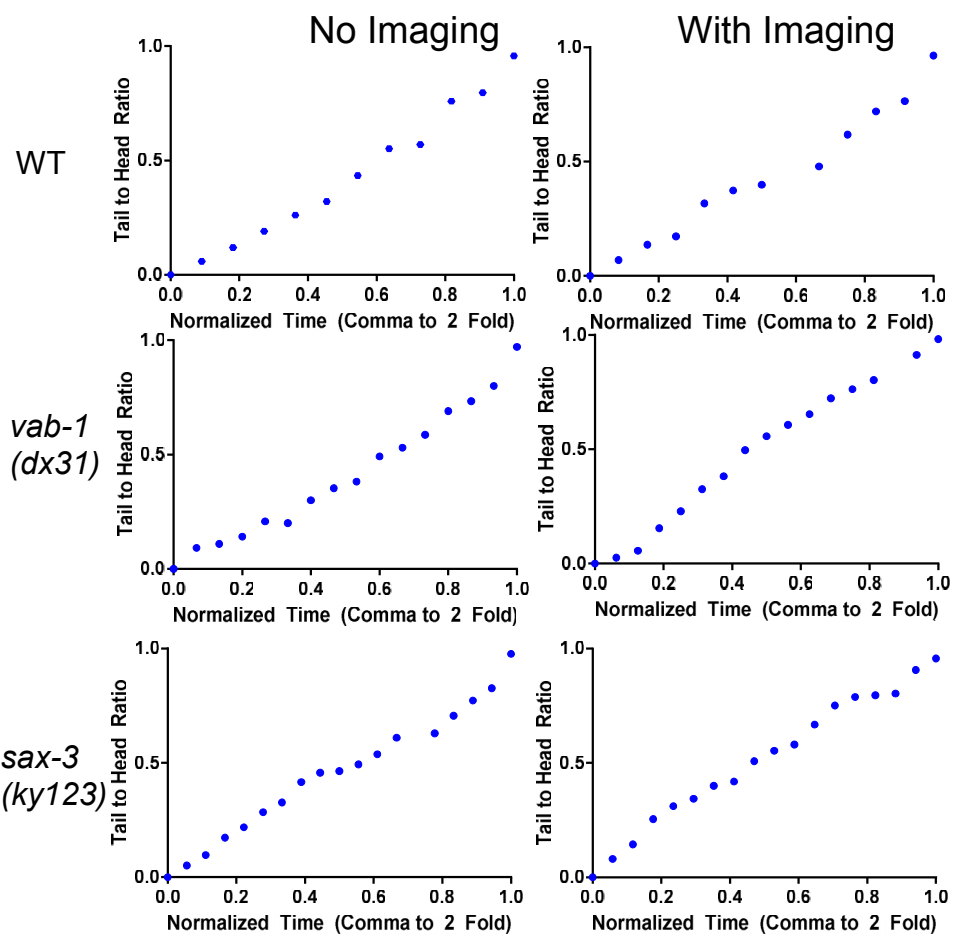
**Figure 8.1. Tail-to-Head Ratio Is Used as a Proxy for Developmental Stage, (A)**

Calculating Tail-to-Head Ratio. Comma stage occurs when the ventral cleft is perpendicular to the anterior-posterior embryo axis <sup>33</sup>. At 2-fold, the tail overlaps entirely with the head. (B) Tail-to-head ratios plotted against normalized time in imaged and non-imaged, wild-type and mutant embryos. Normalized time calculated by setting comma stage to 0 and 2-fold stage to 1. After twitching (Ratio = 0.5-0.6), the tail occasionally retracts, and values for these are omitted. Without imaging, ratio curves steepen over time. With fluorescence imaging, mutants, unlike wild-type embryos, sometimes show flattening of the curve towards time course end, suggesting phototoxic developmental slowdown. To overcome this, Tail-to-Head Ratio was used to mark developmental time rather than absolute or normalized time. (C) Average duration (SD) from comma to 2-fold (n=6 embryos/condition).

A



B



C

	Avg, STD (min)	
	No Imaging	With Imaging
Wildtype	58.6 (6.83)	70.8 (8.6)
<i>vab-1</i> ( <i>dx31</i> )	73.3 (5.1)	82.1 (13.2)
<i>sax-3</i> ( <i>ky123</i> )	81.6 (11.7)	85.8 (13.9)

### Dye-Filling Assays

Embryos were recovered after laser irradiation, grown until the L4 stage, and placed singly in drops of M9 + 5 µg/ml DiI for 30 min (Perens et al., 2005). Animals were recovered onto plates and imaged with wide-field microscopy.

### 3D Renderings of Embryogenesis

Nuclear coordinates were taken from a fully-lineaged embryo (Richards et al., 2013) at 202 min (AB128) and 357 min (early morphogenesis), and 3D models with colored sublineages were rendered in MATLAB.

### Strains and Transgenes

Transgenes Used in this Study:

Transgene	Constructs
<i>nsIs520</i>	pANU01( <i>hsp-16.2::Cre</i> recombinase) + pEKL15( <i>lin-15(+)</i> )
<i>nsIs515</i>	pANU13( <i>his-72</i> <sub>pro</sub> ::lox-STOP-lox::myr-GFP) + pRF4( <i>rol-6</i> ).
<i>nsIs420</i>	pANU21( <i>hsp-16.2::myr-GFP</i> ) + pEKL15( <i>lin-15(+)</i> )
<i>nsIs427</i>	pANU43( <i>hsp-16.2::myr-mCherry</i> ) + pEKL15( <i>lin-15(+)</i> )
<i>wgIs76</i>	<i>unc-130::TY1::eGFP::3xFLAG</i>
<i>kyIs37</i>	<i>odr-10</i> <sub>pro</sub> ::GFP
<i>oyIs45</i>	<i>odr-1</i> <sub>pro</sub> ::YFP
<i>nsEx5290</i>	pANU84( <i>ceh-27</i> <sub>pro</sub> ::GFP) + pANU85( <i>ceh-27</i> <sub>pro</sub> :: <i>mCherry</i> ) + pEKL15( <i>lin-15(+)</i> )



<i>nsEx5291</i>	pANU107( <i>unc-130</i> <sub>pro</sub> (5.5kb)::UNC-130-GFP) + pANU110( <i>unc-130</i> <sub>pro</sub> (5.5kb)::UNC-130-mCherry)
<i>nsEx5292</i>	pEP7( <i>hsp-16.2::daf-6</i> ) + pANU107( <i>unc-130</i> <sub>pro</sub> (5.5kb)::UNC-130-GFP) + pRF4( <i>rol-6</i> )
<i>nsEx5065</i>	pANU134( <i>unc-130</i> <sub>pro</sub> (5.5kb)::UNC-130::STOP::SL2::Cre) + pANU53( <i>dyf-7</i> <sub>pro</sub> ::lox-STOP-lox::myr-GFP) + pEKL15( <i>lin-15</i> (+))

#### Mutant Alleles Used in this Study:

*vab-1(dx31)* II

*sax-3(ky123)* X

*daf-6(e1377)* X

*lin-15(n765ts)* X

#### Plasmids Constructed/Used in this Study:

pANU01	<i>hsp-16.2::Cre</i>	<i>hsp-16.2</i> was digested from pPD49.78 (gift from A. Fire) and inserted into pEM3 = <i>ncs-1</i> <sub>pro</sub> ::Cre (gift from C. Bargmann, from <sup>53</sup> using SphI/XmaI sites
pANU21	<i>hsp-16.2::myr-GFP</i>	<i>hsp-16.2</i> was digested from pPD49.78 (gift from A. Fire) and inserted into pMH29 <sup>69</sup> using SphI/XmaI sites
pANU43	<i>hsp-16.2::myr-mCherry</i>	Myristylation sequence MGSCIGK inserted at N-terminus of mCherry <sup>120</sup>

		myr-mCherry was cloned into pANU21 using AgeI/EcoRI sites
pANU13	<i>his-72</i> <sub>pro::lox-</sub> STOP-lox::myr- GFP	A 1kb <i>his-72</i> promoter <sup>121</sup> was amplified from genomic DNA using oligos 5' aaccCTGCAGaaacgttatagtgtggacaccaattt and 3' aaccCCCGGGtggtgttctggaaattgagaattga and cloned into pMH29 (Heiman and Shaham, 2009) using PstI/XmaI sites  loxP- <i>LacZ</i> STOP -loxP was amplified from pEM1 using oligos  5' aaccCCCGGGcaggaggacccttgctagcgataa 3' aaccACCGGTgataacttcgtataatgtatgctat  and cloned into vector from above using SmaI/AgeI sites
pANU53	<i>dyf-7</i> <sub>pro::lox-</sub> STOP-lox::myr- GFP	lox-STOP-lox was amplified from pEM1(gift of C. Bargmann, from <sup>53</sup> using oligos  5' aaccGGATCCcaggaggacccttgctagcgataa 3' aaccCCCGGGgataacttcgtataatgtatgctat  and cloned into pMH29 (Heiman and Shaham, 2009) using BamHI and XmaI sites
pANU84	<i>ceh-27</i> <sub>pro::GFP</sub>	<i>ceh-27</i> <sub>pro</sub> (3.3 kb) was amplified using  5' aaccCTGCAGttcgtttgtttcactttctgagga

		3' aaccGGATCCtctacaaattaattgtagttaaggcgagaaactgg
pANU85	<i>ceh-27</i> <sub>pro</sub> ::mCherry	See pANU84
pANU107	<i>unc-130</i> (5.5kb) <sub>pro</sub> :: UNC-130-GFP	<i>unc-130</i> <sub>pro</sub> (5.5):: <i>unc-130</i> (CDS) without the last 15 amino acids was amplified from N2 genomic DNA using oligos  5' aaccCCTGCAGGaccgatcttgcgattcacttagtg 3' aaccCCCGGGgagctcgatgaagttcttctgg  cloned in frame into pPD95.75 using SbfI/XmaI
pANU110	<i>unc-130</i> (5.5kb) <sub>pro</sub> :: UNC-130-mCherry	see pANU107
pANU134	<i>unc-130</i> (5.5kb) <sub>pro</sub> ::UNC-130::STOP::SL2::Cre	<i>unc-130</i> <sub>pro</sub> (5.5):: <i>unc-130</i> (CDS)::STOP was amplified from N2 genomic DNA using  5' aaccCCTGCAGGaccgatcttgcgattcacttagtg 3' aaccCCCGGGgctagctcgatgaagttcttctgg  SL2-nCre was generated using fusion PCR  (used to drive Cre expression with regulation of <i>unc-130</i> from promoter and introns)
pEP7	<i>hsp-16.2</i> :: <i>daf-6</i>	108

## Appendix A: A Genetic Strategy for Sparse Labeling in the Embryo

**Introduction:** Initially, we considered an approach for sparse labeling in the embryo based on Brainbow-like strategies<sup>59</sup>. We simplified the Brainbow approach to use a single reporter, which is easily compatible with multi-copy transgenic arrays required for strong expression in *C. elegans*.

A schematic is shown in Figure A.1A. A short heat shock drives expression of Cre recombinase, causing excision of the STOP cassette after recombination, and allowing the fluorescent protein to be expressed constitutively. In order to achieve sparse labeling, the heat shock must be very slight, such that a random subset of cells in the embryo will express Cre in high enough amounts to cause the recombination event to occur. In non-labeled cells, this event does not occur.

We expressed the two constructs as two separate arrays to increase mosaicism, and subsequent sparseness of labeling. After significant optimization of heat shock induction conditions (optimally 36°C, 2 min in water bath), we were able to achieve labeling in small numbers of cells. (Figure A.1B,C)

**Results:** This approach has a number of drawbacks, listed below.

- With a strong heat shock (34°C for 5 min), Cre-lox recombination produces a signal within ~2 hours (shown in Figure 2.1). However, we found that, with a very slight heat shock, recombination takes longer (3-4 hours). This increased delay is due to either (1) the additional time required for Cre accumulation in order to produce a recombination event (2) the time it takes for the GFP signal to accumulate from very few recombination events. Thus if embryos are heat-shocked 3-4 hours before the bean stage, clonal

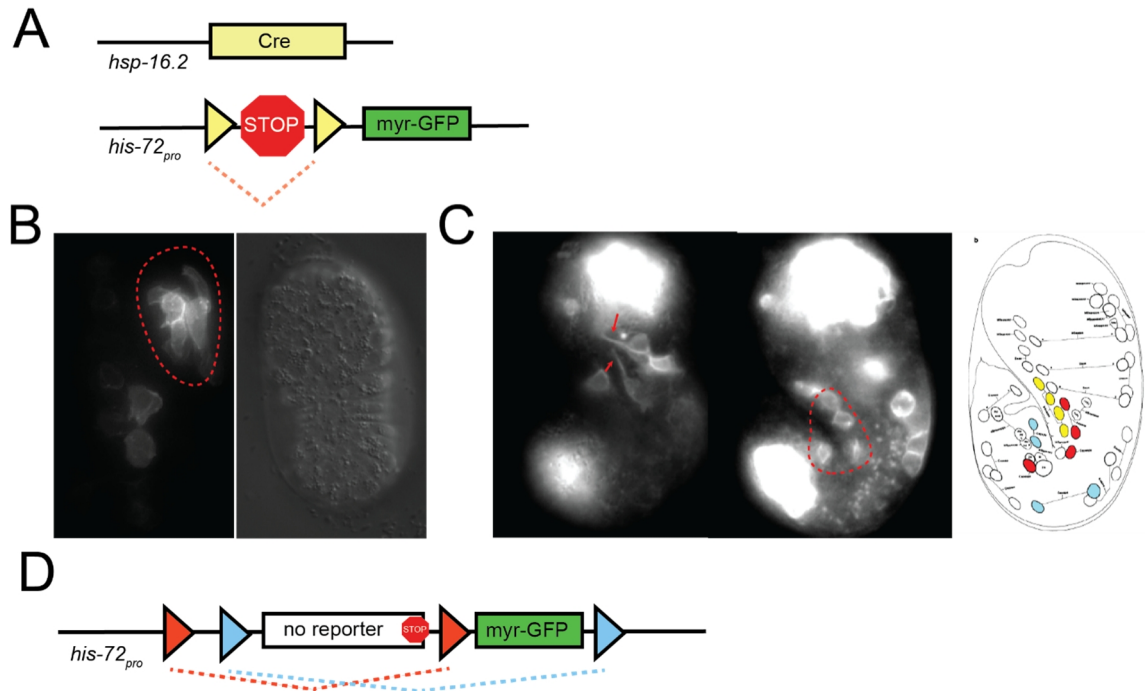
populations of labeled cells are quite large (Figure A.1B). For most of our experiments, we decided to induce at AB128-AB256 (~200-300 m.p.f.), leading to the signal being strong enough to visualize cells in the ~1.5 fold embryo. Even if clonal populations of cells could be identified at this stage, embryos did not show single cell/single sublineage labeling, rather many populations were visible (See Figure A.1C; two planes from the same embryo are shown). This level of sparse labeling does not in general provide cellular resolution of axon growth.

- Biases in the strength of the heat shock promoter across different cell-types can cause non-random labeling. The difference in thresholds for activation is clearly visible when embryos are heat shocked after the final division, with strongest expression in the gut and pharynx. In order to quantify this bias, we synchronized embryos, heat shocked them at ~250-300 min post fertilization, and then recovered L1s shortly after hatching (after which the *his-72* promoter starts to turn off). We scored the neuron-types labeled in each animal when the labeling was sparse enough to differentiate the trajectories of individual neurons. We categorized the different neuron types in *C. elegans* by morphology and then scored the frequency of each cell-type. As shown in Table 4, certain cell types (neurons with sublateral processes, motor neurons, and pharyngeal neurons) never appeared to be labeled. This suggests that this strategy would probably fail to label certain lineages of cells. Moreover, the identifications were not made on the level of single names, it is possible that even though we were able to observe a diversity of neuron classes, the same neurons were labeled repeatedly.

**Alternate Strategies for Genetic Sparse Labeling:** An alternate sparse labeling approach could overcome the first two drawbacks (slower kinetics and the lower

thresholds for activation in some cells), which we propose here. As shown in Figure A1.D, recombination after excision produces two mutually exclusive events – producing either ON or OFF labeling. It is important to note that this strategy requires the use of a single-copy reporter strain. The frequency of ON or OFF events can be set by the distance between the heterospecific lox sites (distance between red triangles vs. between blue triangles, shown in Figure A.1D), thereby determining the “sparseness” of labeling. With this strategy, a strong heat shock can be employed because a recombination event is desired in every cell, and the randomness is provided by the excision event. This strategy has been validated in one recent paper, where a similar strategy was performed in cell culture with recombination rates varying from 5-50% depending on the distance between the lox sites (0-12 kb).<sup>122</sup> We did not test this strategy during this work, but a similar idea is being used for producing asymmetric labels in the amphid sheath (I. Lee, personal communication).

A second strategy to increase the sparseness of labeling is to use a restricted promoter (e.g. *dyf-7*) which is expressed early in embryogenesis, but is not sufficiently sparse to be used for imaging cells directly. Using this promoter to drive expression, in combination with the genetic method to increase sparseness, could lead to single-cell labeling.



**Hi wt g'CB Genetic Sparse Labeling.** (A) Heat shock causes STOP excision in a subset of cells (B) Large clonal populations are labeled at the bean stage (red) (C) Left: Neurites of labeled cells. Axons often fasciculate (top arrow); Middle: Induction of muscle cells; note that the pattern of induction determines the labeled sublineage (red) (D) Diagram of 1.5 Fold stage. The red muscle sublineage is labeled in the middle panel; other sublineages (blue yellow) are shown for comparison (D) Alternate Genetic Labeling Strategy

**Table 4: Neuron Types Labeled after Genetic Sparse Labeling.** (n = 70 animals, 152 cells)

Neuron Type	Examples	Frequency of Labeling Seen (number of cells)
Amphid Sensory Neurons	AFD, AWC	13% (21)
Other Sensory Neurons	IL1, IL2, OLL, OLQ, (URA, URB, URX)	33% (51)
Amphid and Ring Interneurons	ADA, AIA RIP, RIR	29% (45)
Pharyngeal Neurons	M1-5, I1-I5, MCL, MI	0%
Ventral Cord Interneurons + Ring Interneurons with Sublateral Processes	AVB, AVE SAA, SAB	0%
Motor Neurons	DA, DB, DD	0%
Tail Neurons	PHA, PVT	15% (24)
Socket/Sheath Cells (no axons seen)	ILso, AMsh	7.2% (11)

## Appendix B: Identification of Cells in the Embryo without Lineage Tracing

**Introduction:** Existing methods of embryonic cell identification track nuclei divisions with automated software, using the invariant cell lineage of *C. elegans* to identify the cell fate<sup>31</sup>. This method requires tracking from the 4-cell stage. Here, I test the idea that the position of cells in the wildtype embryo may be stereotyped, and therefore it should be possible to identify all cells in later developmental stages in the embryo by relative position alone, without lineage tracing. For large-scale imaging studies, where identification of any precursor cell of interest is desired, this would drastically reduce the required imaging time per embryo. This may also reduce the cumulative phototoxicity, potentially allowing us to take higher quality images during the time of nerve ring formation. Beyond the scope of this project, this method could also be used to identify cells in fixed embryos (e.g. antibody staining) or in electron micrographs.

We expect that nuclei in intermediate stages should be identifiable by single time points, based on the assertions found in Sulston's paper and others<sup>30,110,111</sup>, suggesting that all cells can be reliably identified by eye at the 28-cell stage and even in much later stages. Our ability to identify intermediate time points will depend on the amount of variability of cellular positions in the embryo. Recent studies have addressed this question, suggesting that positional variability for individual cells is quite low, particularly early in the development. One study has shown that, before 200 cells, the volume describing one standard deviation in the positional variation of each single cell does not overlap with neighboring cells, indicating that each cell has a defined position in the embryo<sup>123</sup>. Another study has shown that nuclei from any embryo are  $\sim 2.2 \mu\text{m}$  from



the same nucleus in an averaged reference model (about 4% of the ~50  $\mu\text{m}$  length of the embryo)<sup>36</sup>. This suggests that simple location-based identification for each cell may be sufficient.

**Starting Data Set:** Using annotations from a publicly available dataset ('Expression Patterns in *C. elegans*', <http://epic.gs.washington.edu>), I tested different methods for cell identification. The embryos in this set are lineaged to various developmental stages (mean = 314 cells, n = 260 embryos) and were compressed during imaging. Approximately 7% of embryos were filtered due to abnormal starting rotations.

**Specific Developmental Times are Suited for Alignment:** I first showed that certain cell-stages are likely to be good candidates for cell identification. Since the relative timing of cell divisions in *C. elegans* is not absolute, the number of cells present does not in general determine the identity of those cells present. For certain cell stages (shown in Table 5), the number of cells “uniquely” (or nearly so) determines the identity of those cells; these cell stages correspond to the time when an entire round of cell divisions is complete and number of cells in the embryo plateaus. The average time spent at these cell-stages is also long (Table 5), which means that identifying these time points during development should be relatively simple.

**A Basic Method for Alignment and Bipartite Matching:** I first used a simple method to align compressed embryos that normalizes the embryo for size based on a minimum volume enclosing ellipsoid, rotates the embryo in the imaging plane to match a common initial axis orientation, and then rotates the embryo by 180° along the L-R and A-P axis (4 possible configurations). (This strategy has been used in previous work for generating average embryo datasets.<sup>36</sup>)

I then used a simple bipartite strategy to compute a matching between two sets of coordinates. This strategy assigns each cell from a test embryo to a cell from the reference (average) embryo where the cell identity is known. The bipartite algorithm computes the match with the lowest cost (the summed distance between matched points is lowest). The performance of the simple bipartite match is given in Table 5. Remarkably, this simple strategy leads to >70% accuracy at cell stages before 190-cells (AB128). This further indicates that the positions of cells are relatively fixed.

**Table 5: Developmental Cell-Stages Used for Cell Identification and Performance of Matching Algorithms**

Cell Stage	Approx. Developmental Time (m.p.f.), 20°C	Avg Time Spent in Stage (min)	% of Cell Identities Shared Between 2 Embryos at the Same Stage (avg)	Basic Bipartite Matching	Bipartite Match + Iterated Horn's Method
<b>26-cells</b>	145	5.52	100%	<b>100%</b>	<b>100%</b>
<b>51-cells</b>	170	7.21	100%	<b>93.2%</b>	<b>97.6%</b>
<b>87-cells</b>	195	4.54	100%	<b>74.5%</b>	<b>82.8%</b>
<b>190-cells</b>	240	1.88	99.3%	<b>73.7%</b>	<b>83.4%</b>
<b>361-cells</b>	300	1.32	98.4%	<b>64.1%</b>	<b>80.4%</b>

**Iterated Heuristic Transformations:** Next, I noted that embryos that perform poorly using this method often have internal rotations of cells in the x-y plane or the y-z plane. (Figure B.1A). These rotations occur variably during development and have been noted

by a recent study<sup>123</sup>. Thus, I implemented an iterative heuristic method, which rotates the embryo slightly and recomputes the matching to improve the result. This method relies on the idea that since a large fraction of cells usually match correctly after the alignment, this match contains information about the how the test embryo is shifted with respect to the reference embryo, and can therefore be used for better repositioning.

In this iterated method, the bipartite match is first computed, as before. This bipartite match, which gives a 1-1 correspondence between points, is used to determine a rigid transformation that reduces the distance between these point sets. This transformation has a single solution. After transformation, the bipartite match is computed again, followed by another round of rigid transformation to reduce the distance between the points. The iterations are stopped when the distance to the reference points no longer decreases after transformation (Figure B.1B). Using this iterated method significantly improves the result, with the fraction of cells matching correctly increasing to >80% at all stages tested (Table 5).

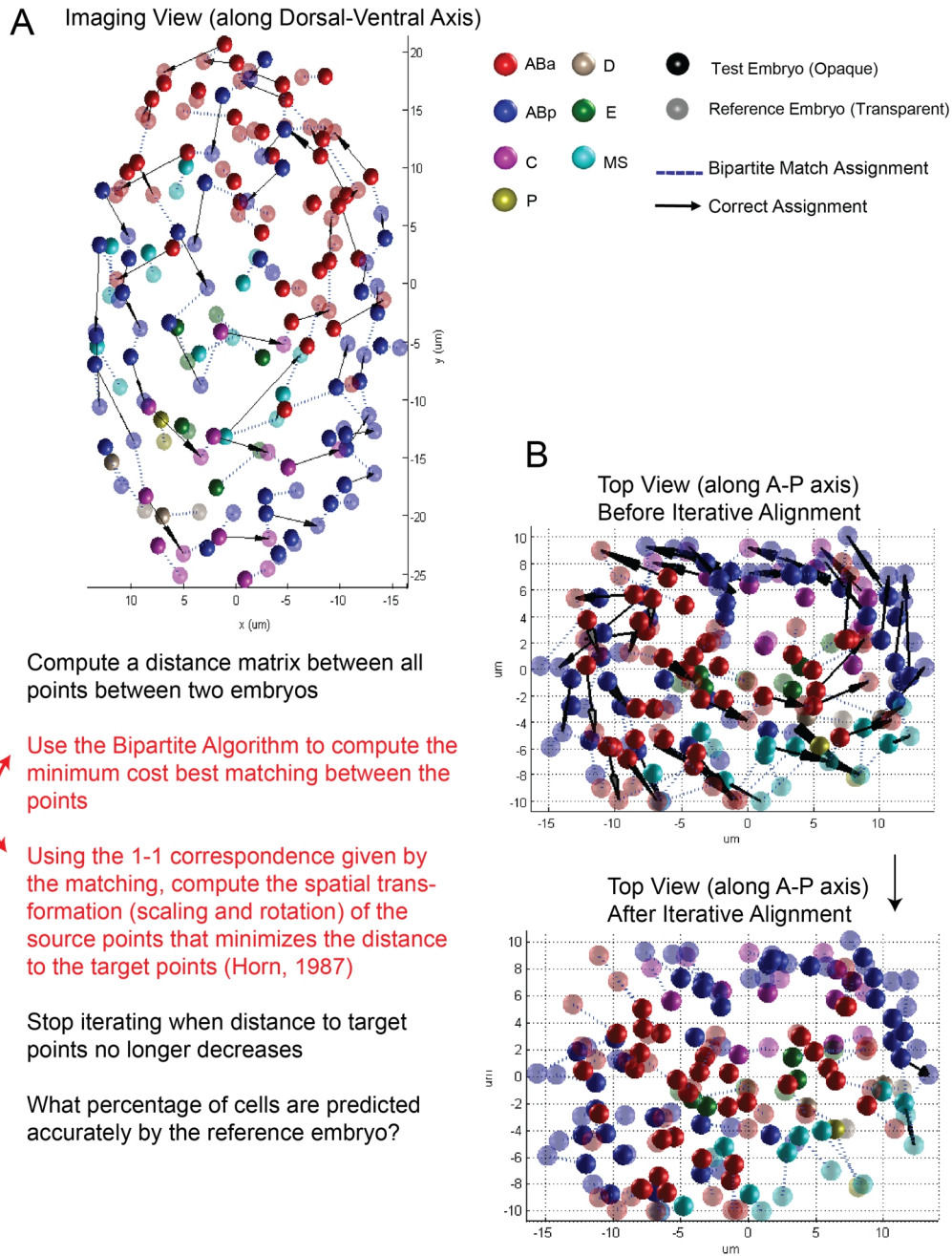


**Figure B.1 Bipartite Matching and Iterated Heuristic Transformations** (A) Due to rotations of cells in the x-y or x-z planes, bipartite matching often performs poorly. When cells are matched incorrectly by the computer algorithm, an arrow shows the correct assignment. Note that the arrows all point clockwise. (B) An iterated heuristic algorithm (left) improves the matching. Note the improvement after rotation (fewer arrows indicating errors).

**Summary and Discussion:** Here I describe a proof-of-principle study addressing whether cells can be identified without lineage tracing in the wildtype embryo. These studies relied on a well-annotated, publicly available dataset of 260 lineaged embryos to test a number of heuristic methods. Using our strategy, cells can be identified at specific developmental stages at rates  $>80\%$ . If some amount of error can be tolerated in cell-identification, this method may prove to be a convenient short-cut for identifying any cell for IR induction.

Implementing this strategy on “real” datasets poses a number of additional challenges. Our method relies on high accuracy in determining the number of cells present, such that these specific cell-stages can be identified reliably. In annotated data sets, the presence of all cells has been verified manually. In real data sets, the error rates in segmentation may prevent such an accurate determination (for example the presence of false positives or missed cells). An important future aim is to determine how well our matching strategies perform with a few additional or missing cells. These randomizations can be performed computationally and tested.

An ideal version of this method would allow the user to “jump in” at any point in the developmental course of the embryo. This method would process time-lapse images of the nuclei present, generating “guesses” of the cell identities, and continually updating the guesses to take into account information about relative timing of cell division between cells, angle of cell division, and trajectory of cell migration as the imaging proceeds. These additional parameters are likely to give much more information about the identity of the cell, and thereby increase the likelihood of correct cell identification. However, this algorithm requires much more flexibility, as the identities of the cells

present are not fixed, and requires much more analysis on the characteristic behavior of individual cells.

An alternate strategy that we did not explore relies on the use of fiduciary markers to label subsets of cells that can be uniquely identified. Such a strategy has been used to create a digital atlas of L1 larval animals.<sup>124</sup> (This atlas does not annotate most neurons of the nerve ring). The annotation of new datasets using this method relies on the distance of nuclei to easily identifiable body wall muscle markers. Using sparse markers, like *unc-130* (described in Chapter 3), a similar strategy could be attempted for the embryo.

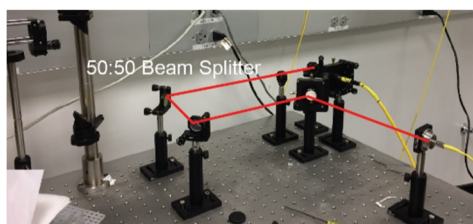
## Appendix C: Introduction of IR Laser System to SPIM Microscope

**Introduction:** As described in Chapter 1, light sheet microscopy offers a number of advantages over confocal microscopy for embryo imaging. It is gentler, thereby allowing higher signal-to-noise images to be taken and at higher temporal resolution. Secondly, the scanning of the light sheet allows for relatively blur-free imaging after twitching. During this work, Peter Insley built a SPIM microscope in our lab for imaging neurodevelopment in *C. elegans* embryos.

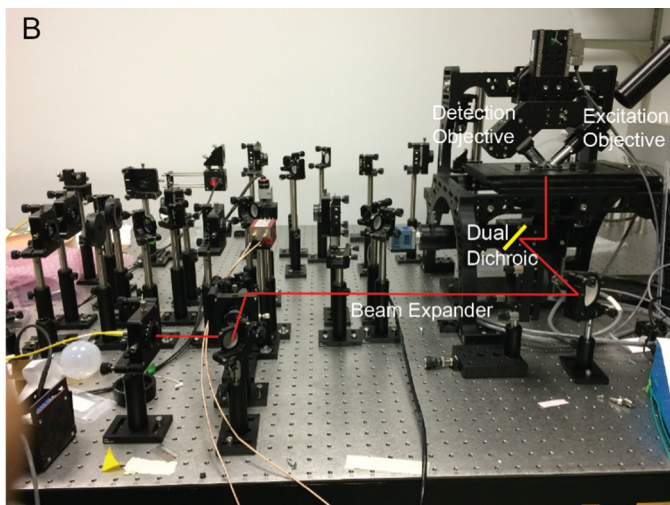
Our aim for this work was to combine the IR and SPIM systems, thereby allowing infrared labeling and gentle imaging of embryos on one microscope. We also hoped to integrate the StarryNite automated lineage software<sup>3,31</sup> to identify any cell of interest for targeting prior to induction, using time-lapse imaging of pan-nuclear markers using the SPIM system.

**Construction of IR Optical Path:** The IR beam is introduced to the SPIM microscope through an objective on the bottom imaging axis (Figure C.1). In conventional SPIM microscopy, this bottom imaging axis is primarily used for identification of embryos using bright-field imaging, and for alignment of the top excitation and detection objectives. The underside objective can also be used for optical perturbations that require high N.A. oil immersion objectives, although no currently published system has used this strategy. From the underside objective, the sample is in the traditional imaging orientation (the sample is viewed through this objective through a perpendicular coverslip), and this objective can be placed close to the sample without steric hindrance from the other objectives.

A



B



C

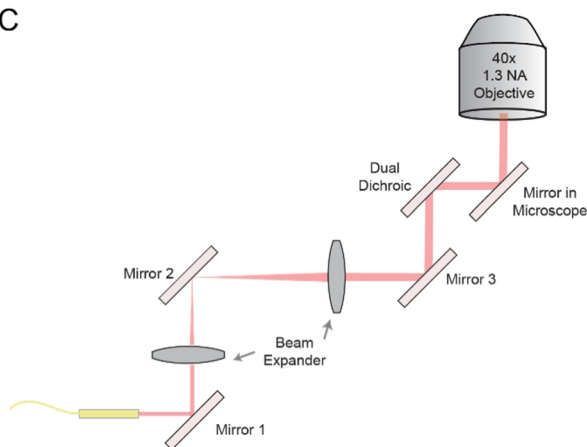


**Figure C.1 Construction of IR Optical Light Path.** (A) Optical Path on IR Table: A beamsplitter divides the IR beam into a path that goes to the IR microscope (left) and one that is coupled to a single-mode fiber (shown in red). (B, C) Optical Path on SPIM Table. The beam from the single-mode fiber is expanded and directed to a microscope port leading to the objective. Mirror 1 and Mirror 2 are used for alignments.

To direct the IR laser to the SPIM microscope while maintaining the IR path on the current setup, we first used a 50:50 beam splitter to create two separate optical paths. As we were concerned that vibrations from the IR microscope table would affect the alignment of the IR beam on the SPIM table, we then focused the light into a single mode



fiber (which maintains the high focusing ability of the light beam), and output the beam from the cable onto the SPIM optical table (Figure C.1). The coupling efficiency of the IR laser into the cable is ~40%.

We constructed an optical path on the SPIM table that allows for spatial control of the IR beam focus by the use of two mirrors; one is conjugate to the back focal plane of the objective, to control the laser position (Mirror 1), while the other is conjugate to the imaging plane, which is used to control laser angle at the focus of the objective (Mirror 2). A long-pass dichroic (Q495lp, Chroma Technology) was used to direct the laser towards the objective. This dichroic allows for GFP fluorescence imaging simultaneously with IR induction, allowing us to visualize nuclear markers for targeting specific cells. The alignment of the IR beam was performed using a similar strategy as described in Chapter 2, using the reflection of the beam as visualized on a camera.

**Strategy for Inducing Cells and For Registering Images:** In order to maintain light efficiency, the embryo must be imaged using SPIM microscopy from the top axes, and then the coordinates of the appropriate cell must be fed to the bottom axis for IR induction. This setup requires that coordinates of a nucleus are transformed from the top image volume to the bottom axis, as the view of the sample is shifted by approximately 120°. To calculate the exact transformation, corresponding points must be identified in images from both the SPIM imaging objective and the underside IR induction objective. We therefore developed a widefield imaging strategy to gather images from the underside objective.

This widefield strategy was used for two aims: (1) to identify cells of interest for induction directly through the underside objective, thereby allowing for optimization of IR induction parameters on the SPIM microscope until the registration system is developed (2) to image the same sample from the top and bottom objectives and use corresponding points to develop a registration method. Eventually, after a registration system is established, the transformation of a coordinates from the top objective to the bottom induction objective should be performed without widefield imaging from the bottom objective.

**Widefield Imaging from Underside Objective:** To gather fluorescent images from the bottom axis, as is required to find GFP-marked nuclei in a volume (e.g. *unc-130* for induction experiments), we realized that the entire sample must be illuminated to gather one slice of fluorescence, as with conventional widefield microscopy. This is due to the fact that the sheet generated by the excitation objective illuminates a section that is not perpendicular to the underside objective. We therefore developed a system to synchronize the underside camera from the bottom objective to the light sheet illumination from the top axes, such that one imaging slice is taken per light-sheet volume. Peter developed software to feed inputs from the LabView control scripts on the SPIM SuperMicro workstation to a Dell computer which controls the PCO Pixelfly camera, used for underside objective image acquisition. This system is effective for taking widefield stacks of 40-50 slices, with 1  $\mu\text{m}$  spacing.

**Optimization of IR Induction Parameters:** Translating the power parameters from the IR microscope onto the SPIM microscope was difficult, as power sensors are not accurate within  $\sim 10\text{-}15\%$ , and the transmission of the underside objective was different from the

induction objective used on the IR microscope. To identify the power levels required for induction, we used the same strategy for cell identification and scoring cell-specificity as used in Chapter 3. We identified UNC-130-labeled nuclei through the bottom objective with the wide-field imaging strategy described above. We then centered the nucleus of interest in the field of view to align it to the laser focus, and irradiated the cell.

An induced embryo with specific labeling is shown in Figure C.2. Induction parameters that reliably induce cells have not yet been identified (there is frequent, unexplained off-target induction), so further optimizations of induction parameters on the SPIM microscope are in progress.

**Image Registration from Top and Bottom Axes:** To produce alignments between top and bottom axes, we imaged the same 3D sample viewed from both objectives. Separate from this work, Peter has developed a system using the UNC-130-GFP marker to register embryos in different orientations on a common coordinate system for comparing neurite outgrowth. To utilize his existing pipeline, we decided to use embryos with UNC-130-GFP-marked nuclei as a set of sparse points for registration. These points are used to calculate a rigid transformation that maps the cells on top of each other from two different views. A sample alignment is shown in Figure C.2B. Note that the nuclei should exactly co-localize as the images are of the same embryo at the same time point but from different views. Therefore, any misalignment is either due to the algorithm or warping of the image volume due to different resolutions and sampling orientations through different objectives.

Ideally, the transformation generated by conducting this alignment on one embryo would be used to transform between the top and bottom views for any other embryo;

thus, the IR laser could be directed to the correct point without requiring imaging through the bottom objective, which is not light-efficient. The alignment method requires further improvement; in particular, the z-positions of registered nuclei do not appear to be accurate, which may be due to the wider point spread function of the wide-field system as compared to the SPIM system.

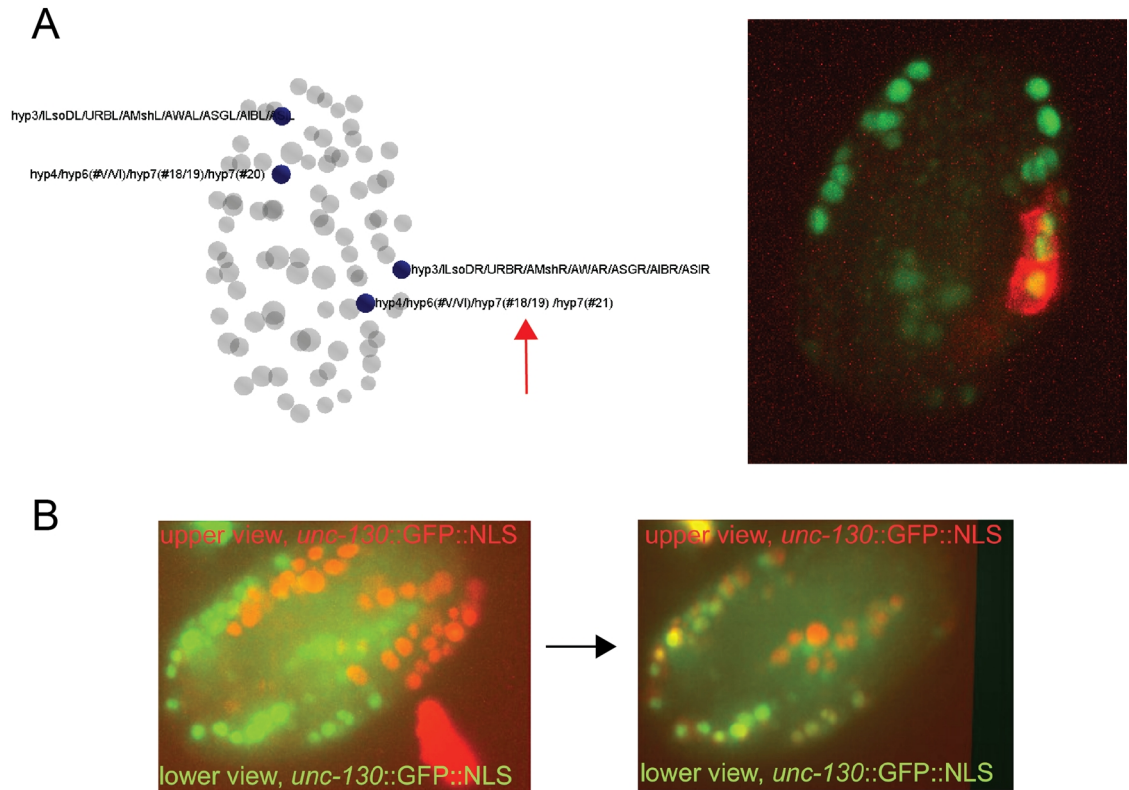


**Figure C.2 IR Induction Optimization and Registration Methods for SPIM**

(A) Induction of a hypodermal cell precursor labeled by UNC-130-GFP (left) leads to induction in four cells. Note the co-localization of the heat-shock driven myr-mCherry signal with the UNC-130-GFP signal. This image was acquired on SPIM. (B) Left: The same embryo is visualized from the upper SPIM imaging axis (red), and the lower underside objective (green); Right: After alignment, the nuclei register on top of each other, although slight misalignment is still visible.

## **Appendix D: Characterization of Regulators of Glial Specification in *C. elegans***

This work was performed in collaboration with a previous student in the lab, Satoshi Yoshimura.

### **Introduction:**

Glia are a major cellular component of vertebrate nervous systems. Many studies have demonstrated that glia have active roles in the nervous system, including modulation of synaptic activity in neurons and directing neurite guidance<sup>1,2</sup>. The *C. elegans* hermaphrodite contains 56 glial cells, and is a promising system to study glial development *in vivo* as glial manipulation does not result in neuronal death<sup>3</sup>.

Recent work from our lab has shown that *C. elegans* glial cells have functional similarities to vertebrate glia; *C. elegans* glia regulate the shape of neuron sensory endings<sup>4,5</sup>, direct axon outgrowth in the developing brain-like nerve ring (Rapti et al., submitted), and control motor output through regulation of synapses (Katz et al., submitted). Recent studies have also demonstrated that molecular pathways leading to glial differentiation in *C. elegans* are conserved in other systems. The well-studied *Drosophila* glial fate regulator Prospero is expressed broadly in *C. elegans* glia, where it has roles in regulating the transcription of secreted proteins<sup>5</sup>. The *C. elegans* CEP sheath glial cells, which envelop the central nervous system of the animal, express *hlh-17*, a homolog of the vertebrate Oligodendrocyte Transcription Factor 2 (Olig2), and upstream regulators of *hlh-17* expression in *C. elegans* have similarly functioning vertebrate homologs<sup>6</sup>. The transcriptional factor *mls-2* controls ventral expression of *hlh-17* in the

*C. elegans* CEPsh, and interestingly, vertebrate Nkx6, a homolog of *mls-2*, regulates ventral Olig2 expression in the spinal cord. Similarly, in the dorsal CEPsh, *hlh-17* expression has been shown to be downstream of *vab-3*, a homolog of Pax-7 which controls Olig2 expression in the dorsal spinal cord. Both *mls-2* and *vab-3* also control expression of a Patched-related gene, *ptr-10*, which is expressed almost exclusively in all *C. elegans* glia. Recent work has shown that the Patched-related gene, *ptr-7/daf-6*, is required for lumen formation in the *C. elegans* amphid sheath glial cell, but the role of *ptr-10* in glial development is not known <sup>7</sup>.

In this study, we use *C. elegans* glia as a system to further study molecular mechanisms of glial specification. We first show that *ptr-10*, like *ptr-7/daf-6*, has a role in lumen formation in glial cells. Next, we show that *ptr-10* expression in glia can be regulated by bHLH factors, including Olig2/*hlh-17*. To identify upstream regulators of glial differentiation, we perform a genetic screen aimed at finding mutants defective in *ptr-10* expression, and identify a novel upstream regulator of glial gene expression, *bath-43*. Interestingly, *bath-43* is a close evolutionary homolog of the well-studied mammalian gene SPOP, which acts as a substrate-specific adaptor to target proteins for degradation by Cul-3-mediated ubiquitination <sup>8,9</sup>. Our study identifies a novel molecular pathway governing glial differentiation in *C. elegans* and suggests a previously uncovered role for the *bath-43*/SPOP gene.

### ***ptr-10*/Patched-related functions in glial lumen formation**

*ptr-10* has been shown to be expressed in all glial cells in *C. elegans*, as well as the vulva, excretory cell, and rectal epithelium <sup>6</sup>, but the function of *ptr-10* is not known. As *ptr-7/daf-6* has a critical role in the formation of the lumen of the amphid sheath, we looked

for similar defects through electron microscopy in *ptr-10(tm2586)* mutants, which contains a large frameshift deletion in the C-terminal region. We specifically looked at the anterior most region of the head, where glial cells for each sensilla form a channel through which neurons exit (Figure 1A). Strikingly, we found that in all animals observed, at least two of the six channels through which the IL1 and IL2 neurons exit are severely bloated (n = 3 animals; Figure 1B). The enlargement of the channel occurs below the socket-sheath junction, suggesting that the IL sheath is specifically affected by the *ptr-10* mutation. At the level of the sheath, this defect appears very similar to the enlargement seen for the amphid channel in *ptr-7/daf-6* mutants<sup>7,10</sup>. However, unlike *ptr-7/daf-6* mutants, the IL neurons successfully exit the channel in *ptr-10* mutants, and the socket region of the sensilla appears unperturbed. Indeed, when we performed dye-filling assays on the IL neurons<sup>11</sup> we did not observe defects, nor were gross defects in IL dendrites visible using fluorescent reporters. Electron microscopy of a weaker allele of *ptr-10*, which causes a large in-frame deletion, also revealed vacuoles near the dendritic tips of cells, but these vacuoles were observed in association with diverse glia and did not specifically affect the channel of the neurons (data not shown). As both alleles of *ptr-10* show similar defects, our results point to a role for *ptr-10* in forming a properly sized glial lumen.

### **bHLH Transcription Factors Regulate *ptr-10* expression**

Next, we aimed to determine which transcription factors are directly involved in activating *ptr-10* expression. Given that the homolog of *hlh-17/Olig2* is expressed specifically in *C. elegans* glia<sup>6,12</sup>, we were interested to find two E-box consensus sequences (5' CANNTG 3'; Ebox1 and Ebox2 shown in Figure D.2A), which are known

to bind bHLH transcription factors. Both of these sequences are contained within a 300 bp upstream promoter sequence of *ptr-10*, which recapitulates the expression pattern of a *ptr-10* fosmid-based reporter containing all regulatory elements.

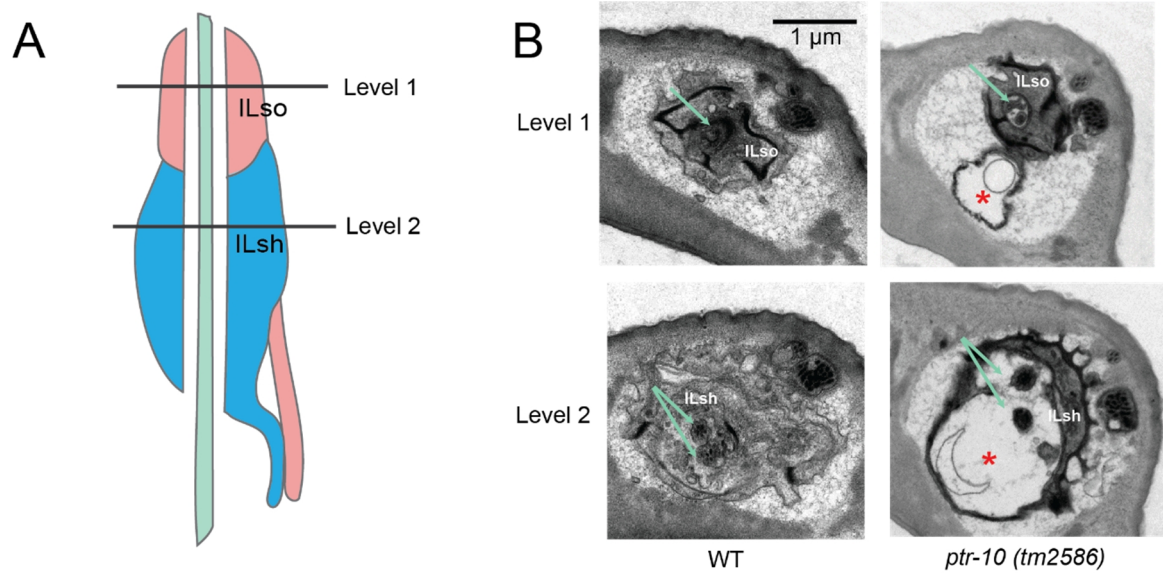


**Figure D.1 *ptr-10* regulates IL sheath lumen formation** (A) The IL socket and sheath form a connected tube through which the IL neuron exits (B) EM of two anterior sections in wildtype and *ptr-10* mutants are shown for comparison. Note the large lumen in the IL sheath (asterisk)

To determine whether these E-boxes are functional *in vivo*, we introduced three points mutations into each E-box that eliminate functions of the consensus sequence (Lee et al. 2005). Surprisingly, the glial expression of the *ptr-10<sub>pro</sub>::myrRFP* reporter was completely abolished when the E-box2 was mutated (Figure D.2A), while mutations in the E-box1 had no apparent effect on the reporter expression<sup>13</sup>. These observations suggest that at least E-box2 is functional *in vivo* and that *ptr-10* is regulated, at least in



part, by bHLH transcription factors. Interestingly, reporter expression in other non-glial cells was maintained, suggesting that bHLH factors act specifically within glia.

Given its expression in glia, *hlh-17* is a potential candidate for this transcriptional activator. To test whether *hlh-17* can regulate *ptr-10*, we ectopically expressed a transgene, consisting of the full-length *hlh-17* cDNA fused to a heat-inducible promoter. In pre and mid-morphogenesis embryos (270 min-430 min) subjected to heat shock activation, hatched L1 larvae expressed *ptr-10<sub>pro</sub>::myrRFP* at a much higher intensity than L1 larvae from non-heat shocked embryos. However, though heat shock induces expression of *hlh-17* in all cells, myr-RFP expression was not present in additional cells. This suggests that *hlh-17* can regulate *ptr-10*, but is not sufficient to induce *ptr-10* expression. In line with this result, a deletion mutant of *hlh-17*, *hlh-17(ns204)*, did not exhibit defects in *ptr-10* expression nor did a triple deletion of all Olig2 homologs in *C. elegans* (*hlh-32(ns223)*, *hlh-17(ns204)*; *hlh-31(ns217)*). As bHLH proteins are a large class of proteins in *C. elegans* (42 members) and bHLH proteins often act as heterodimers in other systems, it is likely that other bHLH factors act as co-factors or redundantly with *hlh-17* to regulate *ptr-10* expression.

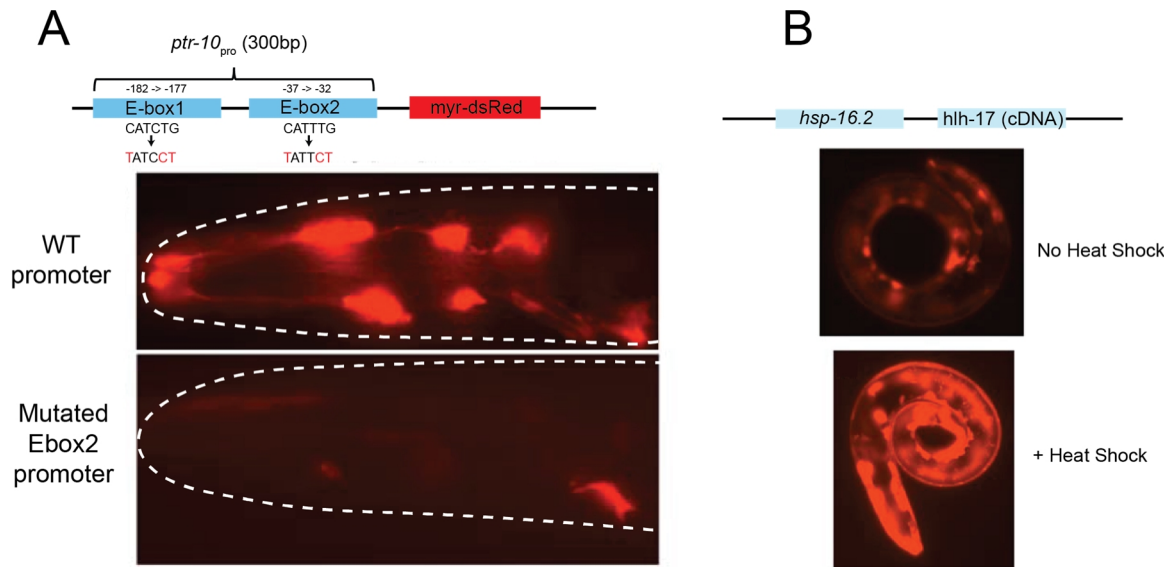


**Figure D.2: bHLH transcription factors regulate *ptr-10* expression**

(A) A 300 bp upstream sequence to the *ptr-10* start site drives expression in glia, excretory cell, vulva, and rectum. This regulatory sequence contains two E-box sequences which are indicated by blue boxes. Numbers indicate genomic positions with respect to the ATG start codon. Mutations in Ebox2 abolish expression of *ptr-10* in glia, but not in other cells.

(B) Overexpression of *hlh-17* cDNA embryonically using a heat-inducible promoter induces *ptr-10* reporter transgene expression. (left) Non-heat shocked, hatched L1 (right) Heat-shocked, hatched L1. Exposure time is constant for both images.

### A Genetic Screen to Identify Regulators of Glial Differentiation

We undertook a genetic screen to further identify upstream regulators of glia-specific genes. We mutagenized animals carrying an integrated *ptr-10<sub>pro</sub>::myr-dsRed* transgene (Figure D.1A) and scanned F2 progeny for changes in reporter expression. From 30,000 haploid mutagenized haploid genomes visualized, we isolated one mutant, *ns2870*, which abolished expression in the CEPsh glia. We were intrigued by the specificity of this

mutant, as it maintains equal expression to wildtype in other glia, the vulva, and excretory system (Figure D.3A).

As shown in Figure D.3B, >60% of *ns2870* animals show loss of *ptr-10* expression in all four CEPsh, with another 20% showing dorsally-restricted expression (Figure D.3A, lower panel). The *ns2870* mutant also strongly diminishes *hlh-17* reporter expression (Figure D.3C,D), indicating that it acts upstream of both genes. We also examined expression of other pan-glial genes, *ceh-26*/Prospero and the microRNA *mir-228* (Figure D.3E,F). Neither of these genes showed defects in expression in *ns2870* mutants, indicating that mutation only affects a subset of genes in the CEPsh. Moreover, as the CEPsh nuclei and processes were visible with the cytoplasmic *mir-228* reporter (Figure D.3F), the mutant *ns2870* does not affect the generation of the CEPsh, but rather some aspect of their specification.

SNP mapping with 78 recombinants was used to map *ns2870* to a 3.98 map unit interval (1.1 Mb) on Chromosome III. Through whole genome sequencing, we found that this region contained a single coding mutation in the gene *bath-43* (genomic locus shown in Figure D.4A), and a fosmid containing the genomic sequence of *bath-43* rescued the defect (Figure D.4B). An allele of *bath-43* containing an early nonsense mutation recapitulates the expression defect, although it is less penetrant. However, another strong missense mutation in a nearby amino-acid, also in the C-terminal region of the protein, causes a strong penetrance defect (Figure D.4C). Thus, we show that *ns2870* is an allele of the gene, *bath-43*.

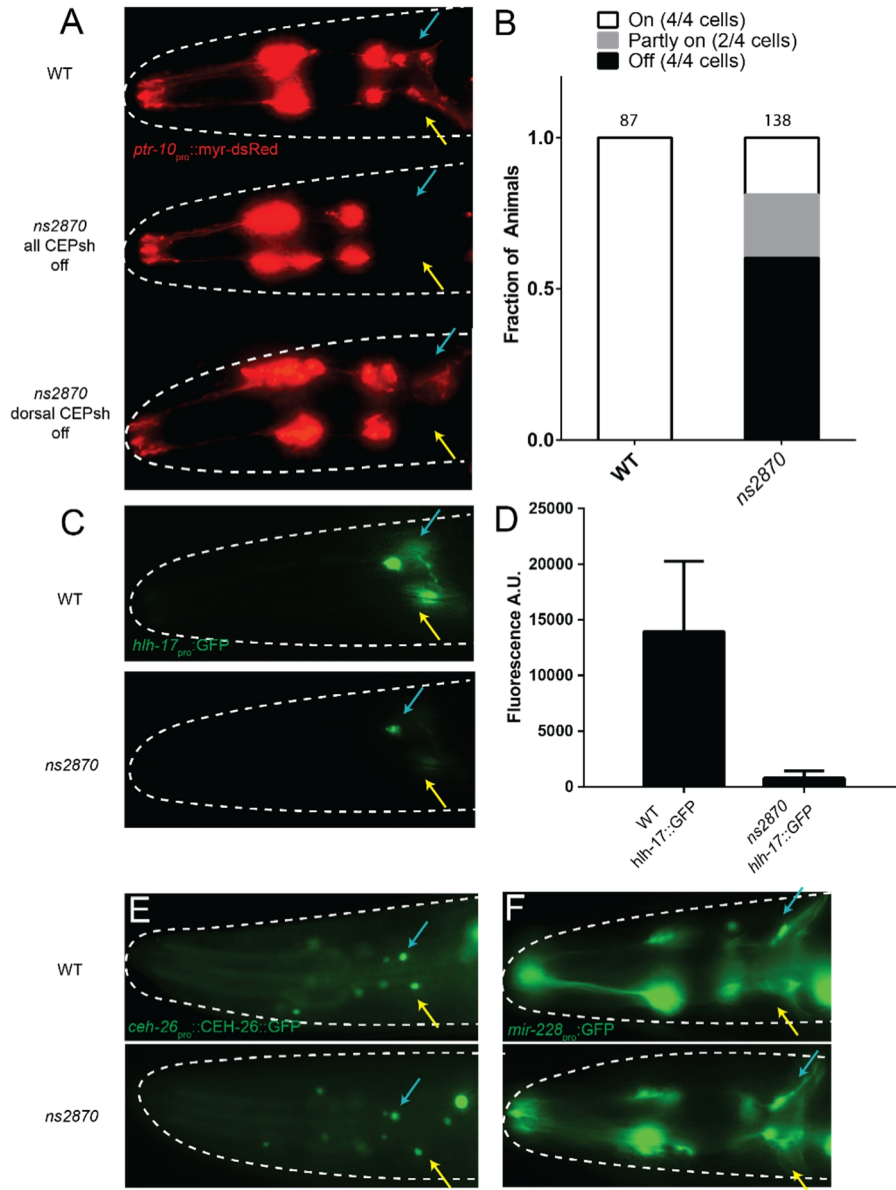


**Figure D.3: *ns2870* affects glial reporter expression specifically in the CEP sheath**

(A) Defects in *ptr-10* expression. dorsal CEPsh (blue), ventral CEPsh (yellow) indicated

(B) Penetrance of *ptr-10* expression defect in *ns2870* mutants

(C) Defects in *hlh-17* expression. Images were acquired with the same exposure time.

(D) Quantification of fluorescence reduction with *hlh-17<sub>pro</sub>::GFP* reporter.

(E, F) Expression of other pan-glial genes *ceH-26* and *mir-228* is not affected in *ns2870*

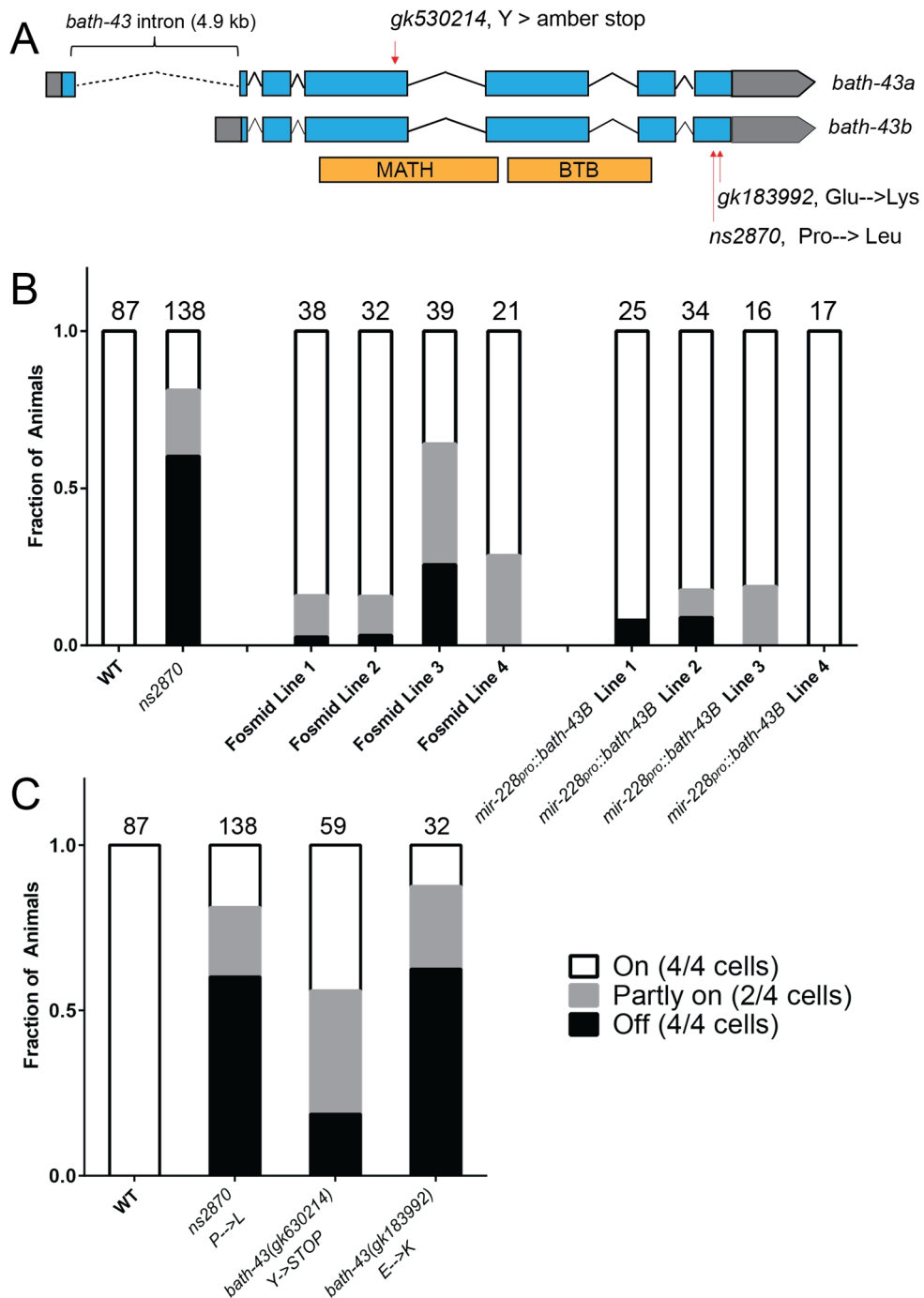


**Figure D.4: *ns2870* is an allele of *bath-43***

(A) Genomic locus of *bath-43*

(B) *ns2870* expression defect in *ptr-10* is rescued by *bath-43*-containing fosmids and by pan-glial expression

(C) Other mutations of *bath-43* show defects in *ptr-10* expression

### ***bath-43* encodes the homolog of mammalian SPOP**

*Bath* genes in *C. elegans* contain BTB and MATH domains, and studies on similar genes in *C. elegans*, *Drosophila*, and vertebrates indicate that they are likely to act as substrate-specific adaptors to a cullin-based nuclear E3 ligase complex, targeting transcription factors and other nuclear proteins for degradation<sup>8,14–16</sup>. (Figure D.5A) Though mammals have only one BTB-MATH containing protein, named SPOP, in *C. elegans* the gene class has been expanded to 47 members<sup>17</sup>. Interestingly, *bath-43* encodes the closest homolog to SPOP, with 91% similarity in the substrate-binding MATH domain. (For comparison, the next closest homolog to SPOP in *C. elegans*, *mel-26*, contains approximately 30% similarity in the MATH domain). (Figure D.5B)

In mammals, SPOP has a number of known targets including androgen receptor and the DEK and ERG oncogenes<sup>18,19</sup>; of clinical interest, SPOP is mutated in ~10% of prostate cancers<sup>20</sup>. In *Drosophila*, the single BTB-MATH containing protein Hib has been shown to directly degrade Ci, a zinc-finger transcription factor that activates Hedgehog signaling and segment polarity<sup>16,21</sup>. No studies have elucidated roles for *bath-43* in *C. elegans*, and roles for SPOP in glial differentiation are also unknown. The high sequence similarity between *bath-43* and SPOP/Hib suggests that there may be evolutionarily conserved substrates between these proteins.

### ***bath-43* acts within glia and localizes to nuclear speckles to control expression of *ptr-10* and *hlh-17***

To determine if *bath-43* acts within the CEP sheath to regulate *ptr-10* and *hlh-17* expression, we expressed BATH-43B under the pan-glial *mir-228* promoter, which is

expressed in all glia from embryonic to adult stages. We found that this transgene achieved nearly complete rescue of the *ptr-10* reporter defect in four independent lines (Figure D.4B). We also quantified *hlh-17* reporter expression with the BATH-43B rescuing transgene, which achieved nearly 80% rescue of reporter expression (Figure D.5B). As homologs of *bath-43* in other systems have been shown to behave cell-autonomously in controlling transcription through degradation of nuclear substrates, this result strongly suggests that *bath-43* acts directly within the CEP sheath cells to promote *ptr-10* and *hlh-17* expression.

To determine in which cells *bath-43* is expressed, we examined wildtype animals containing a transgene expressing GFP under the control of first intron of BATH-43A. This intron is large (5.5 kb) and begins directly before the start codon of the more highly conserved BATH-43B isoform (Figure D.4A). The region between the upstream gene and the BATH-43A isoform is only ~200 base pairs, and thus was not characterized. This regulatory sequence of *bath-43* showed expression in a number of cells including a number of cells clustered around the nerve ring, the pharynx, and tail (Figure D.4C). In most examined animals, a GFP-labeled sheath-like process was visible in the region of the nerve-ring. As the nerve ring is ensheathed by the CEPsh glia, this expression pattern, along with our rescue data, suggests that *bath-43* is expressed and acts in CEPsh glial cells.

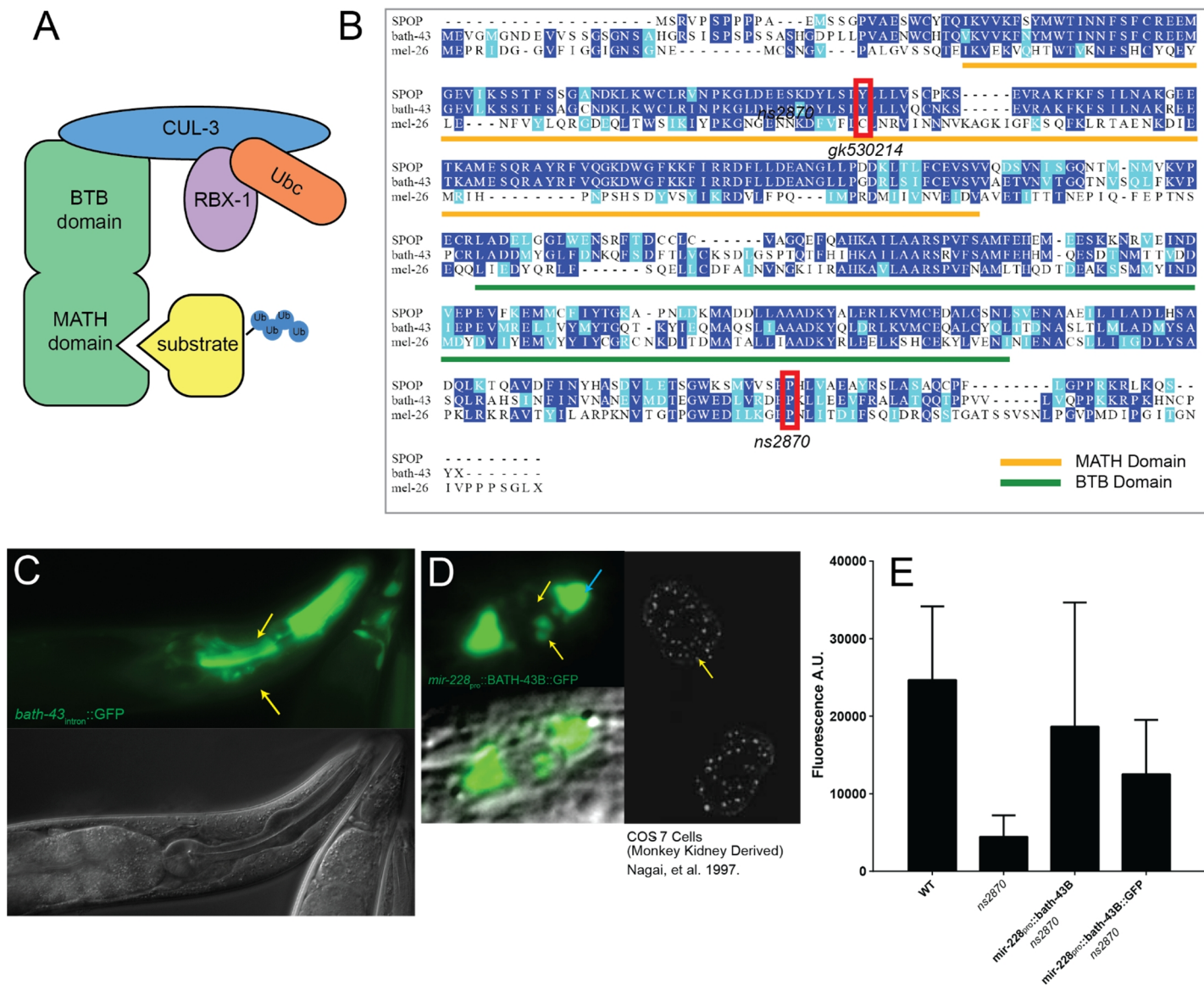


**Figure D.5: Function and Localization of *bath-43***

- (A) BTB-MATH containing proteins (green) act as substrate-specific adaptors to a CUL-3 mediated ubiquitination complex
- (B) Evolutionary conservation between *C. elegans bath-43*, *mel-26* and human SPOP
- (C) Expression pattern of *bath-43*
- (D) Subcellular localization of *bath-43* (left). For comparison, SPOP localization in COS7 cells (right)
- (E) Rescue of *hlh-17* expression defects by BATH-43 and BATH-43B::GFP



### ***bath-43*, like its homologs, localizes to speckles in the nucleus**

We generated a BATH-43B::GFP fusion and expressed it under a pan-glial promoter to determine the subcellular localization of the protein. Interestingly, the GFP-tagged protein appears to localize to small speckles in the nucleus, similar to its human and fly homologs<sup>16,22</sup> (Figure D.5D). Of note, perhaps due to the small size of the nucleus or due to toxicity of the GFP-tagged protein, we were not able to observe the tagged protein in the CEP sheath cells, but expression was easily visible in anterior glial cells. In addition to the nuclear speckled expression, BATH-43B::GFP also was contained in the cytoplasm (Figure D.5D). To see if the cytoplasmic expression was caused by overexpression, we created low-copy number versions of the array, but this did not alter the localization. We also determined whether the BATH-43B::GFP fusion could rescue defects of the *hlh-17* reporter. Approximately 50% rescue was observed, indicating that the subcellular localization that we observe is functional (Figure D.5E). Thus, *bath-43* in *C. elegans* has a similar subcellular localization pattern in the nucleus to its vertebrate homolog, but may additionally have a cytoplasmic function.

### ***bath-43* mutants show excessive matrix accumulation in the CEPsh sensory channel**

In order to visualize the processes of the CEPsh cells at high resolution, we performed electron microscopy on *bath-43* mutant animals. Interestingly, we observed abnormal dark-staining matrix accumulation in the CEP sensory channel. This defect was highly penetrant, as 4/4 animals sectioned had dark, expanded matrices in the lumen of all 4 CEP sheath. The neighboring OLQ dendrite also showed a lesser but similar defect, and abnormal dark staining was also seen infrequently in the amphid sensory channel (2/8

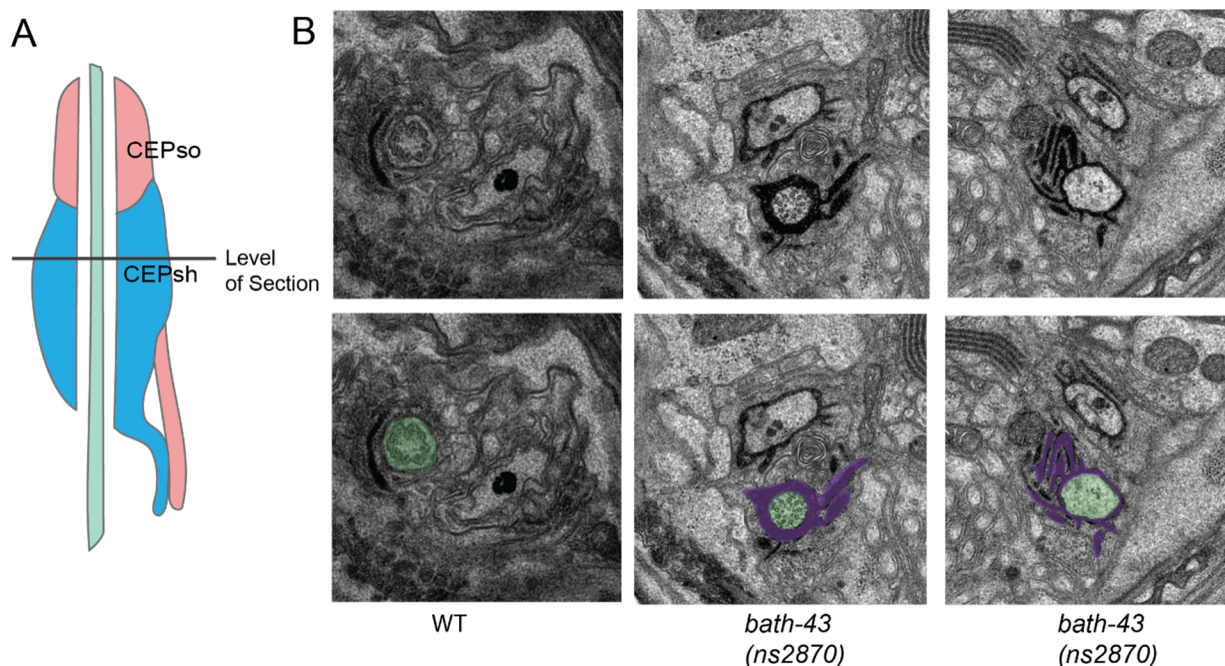


**Figure D.6: *bath-43* mutants show excessive matrix accumulation in the CEPsh sensory channel** (A) Schematic shown the lumen of the CEPsh. The level of the EM section shown in B is indicated. (B) (Top) WT and *bath-43* sections showing morphology of the anterior tip of the CEPsh. (Below) The images are annotated to show the dendrite (green) and the surrounding lumen (purple)

channels). However, all other glial sensory channels appeared normal in these mutants. The specificity and high penetrance of this defect specifically in the CEPsh is consistent with the high penetrance of the *ns2870* allele. Thus, these results suggest that *bath-43* causes a secretion defect.

As other mutants affecting CEPsh differentiation affect dendrite and axon guidance<sup>6</sup>, we also looked for such defects in *bath-43(ns2870)* mutants by light microscopy. However, no defects in the length of CEP dendrites or axon trajectory of amphid neurons were observed (data not shown). As recent work has shown that the CEPsh acts to regulate specific synapses involved in locomotory behavior (Katz et al.,

submitted), we also quantified locomotion, but these assays did not reveal any strong deficits. These studies suggest that, in *bath-43* mutants, the CEPsh has a normal function in nervous system development and regulation even in the context of other defects.

### **A yeast-two-hybrid screen reveals potential substrates of *bath-43***

The MATH domain in *bath* genes confers substrate-specificity for Cul3-mediated degradation, and yeast two-hybrid screens have been performed with other such genes in *C. elegans* to identify putative substrates<sup>23</sup>. Therefore, we performed a yeast-two hybrid screen with the full-length *bath-43* gene as a bait. From a screen of 10<sup>6</sup> clones, we identified 27 independent clones; many of the genes were only identified once, indicating that our screen was not saturated.

A recent study has identified a SPOP binding consensus (SBC) based on deletion mapping of two known substrates<sup>24</sup>. The binding consensus sequence is  $\phi$ - $\pi$ -S-S/T-S/T ( $\phi$ -nonpolar;  $\pi$ -polar). To direct our attention to more likely substrate candidates, we computationally identified the number of SPOP binding sites in each protein. The number of binding sites with the published SBC and a less stringent sequence are given in Table 6. The transcriptome of the CEPsh cells has recently been determined through cell-isolation and mRNA sequencing experiments in our lab (Katz et al, submitted). As we are interested in putative substrates of *bath-43* specifically in the CEPsh, the number of mRNA reads present in the CEPsh cells and the fold upregulation compared to non-CEPsh cells are given for comparison for each gene.

Interestingly, a number of the genes with high numbers of SBC sequences identified in the screen are zinc-finger transcription factors (*ztf-16*, *elt-2*, *pzf-1*, *rnf-1*);

**Table 6: Interactors with *bath-43* in Yeast Two-Hybrid Screen**

Clone Name	No. of Clones	Putative Function	SBC S-S/T-S/T (Lax)	SBC $\phi$ - $\pi$ -S-S/T-S/T (Stringent)	# Reads CEPsh	Fold Induction ( $\log_2$ )
<i>pzf-1</i>	2	Paired Zinc Finger protein; germline meiosis	2	0	3.0	-19.18
<i>F49E2.5</i>	3	Unknown Function; homology to surface glycoprotein	3	0	21929.0	0.17
<i>F55G11.8</i>	1	Unknown Function; homology to epoxide hydrolase	0	0	435.1	0.20
<b><i>bath-43</i></b>	<b>1</b>	<b>acts as a homodimer</b>	<b>1</b>	<b>0</b>	<b>2650.1</b>	<b>0.46</b>
<i>vit-6</i>	1	vitellogenin	3	1	32.8	0.15
<i>hosl-1</i>	1	hormone-sensitive lipase	3	0	1975.3	0.22
<b><i>ztf-16</i></b>	<b>1</b>	<b>zinc finger transcription factor</b>	<b>5</b>	<b>2</b>	<b>1285.3</b>	<b>-1.31</b>
<i>act-4</i>	2	actin isoform	1	1	610611.6	-0.17
<i>him-1</i>	1	germline mitosis, chromosome cohesion	0	0	3715.2	1.09
<i>fum-1</i>	1	fumarase; mitochondrial	0	0	16703.7	0.38
<i>elt-2</i>	1	GATA TF; intestinal differentiation	5	2	246.0	0.20
<i>fbf-2</i>	1	RNA-binding protein; germline development	1	0	135.9	-0.98
<i>vit-2</i>	1	vitellogenin	2	0	20.7	-1.01
<i>rnf-1</i>	1	ring finger protein, zinc ion binding activity, may regulate ubiquitination	2	0	151.6	-1.12
<i>col-93</i>	1	collagen	0	0	3728.0	-1.39
<i>ant-1.1</i>	1	mitochondrial adenine nucleotide transporter	3	0	252297.6	-0.52
<i>clac-48</i>	1	C-type lectin	0	0	1002.6	-0.20
<i>K06H7.7</i>	1	unknown function	1	0	405.6	0.39
<i>T05E12.6</i>	1	Unknown Function; homology to epoxide hydrolase	2	0	137.2	0.18
<i>F57F5.1</i>	1	Cathespain homolog	0	0	33459.2	-0.43
<i>pho-11</i>	1	Acid phosphatase homolog	0	0	2405.0	0.77
<i>vit-5</i>	1	vitellogenin	1	0	15.5	0.62
<i>asp-3</i>	1	Aspartyl protease homolog	1	0	15221.1	-0.50
<i>pab-1</i>	1	poly(A)-binding protein	0	0	144421.5	-0.31

notably, SPOP has been shown to act with this class of transcription factors, especially Ci/Gli in *Drosophila* <sup>16,21</sup>. Previous work in our lab has shown that *ztf-16* acts within the amphid sheath glia to regulate its expansion and fusion during dauer <sup>25</sup>. Electron micrographs of *ztf-16* mutants show that during normal development the amphid sensory channel stains abnormally dark, as do pockets within AMsh glia, similar to our observations of the CEP dendrites in *bath-43* mutants. A role for *ztf-16* in the CEP sheath is not known, but based on these observations as well as expression in the CEP sheath by transcriptome-analysis, it may be a promising candidate for future studies.

Of note, our screen also identified *bath-43* itself as an interactor. As SPOP is known to act as a homodimer in complex with Cul-3 in a 1 (substrate):2 (SPOP):2(Cu-13) complex, the identification of this interactor validates our screen <sup>24</sup>.

### **A strategy for determining transcriptional downstream effectors of *bath-43* in the CEPsh glia**

To determine downstream transcriptional targets of *bath-43*-mediated degradation, we took advantage of recently developed larval cell isolation techniques and modified these for the purpose of identifying differences in the transcriptome between WT and *bath-43* CEPsh cells <sup>26,27</sup>. A specific protocol for isolating CEPsh cells and extracting mRNA for sequencing was recently developed in our lab (Katz et al., submitted). Briefly, the protocol disassociates larval animals while maintaining the cell membranes and nuclei. The dissociated cells are sorted by FACS, and the cell population of interest is separated by using a genetically-expressed fluorescent label. For previous studies, an *hlh-17<sub>pro</sub>::GFP* reporter was used for labeling of the CEPsh. In *ns2870* mutants, *hlh-17* expression is significantly downregulated (Figure D.3C).

Unfortunately, the *hlh-17* reporter is additionally expressed weakly in intestinal cells as well as in a couple of other glial cells and neurons in the ventral cord (Figure D.7A). If only strongly GFP positive cells are selected for, these other cell populations can be excluded, but this is not an option in *ns2870* mutants, where the signal in the CEPsh cells drops to the level of these additional cell groups. Ideally, a completely CEPsh-specific reporter which is not downregulated by *bath-43* would be used for labeling cells in this experiment, but our efforts to find such a promoter sequence or combinatorially label cells were not successful.

Thus, we devised a strategy to use the existing *hlh-17* reporter with *ns2870* mutants without inadvertently enriching for CEPsh cells in the wildtype population due to brighter reporter expression. First, we generated a co-labeled strain with an additional intestinal-specific RFP reporter, allowing us to sort out this population entirely in both wildtype and mutant worms. Secondly, using an unlabeled strain for calibration, the gate for GFP(+) cells was set to be as low/“inclusive” as possible; this allows all GFP(+), even non-CEPsh cells, to be sorted for both WT and *ns2870*, thereby maintaining an equal percentage of CEPsh cells in each population. This way, even if *bath-43* mutants cause a change in expression of a target gene in the CEPsh but do not change that gene’s expression in non-CEPsh cells, the fold reduction of the signal should be no more than  $\frac{1}{2}$  (assuming there are 4 CEPsh cells and 4 other cells being sorted). Thus, a sensitive readout should still be maintained.

Cell sorting and RNA sequencing on both the GFP(+) cells and unlabeled cells for both WT and mutant strains were performed. To confirm that the correct cell populations were being isolated, I performed qPCR for selected genes. The results are shown in Table

7. As expected, *hlh-17* expression is diminished in the mutant population as is *ptr-10* expression. Surprisingly, however, *ceh-26* expression is also severely downregulated, an observation not supported by our fosmid reporter data. This may be a true result, as the fosmid reporter expression may be affected by high copy number, or it may reflect a bias against the CEPsh in the sorted cell population. The mRNA of these cells has not been sequenced, but is likely to be of use in future studies.

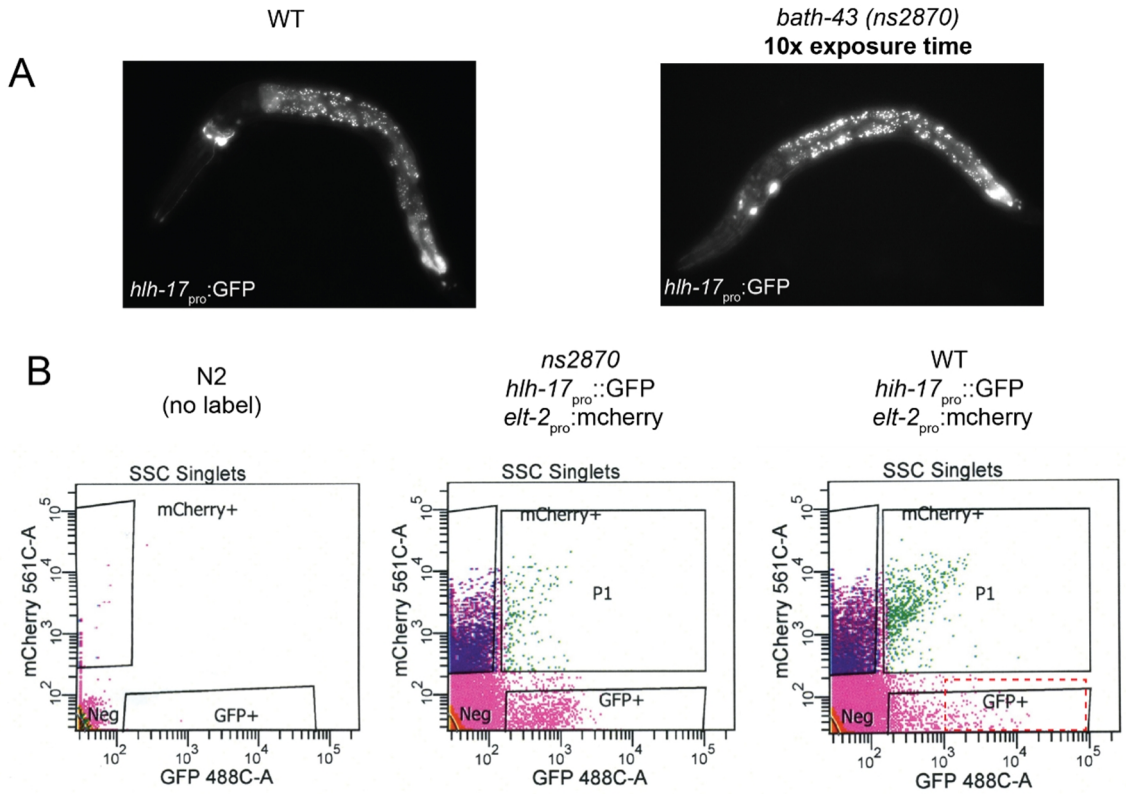


**Figure D.7 Strategy for *bath-43* Transcriptome Analysis in the CEP sheath (A) *hlh-17* reporter expression in WT (left) and *bath-43* (right). Note that additional cells in the ventral cord are visible with high exposure times. (B) FACS sorting strategy for isolating *bath-43* GFP(+) cells vs. WT**

**Table 7: RNA-seq of Isolated Cells from *bath-43* vs. Wildtype**

	Fold Change by qPCR	Fold Change by RNA-seq (from WT RNA-seq data for CEPsh)
<b><i>hlh-17</i></b>		
GFP(+) WT/GFP(-) WT	97.83	101.82
GFP(+) <i>bath-43</i> /GFP(-) <i>bath-43</i>	37.65	
GFP(+) <i>bath-43</i> /GFP(+) WT	0.38	
<b><i>ptr-10</i></b>		
GFP(+) WT/GFP(-) WT	1.91	1.72
GFP(+) <i>bath-43</i> /GFP(-) <i>bath-43</i>	0.07	
GFP(+) <i>bath-43</i> /GFP(+) WT	0.03	
<b><i>ceh-26</i></b>		
GFP(+) WT/GFP(-) WT	2.06	1.19
GFP(+) <i>bath-43</i> /GFP(-) <i>bath-43</i>	0.04	
GFP(+) <i>bath-43</i> /GFP(+) WT	<b>0.02</b>	

## Discussion

Here we describe a molecular program governing glial development in *C. elegans*. First, we show that bHLH transcription factors, including *hlh-17*/Olig2, control *ptr-10*/Patched-related expression in glia. We show that *ptr-10*/Patched-related has a function in directing the formation of the glial sensory lumen. Next, we elucidate a function for *bath-43*, a novel regulator of both *hlh-17*/Olig2 and *ptr-10*/Patched-related specifically in the *C. elegans* CEPsh glia.

An important future goal will be to identify the substrate linking *bath-43* to the expression of these glia-specific genes. Based on the results of the yeast-two hybrid screen, *ztf-16*, which has known functions in the amphid sheath, is a possible candidate. It is important to note that *bath-43* loss-of-function should lead to an accumulation of its



substrate transcription factor; therefore, the substrate is more likely to be a transcriptional repressor.

A link to the function of evolutionary homologs of *bath-43* may lie in the regulation of Patched and Patched-related proteins. Interestingly, the fly homolog of *bath-43*, Hib, is induced by Hedgehog signaling through the Patched (Ptc) protein<sup>16</sup>. In this system, Hib is responsible for degrading the transcriptional effector Ci, which is also directly activated by Hedgehog signaling. Ci, in turn, upregulates Patched expression. In the *Drosophila* system, mutants of Hib lead to increased Patched expression and cell overproliferation; however, mutations in *bath-43* appear to have the opposite effect, causing downregulation of *ptr-10*/Patched-related. Moreover, ligands for Patched-related genes are not known in *C. elegans*, nor is it known whether Hedgehog signaling occurs. Thus, further studies will be required to determine if *bath-43* has a similar role in these systems.

## Bibliography

1. Ramon Y Cajal, S. S. *Histologie Système Nerveux de L'homme et des Vertébrés*. Vol 2. Maloine, Paris; 1911.
2. Yang, G., Pan, F. & Gan, W.-B. B. Stably maintained dendritic spines are associated with lifelong memories. *Nature* **462**, 920–4 (2009).
3. Mizrahi, A. & Katz, L. C. Dendritic stability in the adult olfactory bulb. *Nat. Neurosci.* **6**, 1201–7 (2003).
4. O'Rourke, N. A., Cline, H. T. & Fraser, S. E. Rapid remodeling of retinal arbors in the tectum with and without blockade of synaptic transmission. *Neuron* **12**, 921–34 (1994).
5. Meyer, M. P. & Smith, S. J. Evidence from in vivo imaging that synaptogenesis guides the growth and branching of axonal arbors by two distinct mechanisms. *J. Neurosci.* **26**, 3604–14 (2006).
6. SPERRY, R. W. CHEMOAFFINITY IN THE ORDERLY GROWTH OF NERVE FIBER PATTERNS AND CONNECTIONS. *Proc. Natl. Acad. Sci. U.S.A.* **50**, 703–10 (1963).
7. Walter, J., Kern-Veits, B., Huf, J., Stolze, B. & Bonhoeffer, F. Recognition of position-specific properties of tectal cell membranes by retinal axons in vitro. *Development* **101**, 685–96 (1987).
8. Nakamoto, M. *et al.* Topographically specific effects of ELF-1 on retinal axon guidance in vitro and retinal axon mapping in vivo. *Cell* **86**, 755–66 (1996).
9. Drescher, U. *et al.* In vitro guidance of retinal ganglion cell axons by RAGS, a 25 kDa tectal protein related to ligands for Eph receptor tyrosine kinases. *Cell* **82**, 359–70 (1995).
10. Luo, Y., Raible, D. & Raper, J. A. Collapsin: a protein in brain that induces the collapse and paralysis of neuronal growth cones. *Cell* **75**, 217–27 (1993).
11. Kennedy, T. E., Serafini, T., de la Torre, J. R. & Tessier-Lavigne, M. Netrins are diffusible chemotropic factors for commissural axons in the embryonic spinal cord. *Cell* **78**, 425–35 (1994).
12. Tanaka, E. M. & Kirschner, M. W. Microtubule behavior in the growth cones of living neurons during axon elongation. *J. Cell Biol.* **115**, 345–63 (1991).
13. Buck, K. B. & Zheng, J. Q. Growth cone turning induced by direct local modification of microtubule dynamics. *J. Neurosci.* **22**, 9358–67 (2002).

14. Grutzendler, J., Kasthuri, N. & Gan, W.-B. B. Long-term dendritic spine stability in the adult cortex. *Nature* **420**, 812–6 (2002).
15. Trachtenberg, J. T. *et al.* Long-term in vivo imaging of experience-dependent synaptic plasticity in adult cortex. *Nature* **420**, 788–94 (2002).
16. Udan, R. S., Piazza, V. G., Hsu, C.-W. W., Hadjantonakis, A.-K. K. & Dickinson, M. E. Quantitative imaging of cell dynamics in mouse embryos using light-sheet microscopy. *Development* **141**, 4406–14 (2014).
17. Strnad, P. *et al.* Inverted light-sheet microscope for imaging mouse pre-implantation development. *Nat. Methods* **13**, 139–42 (2016).
18. Hutson, L. D. & Chien, C. B. Pathfinding and error correction by retinal axons: the role of *astray/robo2*. *Neuron* **33**, 205–17 (2002).
19. Tomer, R., Khairy, K., Amat, F. & Keller, P. J. Quantitative high-speed imaging of entire developing embryos with simultaneous multiview light-sheet microscopy. *Nat. Methods* **9**, 755–63 (2012).
20. Keller, P. J., Schmidt, A. D., Wittbrodt, J. & Stelzer, E. H. Reconstruction of zebrafish early embryonic development by scanned light sheet microscopy. *Science* **322**, 1065–9 (2008).
21. Durbin, R. Studies on the Development and Organisation of the Nervous System of *Caenorhabditis elegans*. PhD Thesis. University of Cambridge. (1997).
22. Xu, Z., Li, H. & Wadsworth, W. G. The roles of multiple UNC-40 (DCC) receptor-mediated signals in determining neuronal asymmetry induced by the UNC-6 (netrin) ligand. *Genetics* **183**, 941–9 (2009).
23. Lim, Y. S. & Wadsworth, W. G. Identification of domains of netrin UNC-6 that mediate attractive and repulsive guidance and responses from cells and growth cones. *J. Neurosci.* **22**, 7080–7 (2002).
24. Lim, Y. S., Mallapur, S., Kao, G., Ren, X. C. & Wadsworth, W. G. Netrin UNC-6 and the regulation of branching and extension of motoneuron axons from the ventral nerve cord of *Caenorhabditis elegans*. *J. Neurosci.* **19**, 7048–56 (1999).
25. Zallen, J. A., Yi, B. A. & Bargmann, C. I. The conserved immunoglobulin superfamily member SAX-3/Robo directs multiple aspects of axon guidance in *C. elegans*. *Cell* **92**, 217–27 (1998).
26. Zallen, J. A., Kirch, S. A. & Bargmann, C. I. Genes required for axon pathfinding and extension in the *C. elegans* nerve ring. *Development* **126**, 3679–92 (1999).

27. Wadsworth, W. G., Bhatt, H. & Hedgecock, E. M. Neuroglia and pioneer neurons express UNC-6 to provide global and local netrin cues for guiding migrations in *C. elegans*. *Neuron* **16**, 35–46 (1996).
28. Kennerdell, J. R., Fetter, R. D. & Bargmann, C. I. Wnt-Ror signaling to SIA and SIB neurons directs anterior axon guidance and nerve ring placement in *C. elegans*. *Development* **136**, 3801–10 (2009).
29. Yoshimura, S., Murray, J. I., Lu, Y., Waterston, R. H. & Shaham, S. mls-2 and vab-3 Control glia development, hlh-17/Olig expression and glia-dependent neurite extension in *C. elegans*. *Development* **135**, 2263–75 (2008).
30. White, J. G., Southgate, E., Thomson, J. N. & Brenner, S. The structure of the nervous system of the nematode *Caenorhabditis elegans*. *Philos. Trans. R. Soc. Lond., B, Biol. Sci.* **314**, 1–340 (1986).
31. Schnabel, R., Hutter, H., Moerman, D. & Schnabel, H. Assessing normal embryogenesis in *Caenorhabditis elegans* using a 4D microscope: variability of development and regional specification. *Dev. Biol.* **184**, 234–65 (1997).
32. Bao, Z. *et al.* Automated cell lineage tracing in *Caenorhabditis elegans*. *Proc. Natl. Acad. Sci. U.S.A.* **103**, 2707–12 (2006).
33. Santella, A., Du, Z., Nowotschin, S., Hadjantonakis, A.-K. K. & Bao, Z. A hybrid blob-slice model for accurate and efficient detection of fluorescence labeled nuclei in 3D. *BMC Bioinformatics* **11**, 580 (2010).
34. Santella, A., Du, Z. & Bao, Z. A semi-local neighborhood-based framework for probabilistic cell lineage tracing. *BMC Bioinformatics* **15**, 217 (2014).
35. Richards, J. L., Zacharias, A. L., Walton, T., Burdick, J. T. & Murray, J. I. A quantitative model of normal *Caenorhabditis elegans* embryogenesis and its disruption after stress. *Dev. Biol.* **374**, 12–23 (2013).
36. Giurumescu, C. A. *et al.* Quantitative semi-automated analysis of morphogenesis with single-cell resolution in complex embryos. *Development* **139**, 4271–9 (2012).
37. Murray, J. I. *et al.* Automated analysis of embryonic gene expression with cellular resolution in *C. elegans*. *Nat. Methods* **5**, 703–9 (2008).
38. Wu, Y. *et al.* Inverted selective plane illumination microscopy (iSPIM) enables coupled cell identity lineaging and neurodevelopmental imaging in *Caenorhabditis elegans*. *Proc. Natl. Acad. Sci. U.S.A.* **108**, 17708–13 (2011).
39. Christensen, R. P. *et al.* Untwisting the *Caenorhabditis elegans* embryo. *Elife* **4**, (2015).

40. Wu, Y. *et al.* Spatially isotropic four-dimensional imaging with dual-view plane illumination microscopy. *Nat. Biotechnol.* **31**, 1032–8 (2013).
41. Godement, P., Wang, L. C. & Mason, C. A. Retinal axon divergence in the optic chiasm: dynamics of growth cone behavior at the midline. *J. Neurosci.* **14**, 7024–39 (1994).
42. Serbedzija, G. N., Bronner-Fraser, M. & Fraser, S. E. A vital dye analysis of the timing and pathways of avian trunk neural crest cell migration. *Development* **106**, 809–16 (1989).
43. Eagleson, G. W. & Harris, W. A. Mapping of the presumptive brain regions in the neural plate of *Xenopus laevis*. *J. Neurobiol.* **21**, 427–40 (1990).
44. Chalfie, M., Tu, Y., Euskirchen, G., Ward, W. W. & Prasher, D. C. Green fluorescent protein as a marker for gene expression. *Science* **263**, 802–5 (1994).
45. Duffy, J. B. GAL4 system in *Drosophila*: a fly geneticist's Swiss army knife. *Genesis* **34**, 1–15 (2002).
46. Scheer, N. & Campos-Ortega, J. A. Use of the Gal4-UAS technique for targeted gene expression in the zebrafish. *Mech. Dev.* **80**, 153–8 (1999).
47. Luan, H., Peabody, N. C., Vinson, C. R. & White, B. H. Refined spatial manipulation of neuronal function by combinatorial restriction of transgene expression. *Neuron* **52**, 425–36 (2006).
48. Potter, C. J., Tasic, B., Russler, E. V., Liang, L. & Luo, L. The Q system: a repressible binary system for transgene expression, lineage tracing, and mosaic analysis. *Cell* **141**, 536–48 (2010).
49. Wei, X., Potter, C. J., Luo, L. & Shen, K. Controlling gene expression with the Q repressible binary expression system in *Caenorhabditis elegans*. *Nat. Methods* **9**, 391–5 (2012).
50. Distel, M., Wullmann, M. F. & Köster, R. W. Optimized Gal4 genetics for permanent gene expression mapping in zebrafish. *Proc. Natl. Acad. Sci. U.S.A.* **106**, 13365–70 (2009).
51. Struhl, G. & Basler, K. Organizing activity of wingless protein in *Drosophila*. *Cell* **72**, 527–40 (1993).
52. Macosko, E. Z. *et al.* A hub-and-spoke circuit drives pheromone attraction and social behaviour in *C. elegans*. *Nature* **458**, 1171–5 (2009).

53. Lee, T. & Luo, L. Mosaic analysis with a repressible cell marker (MARCM) for *Drosophila* neural development. *Trends Neurosci.* **24**, 251–4 (2001).
54. Yu, H.-H. H., Chen, C.-H. H., Shi, L., Huang, Y. & Lee, T. Twin-spot MARCM to reveal the developmental origin and identity of neurons. *Nat. Neurosci.* **12**, 947–53 (2009).
55. Yu, H.-H. H. *et al.* A complete developmental sequence of a *Drosophila* neuronal lineage as revealed by twin-spot MARCM. *PLoS Biol.* **8**, (2010).
56. Collins, R. T., Linker, C. & Lewis, J. MAZE: a tool for mosaic analysis of gene function in zebrafish. *Nat. Methods* **7**, 219–23 (2010).
57. Badea, T. C. *et al.* New mouse lines for the analysis of neuronal morphology using CreER(T)/loxP-directed sparse labeling. *PLoS ONE* **4**, e7859 (2009).
58. Livet, J. *et al.* Transgenic strategies for combinatorial expression of fluorescent proteins in the nervous system. *Nature* **450**, 56–62 (2007).
59. Hadjieconomou, D. *et al.* Flybow: genetic multicolor cell labeling for neural circuit analysis in *Drosophila melanogaster*. *Nat. Methods* **8**, 260–6 (2011).
60. Pan, Y. A. *et al.* Zebrabow: multispectral cell labeling for cell tracing and lineage analysis in zebrafish. *Development* **140**, 2835–46 (2013).
61. Wachsman, G., Heidstra, R. & Scheres, B. Distinct cell-autonomous functions of RETINOBLASTOMA-RELATED in *Arabidopsis* stem cells revealed by the Brother of Brainbow clonal analysis system. *Plant Cell* **23**, 2581–91 (2011).
62. Loulier, K. *et al.* Multiplex cell and lineage tracking with combinatorial labels. *Neuron* **81**, 505–20 (2014).
63. Chen, C.-H. H. *et al.* Multicolor Cell Barcoding Technology for Long-Term Surveillance of Epithelial Regeneration in Zebrafish. *Dev. Cell* **36**, 668–80 (2016).
64. Kanca, O., Caussinus, E., Denes, A. S., Percival-Smith, A. & Affolter, M. Raepli: a whole-tissue labeling tool for live imaging of *Drosophila* development. *Development* **141**, 472–80 (2014).
65. Boulina, M., Samarajeewa, H., Baker, J. D., Kim, M. D. & Chiba, A. Live imaging of multicolor-labeled cells in *Drosophila*. *Development* **140**, 1605–13 (2013).
66. Marinković, P., Godinho, L. & Misgeld, T. Generation and Screening of Transgenic Mice with Neuronal Labeling Controlled by Thy1 Regulatory Elements. *Cold Spring Harb Protoc* **2015**, 875–82 (2015).

67. Smith, C. J., Morris, A. D., Welsh, T. G. & Kucenas, S. Contact-mediated inhibition between oligodendrocyte progenitor cells and motor exit point glia establishes the spinal cord transition zone. *PLoS Biol.* **12**, e1001961 (2014).
68. Heiman, M. G. & Shaham, S. DEX-1 and DYF-7 establish sensory dendrite length by anchoring dendritic tips during cell migration. *Cell* **137**, 344–55 (2009).
69. Konermann, S. *et al.* Optical control of mammalian endogenous transcription and epigenetic states. *Nature* **500**, 472–6 (2013).
70. Kennedy, M. J. *et al.* Rapid blue-light-mediated induction of protein interactions in living cells. *Nat. Methods* **7**, 973–5 (2010).
71. Taslimi, A. *et al.* Optimized second-generation CRY2-CIB dimerizers and photoactivatable Cre recombinase. *Nat. Chem. Biol.* **12**, 425–30 (2016).
72. Niopek, D. *et al.* Engineering light-inducible nuclear localization signals for precise spatiotemporal control of protein dynamics in living cells. *Nat Commun* **5**, 4404 (2014).
73. Yumerefendi, H. *et al.* Control of Protein Activity and Cell Fate Specification via Light-Mediated Nuclear Translocation. *PLoS ONE* **10**, e0128443 (2015).
74. Deguchi, T. *et al.* Infrared laser-mediated local gene induction in medaka, zebrafish and *Arabidopsis thaliana*. *Dev. Growth Differ.* **51**, 769–75 (2009).
75. Kamei, Y. *et al.* Infrared laser-mediated gene induction in targeted single cells in vivo. *Nat. Methods* **6**, 79–81 (2009).
76. Miao, G. & Hayashi, S. Manipulation of gene expression by infrared laser heat shock and its application to the study of tracheal development in *Drosophila*. *Dev. Dyn.* **244**, 479–87 (2015).
77. Stringham, E. G. & Candido, E. P. Targeted single-cell induction of gene products in *Caenorhabditis elegans*: a new tool for developmental studies. *J. Exp. Zool.* **266**, 227–33 (1993).
78. Kalmar, B. & Greensmith, L. Induction of heat shock proteins for protection against oxidative stress. *Adv. Drug Deliv. Rev.* **61**, 310–8 (2009).
79. Bienz, M. & Pelham, H. R. Heat shock regulatory elements function as an inducible enhancer in the *Xenopus hsp70* gene and when linked to a heterologous promoter. *Cell* **45**, 753–60 (1986).

80. Pelham, H. R. & Bienz, M. A synthetic heat-shock promoter element confers heat-inducibility on the herpes simplex virus thymidine kinase gene. *EMBO J.* **1**, 1473–7 (1982).
81. Prahlad, V., Cornelius, T. & Morimoto, R. I. Regulation of the cellular heat shock response in *Caenorhabditis elegans* by thermosensory neurons. *Science* **320**, 811–4 (2008).
82. Richter, K., Haslbeck, M. & Buchner, J. The heat shock response: life on the verge of death. *Mol. Cell* **40**, 253–66 (2010).
83. Hentze, N., Le Breton, L., Wiesner, J., Kempf, G. & Mayer, M. P. Molecular mechanism of thermosensory function of human heat shock transcription factor Hsf1. *Elife* **5**, (2016).
84. Clos, J., Rabindran, S., Wisniewski, J. & Wu, C. Induction temperature of human heat shock factor is reprogrammed in a *Drosophila* cell environment. *Nature* **364**, 252–5 (1993).
85. Zou, J., Guo, Y., Guettouche, T., Smith, D. F. & Voellmy, R. Repression of heat shock transcription factor HSF1 activation by HSP90 (HSP90 complex) that forms a stress-sensitive complex with HSF1. *Cell* **94**, 471–80 (1998).
86. Abravaya, K., Myers, M. P., Murphy, S. P. & Morimoto, R. I. The human heat shock protein hsp70 interacts with HSF, the transcription factor that regulates heat shock gene expression. *Genes Dev.* **6**, 1153–64 (1992).
87. Stringham, E. G., Dixon, D. K., Jones, D. & Candido, E. P. Temporal and spatial expression patterns of the small heat shock (hsp16) genes in transgenic *Caenorhabditis elegans*. *Mol. Biol. Cell* **3**, 221–33 (1992).
88. Harris, J., Honigberg, L., Robinson, N. & Kenyon, C. Neuronal cell migration in *C. elegans*: regulation of Hox gene expression and cell position. *Development* **122**, 3117–31 (1996).
89. Venero Galanternik, M., Nikaido, M., Yu, Z., McKinney, S. A. & Piotrowski, T. Localized Gene Induction by Infrared-Mediated Heat Shock. *Zebrafish* (2016). doi:10.1089/zeb.2015.1161
90. Churgin, M. A., He, L., Murray, J. I. & Fang-Yen, C. Efficient single-cell transgene induction in *Caenorhabditis elegans* using a pulsed infrared laser. *G3 (Bethesda)* **3**, 1827–32 (2013).
91. Suzuki, M., Toyoda, N. & Takagi, S. Pulsed irradiation improves target selectivity of infrared laser-evoked gene operator for single-cell gene induction in the nematode *C. elegans*. *PLoS ONE* **9**, e85783 (2014).



92. Link, C. D., Cypser, J. R., Johnson, C. J. & Johnson, T. E. Direct observation of stress response in *Caenorhabditis elegans* using a reporter transgene. *Cell Stress Chaperones* **4**, 235–42 (1999).
93. Beck, C. D. & Rankin, C. H. Heat shock disrupts long-term memory consolidation in *Caenorhabditis elegans*. *Learn. Mem.* **2**, 161–77 (1995).
94. Jones, D. & Candido, E. P. Feeding is inhibited by sublethal concentrations of toxicants and by heat stress in the nematode *Caenorhabditis elegans*: relationship to the cellular stress response. *J. Exp. Zool.* **284**, 147–57 (1999).
95. Jones, D., Russnak, R. H., Kay, R. J. & Candido, E. P. Structure, expression, and evolution of a heat shock gene locus in *Caenorhabditis elegans* that is flanked by repetitive elements. *J. Biol. Chem.* **261**, 12006–15 (1986).
96. Jones, D., Dixon, D. K., Graham, R. W. & Candido, E. P. Differential regulation of closely related members of the hsp16 gene family in *Caenorhabditis elegans*. *DNA* **8**, 481–90 (1989).
97. Murray, J. I. & Bao, Z. Automated lineage and expression profiling in live *Caenorhabditis elegans* embryos. *Cold Spring Harb Protoc* **2012**, (2012).
98. Vogel, Noack, Hüttman & Paltauf. Mechanisms of femtosecond laser nanosurgery of cells and tissues. *Appl Phys B* **81**, 1015–1047 (2005).
99. Bao, Z., Zhao, Z., Boyle, T. J., Murray, J. I. & Waterston, R. H. Control of cell cycle timing during *C. elegans* embryogenesis. *Dev. Biol.* **318**, 65–72 (2008).
100. Komuro, H., Yacubova, E., Yacubova, E. & Rakic, P. Mode and tempo of tangential cell migration in the cerebellar external granular layer. *J. Neurosci.* **21**, 527–40 (2001).
101. Sulston, J. E., Schierenberg, E., White, J. G. & Thomson, J. N. The embryonic cell lineage of the nematode *Caenorhabditis elegans*. *Dev. Biol.* **100**, 64–119 (1983).
102. Hao, J. C. *et al.* *C. elegans* slit acts in midline, dorsal-ventral, and anterior-posterior guidance via the SAX-3/Robo receptor. *Neuron* **32**, 25–38 (2001).
103. Grossman, E. N., Giurumescu, C. A. & Chisholm, A. D. Mechanisms of ephrin receptor protein kinase-independent signaling in amphid axon guidance in *Caenorhabditis elegans*. *Genetics* **195**, 899–913 (2013).
104. George, S. E., Simokat, K., Hardin, J. & Chisholm, A. D. The VAB-1 Eph receptor tyrosine kinase functions in neural and epithelial morphogenesis in *C. elegans*. *Cell* **92**, 633–43 (1998).

105. Peckol, E. L., Zallen, J. A., Yarrow, J. C. & Bargmann, C. I. Sensory activity affects sensory axon development in *C. elegans*. *Development* **126**, 1891–902 (1999).
106. Zallen, J. A., Peckol, E. L., Tobin, D. M. & Bargmann, C. I. Neuronal cell shape and neurite initiation are regulated by the Ndr kinase SAX-1, a member of the Orb6/COT-1/warts serine/threonine kinase family. *Mol. Biol. Cell* **11**, 3177–90 (2000).
107. Bülow, H. E., Berry, K. L., Topper, L. H., Peles, E. & Hobert, O. Heparan sulfate proteoglycan-dependent induction of axon branching and axon misrouting by the Kallmann syndrome gene *kal-1*. *Proc. Natl. Acad. Sci. U.S.A.* **99**, 6346–51 (2002).
108. Perens, E. A. & Shaham, S. C. *C. elegans* *daf-6* encodes a patched-related protein required for lumen formation. *Dev. Cell* **8**, 893–906 (2005).
109. Oikonomou, G. *et al.* Opposing activities of LIT-1/NLK and DAF-6/patched-related direct sensory compartment morphogenesis in *C. elegans*. *PLoS Biol.* **9**, e1001121 (2011).
110. Fang-Yen, C., Gabel, C. V., Samuel, A. D., Bargmann, C. I. & Avery, L. Laser microsurgery in *Caenorhabditis elegans*. *Methods Cell Biol.* **107**, 177–206 (2012).
111. Bargmann, C. I. & Avery, L. Laser killing of cells in *Caenorhabditis elegans*. *Methods Cell Biol.* **48**, 225–50 (1995).
112. Yanik, M. F. *et al.* Neurosurgery: functional regeneration after laser axotomy. *Nature* **432**, 822 (2004).
113. Ben-Yakar, A. & Bourgeois, F. Ultrafast laser nanosurgery in microfluidics for genome-wide screenings. *Curr. Opin. Biotechnol.* **20**, 100–5 (2009).
114. Shcherbo, D. *et al.* Far-red fluorescent tags for protein imaging in living tissues. *Biochem. J.* **418**, 567–74 (2009).
115. Santella, A. *et al.* WormGUIDES: an interactive single cell developmental atlas and tool for collaborative multidimensional data exploration. *BMC Bioinformatics* **16**, 189 (2015).
116. Morton, E. A. & Lamitina, T. *Caenorhabditis elegans* HSF-1 is an essential nuclear protein that forms stress granule-like structures following heat shock. *Aging Cell* **12**, 112–20 (2013).
117. Brenner, S. The genetics of *Caenorhabditis elegans*. *Genetics* **77**, 71–94 (1974).
118. Stiernagle, T. Maintenance of *C. elegans*. *WormBook* 1–11 (2006).  
doi:10.1895/wormbook.1.101.1

119. Bao, Z. & Murray, J. I. Mounting *Caenorhabditis elegans* embryos for live imaging of embryogenesis. *Cold Spring Harb Protoc* **2011**, (2011).
120. Adler, C. E., Fetter, R. D. & Bargmann, C. I. UNC-6/Netrin induces neuronal asymmetry and defines the site of axon formation. *Nat. Neurosci.* **9**, 511–8 (2006).
121. Murray, J. I., Bao, Z., Boyle, T. J. & Waterston, R. H. The lineaging of fluorescently-labeled *Caenorhabditis elegans* embryos with StarryNite and AceTree. *Nat Protoc* **1**, 1468–76 (2006).
122. Wang, S.-Z. Z., Liu, B.-H. H., Tao, H. W., Xia, K. & Zhang, L. I. A genetic strategy for stochastic gene activation with regulated sparseness (STARS). *PLoS ONE* **4**, e4200 (2009).
123. Moore, J. L., Du, Z. & Bao, Z. Systematic quantification of developmental phenotypes at single-cell resolution during embryogenesis. *Development* **140**, 3266–74 (2013).
124. Long, F., Peng, H., Liu, X., Kim, S. K. & Myers, E. A 3D digital atlas of *C. elegans* and its application to single-cell analyses. *Nat. Methods* **6**, 667–72 (2009).
125. Noctor, S. C., Flint, A. C., Weissman, T. A., Dammerman, R. S. & Kriegstein, A. R. Neurons derived from radial glial cells establish radial units in neocortex. *Nature* **409**, 714–20 (2001).
126. Hosoya, T., Takizawa, K., Nitta, K. & Hotta, Y. glial cells missing: a binary switch between neuronal and glial determination in *Drosophila*. *Cell* **82**, 1025–36 (1995).
127. Bacaj, T., Tevlin, M., Lu, Y. & Shaham, S. Glia are essential for sensory organ function in *C. elegans*. *Science* **322**, 744–7 (2008).
128. Singhvi, A. *et al.* A Glial K/Cl Transporter Controls Neuronal Receptive Ending Shape by Chloride Inhibition of an rGC. *Cell* **165**, 936–48 (2016).
129. Wallace, S. W., Singhvi, A., Liang, Y., Lu, Y. & Shaham, S. PROS-1/Prospero Is a Major Regulator of the Glia-Specific Secretome Controlling Sensory-Neuron Shape and Function in *C. elegans*. *Cell Rep* **15**, 550–62 (2016).
130. Pintard, L. *et al.* The BTB protein MEL-26 is a substrate-specific adaptor of the CUL-3 ubiquitin-ligase. *Nature* **425**, 311–6 (2003).
131. Luke-Glaser, S., Pintard, L., Lu, C., Mains, P. E. & Peter, M. The BTB protein MEL-26 promotes cytokinesis in *C. elegans* by a CUL-3-independent mechanism. *Curr. Biol.* **15**, 1605–15 (2005).

132. Tong, Y.-G. G. & Bürglin, T. R. Conditions for dye-filling of sensory neurons in *Caenorhabditis elegans*. *J. Neurosci. Methods* **188**, 58–61 (2010).
133. McMiller, T. L. & Johnson, C. M. Molecular characterization of HLH-17, a *C. elegans* bHLH protein required for normal larval development. *Gene* **356**, 1–10 (2005).
134. Lee, S.-K. K., Lee, B., Ruiz, E. C. & Pfaff, S. L. Olig2 and Ngn2 function in opposition to modulate gene expression in motor neuron progenitor cells. *Genes Dev.* **19**, 282–94 (2005).
135. Shteingauz, A., Cohen, E., Biala, Y. & Treinin, M. The BTB-MATH protein BATH-42 interacts with RIC-3 to regulate maturation of nicotinic acetylcholine receptors. *J. Cell. Sci.* **122**, 807–12 (2009).
136. Zhu, H. *et al.* SPOP E3 Ubiquitin Ligase Adaptor Promotes Cellular Senescence by Degrading the SENP7 deSUMOylase. *Cell Rep* **13**, 1183–93 (2015).
137. Zhang, Q. *et al.* A hedgehog-induced BTB protein modulates hedgehog signaling by degrading Ci/Gli transcription factor. *Dev. Cell* **10**, 719–29 (2006).
138. Thomas, J. H. Adaptive evolution in two large families of ubiquitin-ligase adapters in nematodes and plants. *Genome Res.* **16**, 1017–30 (2006).
139. An, J., Wang, C., Deng, Y., Yu, L. & Huang, H. Destruction of full-length androgen receptor by wild-type SPOP, but not prostate-cancer-associated mutants. *Cell Rep* **6**, 657–69 (2014).
140. Gan, W. *et al.* SPOP Promotes Ubiquitination and Degradation of the ERG Oncoprotein to Suppress Prostate Cancer Progression. *Mol. Cell* **59**, 917–30 (2015).
141. Blattner, M. *et al.* SPOP mutations in prostate cancer across demographically diverse patient cohorts. *Neoplasia* **16**, 14–20 (2014).
142. Zhang, Q. *et al.* Multiple Ser/Thr-rich degrons mediate the degradation of Ci/Gli by the Cul3-HIB/SPOP E3 ubiquitin ligase. *Proc. Natl. Acad. Sci. U.S.A.* **106**, 21191–6 (2009).
143. Nagai, Y. *et al.* Identification of a novel nuclear speckle-type protein, SPOP. *FEBS Lett.* **418**, 23–6 (1997).
144. Weber, H. & Hellmann, H. Arabidopsis thaliana BTB/ POZ-MATH proteins interact with members of the ERF/AP2 transcription factor family. *FEBS J.* **276**, 6624–35 (2009).
145. Zhuang, M. *et al.* Structures of SPOP-substrate complexes: insights into molecular architectures of BTB-Cul3 ubiquitin ligases. *Mol. Cell* **36**, 39–50 (2009).

146. Procko, C., Lu, Y. & Shaham, S. Sensory organ remodeling in *Caenorhabditis elegans* requires the zinc-finger protein ZTF-16. *Genetics* **190**, 1405–15 (2012).
147. Zhang, S., Banerjee, D. & Kuhn, J. R. Isolation and culture of larval cells from *C. elegans*. *PLoS ONE* **6**, e19505 (2011).
148. Spencer, W. C. *et al.* Isolation of specific neurons from *C. elegans* larvae for gene expression profiling. *PLoS ONE* **9**, e112102 (2014).